

University of Alberta

*Electron Irradiation Damage to Organic Light-Emitting Materials*

by

*Peng Li*



A thesis submitted to the Faculty of Graduate Studies and Research in partial fulfillment of  
the  
requirements for the degree of *Master of Science*

Department of *Physics*

Edmonton, Alberta  
Spring 2004



Library and  
Archives Canada

Bibliothèque et  
Archives Canada

Published Heritage  
Branch

Direction du  
Patrimoine de l'édition

395 Wellington Street  
Ottawa ON K1A 0N4  
Canada

395, rue Wellington  
Ottawa ON K1A 0N4  
Canada

*Your file* *Votre référence*  
*ISBN: 0-612-96512-0*  
*Our file* *Notre référence*  
*ISBN: 0-612-96512-0*

The author has granted a non-exclusive license allowing the Library and Archives Canada to reproduce, loan, distribute or sell copies of this thesis in microform, paper or electronic formats.

L'auteur a accordé une licence non exclusive permettant à la Bibliothèque et Archives Canada de reproduire, prêter, distribuer ou vendre des copies de cette thèse sous la forme de microfiche/film, de reproduction sur papier ou sur format électronique.

The author retains ownership of the copyright in this thesis. Neither the thesis nor substantial extracts from it may be printed or otherwise reproduced without the author's permission.

L'auteur conserve la propriété du droit d'auteur qui protège cette thèse. Ni la thèse ni des extraits substantiels de celle-ci ne doivent être imprimés ou autrement reproduits sans son autorisation.

---

In compliance with the Canadian Privacy Act some supporting forms may have been removed from this thesis.

Conformément à la loi canadienne sur la protection de la vie privée, quelques formulaires secondaires ont été enlevés de cette thèse.

While these forms may be included in the document page count, their removal does not represent any loss of content from the thesis.

Bien que ces formulaires aient inclus dans la pagination, il n'y aura aucun contenu manquant.

# Canada

## **Abstract**

Organic materials have been widely applied these days due to many advantages over their inorganic counterparts. One problem associated with electron microscopy, when applied to organic and biological specimens, is radiation damage from the area being analyzed.

It has been reported that there is no obvious damage to some aromatics below the K-shell ionization energy  $\sim 285\text{eV}$ . If this were true, it would dramatically enhance the microscopy for organic and biological samples when applying a low-energy electron beam. In the field of lithography, the spatial resolution could be much improved by using the aromatic materials as electron-beam resists, using a suitable incident energy.

The radiation damage cross-section of a coronene sample as a function of the incident energy was studied by monitoring the decay of cathodoluminescence (CL) emission intensity. Results were compared with previous measurements to understand the electron irradiation damage mechanism in organic materials.

## **Acknowledgements**

First and foremost, I would like to express my gratitude to my wife Fiona and my parents for their continued support.

My sincere gratitude goes to my supervisor Dr. Ray Egerton for his patience, kind advice and support. Also I would like to thank my committee Dr. Mark Freeman, Dr. Al Meldrum and Dr. Frank Hegmann and Dr. Rik Tykwinski for their encouragement and fruitful discussions.

I would like to acknowledge to Dr. Marek Malac and Mr. Greg Popowich for their support and advice on sample preparation and electron microscopy.

I'm especially grateful to Don Mullin, Tony Walford, Yolande Peske, Steve Rogers, Lynn Chandler and Sarah Derr for their technical and administrative help.

I would like to make special mention about Ms. Qu, my physics teacher in high-school, who led me into the field of physics.

Last, but not least my thanks belong to Feng Wang, Julie Qian, Svitlana Shcherbyna and all my Chinese friends at the University of Alberta for their help in my thesis preparation and daily life at Edmonton.

## Table of Contents

Chapter 1. Organic light-emitting materials .....	1
Introduction .....	1
Organic light-emitting mechanism.....	2
The origins of organic luminescence.....	2
Requirements for luminescence.....	2
Luminescence processes in aromatics .....	4
Applications of organic light-emitting materials .....	7
Quenching mechanism and damage to organic materials by electrons .....	9
Degradation in organic light-emitting devices .....	9
Radiation damage to organic materials by electrons in the Electron Microscope.....	10
Chapter 2. Sample preparation and radiation damage measurement by an analytical transmission electron microscope (TEM) .....	20
Introduction .....	20
Sample preparation, film structure and electron diffraction pattern .....	21
Vacuum evaporation .....	21
Solvent evaporation.....	28
Electron diffraction pattern and crystal structure.....	29
Fading of electron diffraction pattern.....	30
$\pi$ -peak monitoring by EELS .....	32
Damage measurement at low energy.....	33
Temperature dependence of the damage rate.....	34
Dose-rate independence .....	36

Chapter 3. Cathodoluminescence (CL) measurement in a scanning electron microscope (SEM) .....	61
Introduction .....	61
Cathodoluminescence (CL) spectra measured by fiber/spectrometer system .....	62
Total intensity measured by PMT .....	62
Dependence of CL yield on incident energy .....	63
Decay of the total intensity .....	64
Characteristic dose and damage cross-section .....	65
Problem of undersampling .....	66
Problem of beam heating .....	68
Damage cross-section versus incident energy .....	77
Retarding system .....	77
Surface effect and landing energy calibration by reflection .....	78
CL damage cross- section versus incident energy .....	83
Chapter 4. Discussion .....	106
Energetic electron interaction with solids .....	106
Beam effects in the electron microscope .....	107
High resolution imaging and damage .....	108
Damage mechanism .....	110
General theoretical considerations .....	110
The influence of chemical structure .....	111
The influence of electron energy .....	112
Interpretation of previous and current measurements .....	115
Hydrogen release .....	120
Reduction of damage .....	122

Future work.....	124
Reference.....	139

## List of Figures

- Figure 1-1: Relationship between the excited singlet ( $S_1$ ), triplet (T) and ground ( $S_0$ ) states in (a) aromatic hydrocarbons, and (b) dyes..... 12
- Figure 1-2: Luminescence process in an aromatic material. .... 13
- Figure 1-3: Coronene molecular structure..... 14
- Figure 1-4: Graphic representation of the dose and energy density of 100kV electrons that cause deleterious effects in the listed materials [Hawkes and Valdre 1990]. .... 15
- Figure 1-5: Molecular structures of p-terphenyl and rubrene. .... 16
- Figure 1-6: Coronene Cathodoluminescence (CL) (a) and Photoluminescence (PL) (b) spectra. .... 17
- Figure 1-7: The performance of inorganic and organic light-emitting diodes (LEDs), shown here in terms of the "luminous efficiency" in lumens per watt, has been improving steadily over the years [Friend 1999]..... 18
- Figure 2-1: Diagram of the vacuum evaporation apparatus. .... 38
- Figure 2-2: Morphologies (TEM images) of vacuum-evaporated coronene films (on carbon) with different average thickness: a: 1.4nm; b: 60nm; c:



150nm (from thickness monitor), prepared in room temperature and with a deposition rate of 0.1-0.2 Å/s. ....39

Figure 2-3: 2nm (from thickness monitor) coronene films on different substrates: C-film (a); Cleaved KCl crystal (b); SiN membrane (c). (All were prepared at room temperature and deposition rate of 0.1-0.2 Å/s.).....40

Figure 2-4: A 1.6nm (from thickness monitor) coronene film on carbon film prepared at 90K and deposition rate of 0.02 Å/s. ....41

Figure 2-5: Collection angle dependence of film thickness measured by EELS ( $E_0 = 200\text{keV}$ ; carbon film). Thickness is in terms of  $t/\lambda_i$ , where  $\lambda_i$  is the inelastic mean free path.....42

Figure 2-6: Theoretical calculation of coverage fraction dependence of measured thickness by EELS for non-uniform film.  $t_1$ : thin area;  $t_2$ : thick area;  $t_{\text{eels}}$ : thickness measured by EELS;  $t_{\text{ave}}$ : average thickness. ....43

Figure 2-7: A solvent-evaporated coronene film on a bare TEM Cu grid. The water temperature: 5°C; solvent: 1,2-dichloroethane; the specimen thickness: 70nm. ....44

Figure 2-8: A lacey carbon film. ....45

Figure 2-9: A solvent evaporated coronene film on a lacey carbon grid. Specimen thickness: 40nm; water temperature: 5°C; solvent: 1,2-dichloroethane.....46

Figure 2-10: Diffraction patterns of coronene films on regular and lacey carbon grids: (a): Lacey carbon film; (b): regular carbon supporting film.....47

Figure 2-11: Diffraction pattern fading (coronene) with the increase of irradiation dose ( $E_0=200\text{keV}$ ). A series of diffraction patterns  $a_1, a_2, a_3, a_4$  were irradiated after dose 0 ( $a_1$ ),  $0.12\text{C}/\text{cm}^2$  ( $a_2$ ),  $0.24\text{C}/\text{cm}^2$  ( $a_3$ ) and  $0.48\text{C}/\text{cm}^2$  ( $a_4$ ); a background was recorded after a large dose.  $b_1, b_2, b_3$  and  $b_4$  show the diffraction after subtracting the background. ....48

Figure 2-12: Intensity vs. dose curve of diffraction fading (coronene).  $E_0=200\text{keV}$ . ....49

Figure 2-13: Low-energy loss spectrum of coronene. ....50

Figure 2-14: 6eV-peak fading (coronene) with the increase of irradiation dose ( $E_0=200\text{keV}$ ). A series of energy-loss spectra a, b, c and d were recorded (upper) after dose 0 (a),  $0.292\text{C}/\text{cm}^2$  (b),  $1.31\text{C}/\text{cm}^2$  (c) and  $1.75\text{C}/\text{cm}^2$  (d); 6eV-peaks (lower) can be separated from the tail of the zero peaks. ....51

Figure 2-15: 6eV-peak intensity vs. dose (coronene).  $E_0=200\text{keV}$ . ....52

Figure 2-16: Characteristic doses $D_{1/e}$ and corresponding damage cross-sections measured by diffraction-pattern fading and 6eV-fading (coronene). $E_0=200\text{keV}$ .....	53
Figure 2-17: TEM images of coronene specimens before and after pre-irradiation for a dose of $0.36\text{ C/cm}^2$ at $0.7\text{keV}$ in a low-energy SEM. Diffraction patterns are inserted. A vacuum-evaporated coronene specimen on carbon film: before (a <sub>1</sub> ) & after (a <sub>2</sub> ) irradiation; a solvent-evaporated coronene specimen on lacey carbon film: before (b <sub>1</sub> ) & after (b <sub>2</sub> ) irradiation. ....	54
Figure 2-18: Temperature dependence of damage rate for coronene by diffraction-pattern fading. $E_0=200\text{keV}$ .....	55
Figure 2-19: Temperature dependence of damage rate for coronene by 6eV-peak fading. $E_0=200\text{keV}$ .....	56
Figure 2-20: Dose rate independence of damage rate for coronene by diffraction-pattern fading, $E_0=200\text{keV}$ .....	57
Figure 2-21: Dose rate independence of damage rate for coronene by 6eV-peak fading. $E_0=200\text{keV}$ .....	58
Figure 3-1: Diagram of cathodoluminescence apparatus with a SEM: A fiber optic connected to a spectrometer was fed through the SEM chamber to measure the CL emission spectrum; a PMT/electrometer system was used to measure the total emission intensity.....	84

Figure 3-2: Beam current vs. incident energy in our PHILIPS  
505 SEM. ....85

Figure 3-3: Cathodoluminescence efficiency for coronene and rubrene.  
The efficiency is shown (left) in terms of the intensity/beam current;  
energy deposition (right) was calculated for the primary beam  
transmitted through a 60nm thick coronene film. ....86

Figure 3-4: Cathodoluminescence intensity vs. dose curve. (coronene,  
 $E_0=1\text{keV}$ ) .....87

Figure 3-5: Undersampling for low magnification in the SEM. For low  
line/frame number  $N$  and small spot size  $d$  in the SEM, undersampling  
could happen at low magnifications: the actual area (gray area)  $A_s=d \times N \times L$   
scanned by the electron beam is less than the area (gray + white area)  
 $A_d=W_d \times L$  estimated from the display screen, where  $L$  is the length of  
screen and  $W_d$  is the width of screen.....88

Figure 3-6: An unsupported organic specimen on a TEM grid. The heat  
generated in the specimen (3) by the electron beam will conduct over a  
distance  $R$  from the irradiated area (2) to grid bars (1) whose temperature  
 $T_0$  is the same as the surroundings. 1: Grid bars; 2: Area illuminated by  
e-beam; 3: Organic specimen; 4: SEM stub. ....89

Figure 3-7: Calculated temperature increase for an unsupported 40nm  
thick coronene film during the damage measurement in TEM ( $E_0=200\text{keV}$ ,  
beam diameter:  $2.5\mu\text{m}$ ). ....90

Figure 3-8: Average energy loss in a coronene film (thickness  $t=40\text{nm}$ ), calculated by Bethe Stopping Power Law. The vertical dashed line shows the incident energy where the electron range is approximately equal to the thickness  $t=40\text{nm}$ . .....91

Figure 3-9: Calculated temperature increase for an unsupported 40nm thick coronene film with a stationary beam ( $E_0 = 0.7\text{keV}$ , spot size  $= 0.5\mu\text{m}$ ). .....92

Figure 3-10: Calculated temperature increase for a stationary beam and scanned beam at the SEM video-rate full-frame display ( $I=8\text{nA}$ , spot size  $= 0.5\mu\text{m}$ ). The temperature increase for a scanning beam was estimated by assuming the generated heat will be dispersed between two adjacent scans. If the dissipation time is long compared to the scanning time, the temperature increase could be somewhere between the stationary and the scanned beam case. ....93

Figure 3-11: A supported organic specimen on an Al foil. The heat generated by the electron beam (1) can efficiently conduct through the metal substrate foil (3). The substrate is in thermal contact with the SEM stub (4) whose temperature is  $T_0$ . 1: Electron probe; 2: Organic specimen; 3: Al foil; 4: SEM stub. ....94

Figure 3-12: The heat balance in a supported sample on Al foil. To obtain an upper estimate, we assume that the heat will travel down within a cylinder with a cross-section area of  $A$  to the lower surface whose temperature  $T_0$  is the same as the surroundings (b). In this simplification,

we overestimate T, because in practice the heat will travel in an angular cone (a) down to the stub instead of being limited to the cylinder. ....95

Figure 3-13: Calculated temperature increase for a thin coronene sample (40 nm) on a thick Al foil (~20 $\mu$ m) in the low-energy range. (I=8nA, spot size = 0.5 $\mu$ m). .....96

Figure 3-14: Calculated temperature increase for a stationary beam (0.1-30keV) illuminating an Al-foil supported coronene film (40nm). (I=8nA, spot size = 0.5 $\mu$ m).....97

Figure 3-15: SEM images of a 20nm thick carbon film on a TEM grid for different incident energies (a:30keV; b: 1keV).....98

Figure 3-16: Diagram of electrons traveling in the SEM column. Electrons emitted from the filament are accelerated to a certain velocity  $V_0$  after passing through the anode (3). Then the electron beam is deflected by a deflection coil system (6) to scan an area on the sample. Without any retarding potential on the stage (7), electrons will travel from the final aperture (5) to the sample with their initial velocity  $V_0$ . But with a negative potential  $U_r$  on the stage, electrons will be decelerated and a landing energy  $U_L$  can be obtained as low as  $(U_a-U_r)$ , where  $U_a$  is the accelerating energy. 1: Cathode; 2: Wehnelt; 3: Anode; 4: Electron beam;5: Final aperture; 6: Deflection coil system; 7: Stage.....99

Figure 3-17: Electron reflection in a SEM with a retarding system. a,b,c and d show the reflection occurs when the landing energy  $U_L$  is

approaching 0 in the SEM (The accelerating energy  $U_a=1.12\text{keV}$ ; the retarding potential  $U_r$  is increasing to  $U_a$ ). e,f and g are some reflected images inside the SEM chamber when  $U_r$  is greater than  $U_a$ ..... 100

Figure 3-18: Diagram of electrons traveling from the final aperture to the stage in the SEM column without (a) and with (b) the retarding potential  $U_r$ . 1: Final aperture; 2: Deflection coil system; 3: Specimen stage. ... 101

Figure 3-19: Experimental and theoretical  $R^2-U_r$  curve (with an accelerating energy  $U_a=1.12\text{keV}$ ), where  $R^2$  is the ratio of area in low-voltage operation to that in normal operation. .... 102

Figure 3-20: The dependence of damage cross-section on the incident energy for a coronene film measured in our SEM by monitoring CL-fading. In the energy range from 1keV-30keV, damage rate measurements were done without any retarding potential, while in the energy below 1keV, measurements were conducted with a constant accelerating energy of 1.12keV and a retarding potential on the stage. .... 103

Figure 4-1: Variation with incident energy of secondary electron yield for silver [Joy 1996]. .... 128

Figure 4-2: Previous damage measurement by the Cavendish group (solid) [Muhid 1988] by monitoring the fading of the diffraction pattern at room temperature and our measurements (hollow data points) at room temperature and 90K..... 129

Figure 4-3: Diffraction Pattern damage cross-section and K-shell ionization cross-section [Muhid 1988].	130
Figure 4-4: Diffraction pattern damage cross-section measured by the Cavendish group [Muhid 1988] and Arizona State University group [Stevens 2000].	131
Figure 4-5: Direct measurement of diffraction pattern damage cross-section in low energy irradiation [Stevens 2000].	132
Figure 4-6: Our CL damage cross-section and previous diffraction pattern damage cross-section measured by the Cavendish group [Muhid 1988].	133
Figure 4-7. The CL damage cross-section, calculated energy deposition rate (for a 60nm coronene) and inelastic cross-section per coronene molecule.	134



## List of Tables

Table 1-1: Some theoretical calculations about ground state energy and the lowest excited state energy in coronene. $E_2$ : the energy of the lowest excited state; $E_1$ : the ground state energy; $\alpha$ : the coulomb integral; $\beta$ : the resonance integral. ....	19
Table 2-1: Thickness monitor reading and EELS thickness measurements. (the supporting carbon film $t/\lambda_i = 0.13$ ). ....	59
Table 2-2: Characteristic doses for different materials by monitoring the fading of $\pi$ -peak ( $E_0=200\text{keV}$ ). The characteristic dose $D_{1/e}$ was measured in our JEOL 2010 TEM; the damage cross-section is $\sigma_D=q/D_{1/e}$ , where $q$ is the electronic charge. * Resonance Energy per $\pi$ electron was calculated according to Wheland (1955). ....	60
Table 3-1: Measurement of characteristic doses for different magnifications. ( $E_0=6\text{keV}$ , spot size = $0.5\mu\text{m}$ ) ....	104
Table 3-2: $\kappa$ values for some solid and liquid organic materials [Herbert 1989]. ....	105
Table 4-1: Dose, $D$ , and corresponding number of electrons $/\text{\AA}^2$ for the damage of different materials and physical properties compared with the dose to get one elastically scattered electron per atom and to blacken a photographic emulsion [Reimer 1975]. ....	135

Table 4-2: Observed saturation dose, D, for radiation damage of different organic compounds ( $E_0$ =electron energy) [Reimer 1975]. .....	136
Table 4-3: Temperature effect on damage dose. ....	137
Table 4- 4: Electron doses required for extinction of the diffraction pattern ( $E_0=100\text{keV}$ ) for samples with carbon coating and without carbon coating [Fryer 1983].....	138

# Chapter 1

## Organic light-emitting materials

### *Introduction*

Organic and molecular materials were originally confined to chemistry and biology. But this situation has changed with the development of polymers, other molecular materials that can emit light and conduct electricity, and thin film devices. These organic materials offer many advantages over their inorganic counterparts: they are durable, flexible and cheap to mass-produce. The light-emitting properties of organic materials can be exploited for use in displays; polymers have already been used as the active materials in transistors, and are now being used for the conducting parts of devices as well.

The lifetime of organic materials is a critical problem for their commercial application. A related problem associated with electron microscopy, when applied to organic and biological specimens, is radiation damage from the area being analyzed. It has been reported that there is no obvious damage to some aromatics below the K-shell ionization energy  $\sim 285\text{eV}$ . If so, a low-voltage (below carbon K-shell ionization) SEM could examine such materials without damage. And at higher incident energy there would be negligible effect from low-energy secondary electrons, leading to high spatial resolution if these materials were used as electron-beam resists.

## ***Organic light-emitting mechanism***

### *The origins of organic luminescence*

Luminescence can be described as cold light, in contrast to light emitted by incandescent bodies which emit light solely because of their high temperature. Luminescence can take on a variety of forms such as photoluminescence, cathodoluminescence, radioluminescence, bioluminescence, thermoluminescence, triboluminescence, sonoluminescence, and electroluminescence [Lumb 1978]. These different forms are concerned with the excitation processes which occur prior to the emission of light.

The difference between organic and inorganic luminescence lies in the molecular and atomic structure of these materials. Inorganic materials are held together by ionic or covalent bonds between individual atoms, and thus can be regarded as "atomic" solids. Organic materials are held together by van der Waals forces between molecules and are therefore molecular solids. The luminescence processes in organic materials are associated with the excited states of molecules.

### *Requirements for luminescence*

Generally, the emission of luminescence is associated with conjugated and aromatic organic molecules. It is an inherent molecular property and arises from the electronic structure of these molecules. Much of the excited energy absorbed by a molecule may be lost by processes other than luminescence. A certain energy fraction of the irradiating particles

is spent in the excitation of delocalized  $\pi$ -electronic singlet states. This excitation is responsible for the luminescence of aromatic, heterocyclic and conjugated molecules. The luminescence process will tend to be favored if a compound has the following properties [Bowen 1968]:

*(1) Structural Considerations*

Saturated organic substances are not normally fluorescent in the solid state or in solution whereas a conjugated system of double bonds commonly gives rise to strong luminescence emission. This luminescence originates from the excited states of the delocalized  $\pi$ -electrons in these molecules. Other factors such as the geometrical arrangement of the molecule and the type and position of substituents can also influence the emission.

*(2) Electronic Considerations*

The excited singlet state of  $\pi$  electrons should be relatively stable to the deactivating processes. If the relaxation half-life is too long, intersystem crossing, which is the non-radiative transfer of energy between the singlet state and the triplet state, will be favored; a shorter half-life implies rapid deactivation of the molecule by other processes [Bowen 1968]. The excited singlet  $S_1$  and triplet states T should be separated in the case of the aromatic hydrocarbons (Figure 1-1), for where the two states are very close together, e.g., in some dyes, intersystem crossing from the excited singlet to the triplet state can occur.

### ***Luminescence processes in aromatics***

Non-conjugated and saturated molecules are formed of single bonds only or may contain isolated double bonds, while in aromatic molecules we cannot speak of a strict localization of the  $\pi$ -electrons between any pair of adjacent carbons. Thus we cannot speak of the existence of discrete “double” bonds. In such a structure, the double bonds are delocalized, which means that no bond in the molecule may be considered as purely single or double; all of them must be considered as bonds of a new intermediate type. When dealing with this type of system, we may divide the electrons into two groups: (a) the  $\sigma$  electrons which form the basic rigid skeleton of localized bonds, and (b) the  $\pi$ -electrons which form a fluid, single system spreading over the  $\sigma$  skeleton. It is the de-excitation of excited states of these  $\pi$ -electron systems that causes the luminescence, as has been discussed in great detail by Birks [1970].

The ground state of any  $\pi$ -electron system is a singlet state  $S_0$ . The resultant excited states are also singlet states ( $S_1$ ,  $S_2$ ,  $S_3$ , etc.) if the  $\pi$ -electrons are excited without change of spin, otherwise the resultant is a triplet state, if the  $\pi$ -electron suffers a spin reversal between the ground and excited state. Figure 1-2 shows the luminescence processes that can occur in the  $\pi$ -electron systems of organic molecules.

Electronic transitions between a singlet and triplet state are formally forbidden by quantum mechanical selection rules [Friedrich 1998]: the selection rules for the orbital angular momentum quantum numbers  $L$ ,  $M_L$ :  $\Delta L=0,\pm 1$ ,  $\Delta M_L=0,\pm 1$ , and the quantum numbers of the total spin  $S$

and  $M_s$  cannot change in a transition:  $\Delta S=0$ ,  $\Delta M_s=0$ . The absorption process, therefore, occurs principally between the ground state  $S_0$  and the singlet states  $S_1$ ,  $S_2$ ,  $S_3$ , etc, but there is still a finite rate constant for intersystem crossing from the excited singlet to lowest triplet state  $T_1$ . This is a non-radiative process. It should be noted that each triplet state lies below the corresponding singlet state -- a situation dictated by Hund's rule [Friedrich 1998]: when the spins of more than one electron from a given sub-shell are coupled to the total spin  $S$ , then the state with the largest value of  $S$  is energetically lowest; of all states with the same value of  $S$ , the state with the maximum value of  $L$  is the energetically lowest. Luminescence may be produced by absorption into any of the excited singlet states  $S_1$ ,  $S_2$ ,  $S_3$ , etc. However, the primary fluorescence emission, in general, occurs from the lowest excited singlet state  $S_1$  irrespective of the initial state excited. The radiative transitions from higher excited states  $S_2$ ,  $S_3$ , etc. are very weak due to the rapid and efficient non-radiative process of internal conversion between  $S_2$ ,  $S_3$ , etc. and the lowest excited state  $S_1$ .

Among the huge variety of existing light-emitting molecules, aromatics are most promising due to the high emission intensity and stability. Coronene whose molecular structure is given in Figure 1-3 [Weast 1988] was chosen as an experimental substance for the following reasons. The molecule is planar with a 6-fold symmetry axis (spacegroup  $D_{6h}$ ), which makes coronene suitable for theoretical calculations [Lackinger 2002]; it can be considered as the smallest possible flake of a graphite sheet saturated by hydrogen atoms. Coronene is well known as a fluorescent material which can be used as the light emitting material in

electroluminescence (EL) devices and charge-coupled devices [Zhou 2001; Yang 2003]. The good stability and resistance to irradiation due to its planar molecule structure and  $\pi$ -electron system make damage-rate measurements easy, while the damage rate is too fast to take enough measurements for those materials with poor stability and less resistance to irradiation damage. In Figure 1-4 [Hawkes and Valdre 1990] various specimens are listed together with the electron doses that cause lethal, destructive or conductive response of the specimen to that dose. The dose needed to destroy crystallinity of aliphatic amino acids is in the order of  $10^{-3}\text{C}/\text{cm}^2$  for 100keV electrons. Scanning with a probe current  $I_p=10^{-11}\text{A}$  in a frame time  $T=100\text{s}$  at a magnification  $M=10,000$  corresponds to a dose  $10^{-3}\text{C}/\text{cm}^2$  [Reimer 1985]. This means that amino acids are already strongly damaged by one high-resolution scan. Two other simple aromatic compounds: rubrene and p-terphenyl (Figure 1-5) [Weast 1988] were also examined, to compare with coronene.

The LCAO method gives very good theoretical results for conjugated systems [Pullman 1963]. By the Linear Combination of Atomic Orbitals (LCAO) approximation and simple molecular orbital treatment, the energies of molecular orbitals in coronene have been calculated theoretically [Moffitt 1948; Baldock 1950]. Table 1-1a shows the calculation results of the energy transition between the energy of the lowest excited state  $E_2$  and the ground state energy  $E_1$ , expressed in terms of  $\alpha$  and  $\beta$  ( $\alpha$  is the coulomb integral, and  $\beta$  the resonance integral) and some experimental values of  $\beta$  in eV. Table 1-1b gives values  $\Delta E=E_2-E_1$  calculated in units of eV. From Figure 1-6 our measured emission



peak is around 505nm, corresponding to a transition energy 2.46eV which is within the calculated range listed in Table 1-1b.

### ***Applications of organic light-emitting materials***

Light emission from organic materials is not very common in everyday life. However, some living creatures, such as fireflies, emit light with amazingly high efficiencies. Light emission from organic single crystals has been studied since the early 1960s, but the high voltages needed to generate the light meant that organic materials did not emerge as realistic candidates for display application until the development of thin-film devices in the late 1980s (Figure 1-7) [Friend 1999]. Organic devices have improved rapidly since their introduction, and this comparison suggests that they have much further potential. While it has been known since the early 1960s that single organic crystals can emit light, the electric fields needed were prohibitively high. But the development of thin-film devices in the last decade has meant that organic materials are now emerging as realistic candidates for display applications [Junji 1999]. The output color can be tuned by adding fluorescent laser dyes, and white light can be produced by having several layers, each doped with a different dye. Multilayer devices are already being used in real applications. The big advantage that polymers offer is that they are easy to fabricate. Indeed, standard inkjet printing technology is being adapted to make the different colored pixels needed for full-color displays [Junji 1999].

There are many other applications for organic electroluminescent devices besides displays. These include illumination devices and light-emitting signs. Devices that emit white light are particularly useful for illumination purposes, and in applications where space is at a premium - for example inside cars and aircraft -- the thinness and low weight of organic devices are really advantageous. Organic lights are also environmentally friendly, unlike conventional fluorescent lamps that use toxic materials such as mercury, and typical power efficiencies are comparable with those of incandescent light bulbs, if not as good as fluorescent sources. Another promising application of semiconducting polymers is in the field of photovoltaics, where they may be used as area detectors or solar cells [Friend 1999].

Organic molecules are not confined to technological applications. Barbara and Gunther [1999] described how certain magnetic nanomolecules were used to investigate the boundary between quantum and classical mechanics.

Thus, molecular and organic materials are making an impact in both fundamental physics and technological applications. In the future, students may well learn about condensed-matter physics from organic display boards in classrooms lit by organic lights, while silicon will be confined to the history books.

## ***Quenching mechanism and damage to organic materials by electrons***

### *Degradation in organic light-emitting devices*

The synthesis of new, as well as the use of novel structures, has greatly enhanced the performance of organic light-emitting devices: almost all the visible range can now be covered by organic light-emitting diodes. The efficiency has also been improved and has become quite acceptable for most of them [Sheats 1996; Burrows 1997; Dodabalapur 1997; Nguyen 1998]. The main problem still to be solved concerns the short lifetime of the diodes.

Although the origin of light decay with time is still not fully understood, earlier studies [Bowen 1968; Lumb 1978; Sheats 1996] have suggested that the most important processes are those of impurity quenching, concentration quenching, and energy transfer. The difference in beam effect in organic samples obtained from different manufacturers indicated that the presence of impurities may have an important influence. A product with a lower-purity-grade resulted in a lower luminescent yield [Lumb 1978]. A damaged crystal can be considered as a mixed crystal in which impurities are introduced by irradiation. Reactions with quenching atoms such as oxygen can also cause the degradation of luminescence in organic materials. The detailed mechanics of the process are rather complicated, but the net result is that oxygen catalyses the non-radiative process of the organic fluorescent molecule. Concentration quenching (or self-quenching) is another

process in solution samples and blends or doped organic solid devices [Shi 1997; Yang 2003]: the fluorescence reaches a maximum intensity at a certain concentration, and then decreases with a further increase of the concentration. A radiationless process is a transition which takes place between energy states without the emission of light. Radiationless processes are, therefore, in competition with the radiative processes responsible for luminescence emission. The intramolecular or intermolecular damage caused by electron irradiation might result in the creation of new energy levels with non-radiative transitions.

*Radiation damage to organic materials by electrons in the Electron  
Microscope*

Electron microscopy is by now a well-established discipline. It can be found in any field of scientific endeavor, from natural science to history. Radiation damage was a specter right from the beginning and has haunted electron microscopy ever since. Especially, beam-induced damage to thin organic specimens, such as polymers or biological tissue, constitutes a major limitation to their imaging in an electron microscope. Many works have been focused on the mechanism of radiation damage to organic and biological specimens in microscopy [Ditchfield 1973; Egerton 1982, 1987, 1999; Reimer 1984; Fryer 1992;] and protection methods [Egerton 1982; Fryer 1983]. It has been reported [Howie 1985, 1987; Muhid 1988; Stevens 2000] that carbon K-shell ionization which requires an electron energy of at least 285eV rather than direct valence excitation is the initial step in the chain of damage events in some aromatic,  $\pi$ -bonded materials. If the conclusion can be confirmed further by more evidence, a low-energy electron microscope (LEEM) will provide a

promising method of imaging and examining organic and biological specimens.

Also photoresists based on aromatic materials will dramatically improve the resolution of e-beam lithography carried out with a proper electron beam. A serious limitation to lithography resolution is due to the broadening of the written line in the resist by electron scattering so that the line-width is greater than the spot diameter [Brewer 1980]. The electron range in a resist is usually greater than the thickness of the resist layer; therefore a large fraction of backscattered electrons return to the resist from the surface of a substrate where the atomic number is usually higher than in the resist. It is obvious that the energy of backscattered electrons is less than primary electrons. Secondary electrons are excited by both primary and backscattered electrons, mostly with energies lower than 50eV. When operating at a sufficient low energy primary beam so that energies of backscattered and secondary electrons are below carbon K-shell ionization energy (~285eV), the resolution limit due to electron scattering might be overcome.

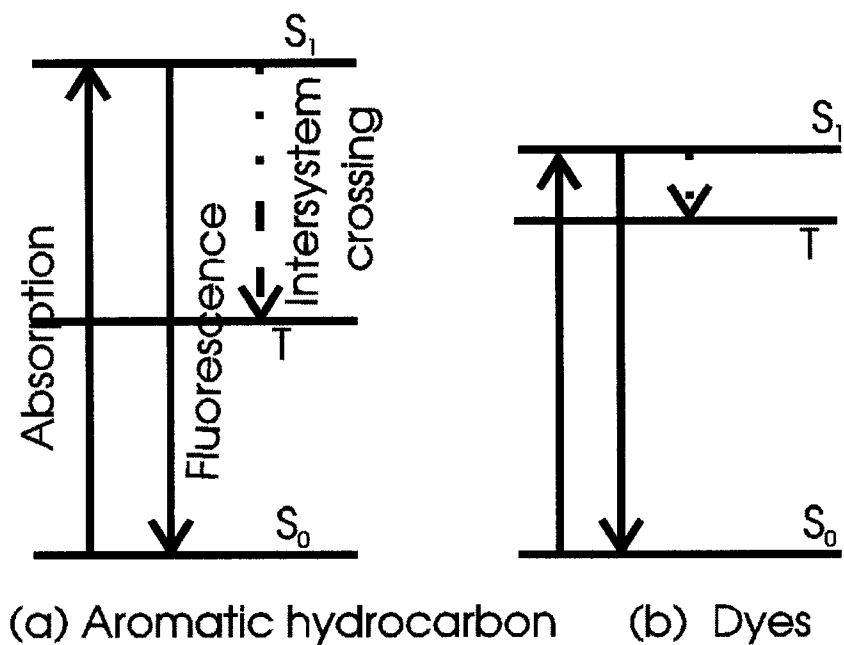


Figure 1-1: Relationship between the excited singlet ( $S_1$ ), triplet ( $T$ ) and ground ( $S_0$ ) states in (a) aromatic hydrocarbons, and (b) dyes. (Broken lines represent unlikely transitions, solid lines likely ones.)

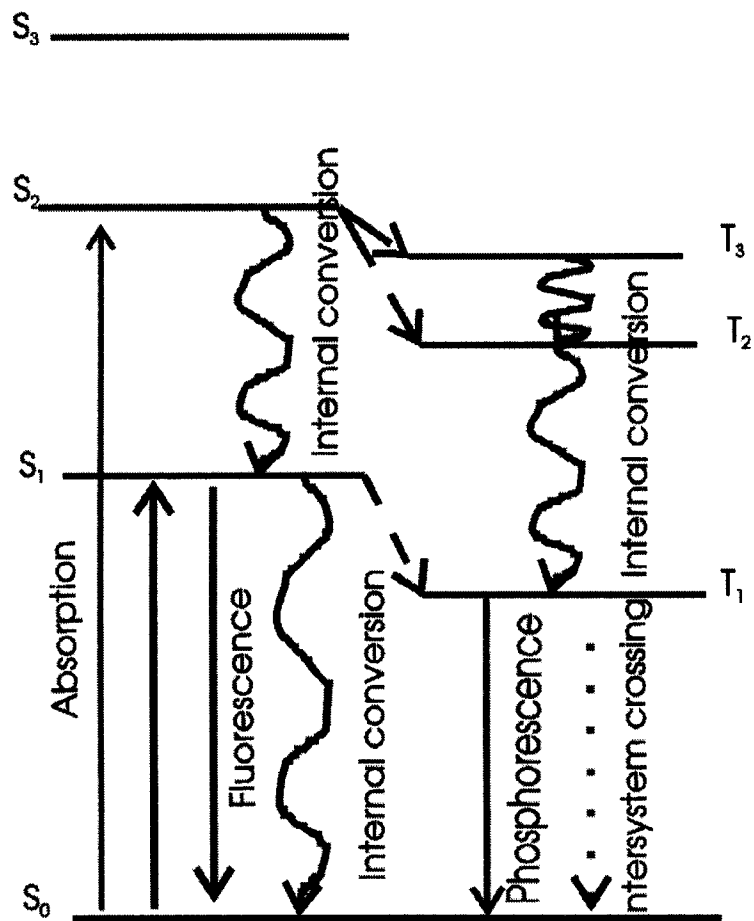
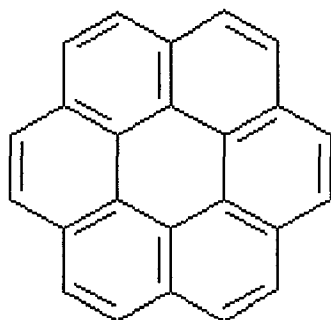


Figure 1-2: Luminescence process in an aromatic material.  $S_0$ : ground state;  $S_1, S_2, S_3 \dots$ : excited singlet states;  $T_1, T_2, T_3 \dots$ : excited triplet states.  $\longrightarrow$  : absorption and emission;  $\rightsquigarrow$  : internal conversion;  $\cdots\rightarrow$  : intersystem crossing.



Coronene  $C_{24}H_{12}$

Figure 1-3: Coronene molecular structure.



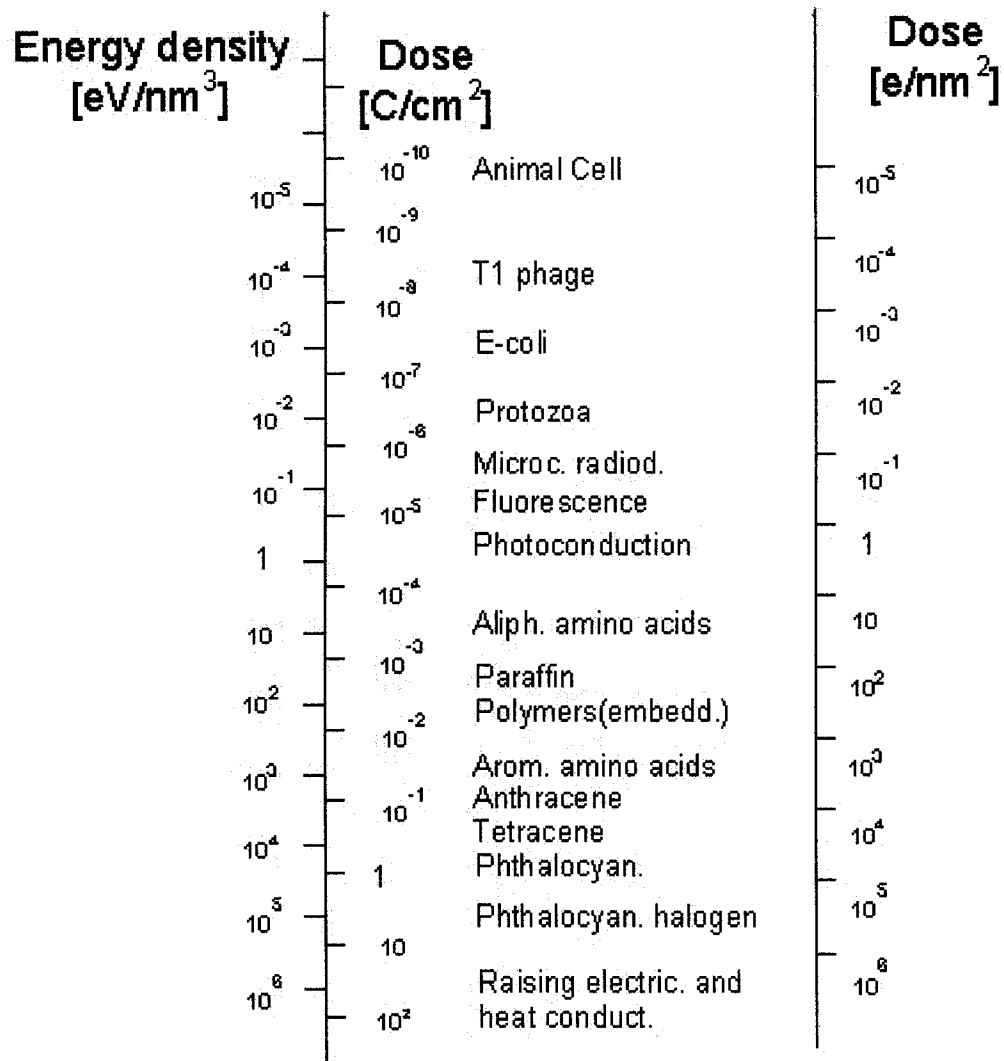
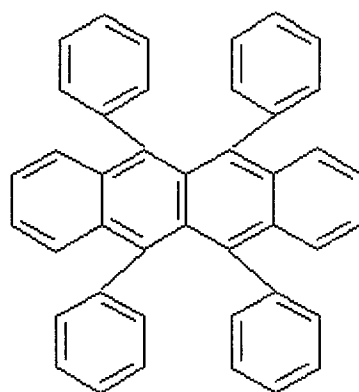
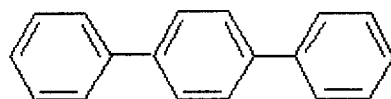


Figure 1-4: Graphic representation of the dose and energy density of 100kV electrons that cause deleterious effects in the listed materials [Hawkes and Valdre 1990].



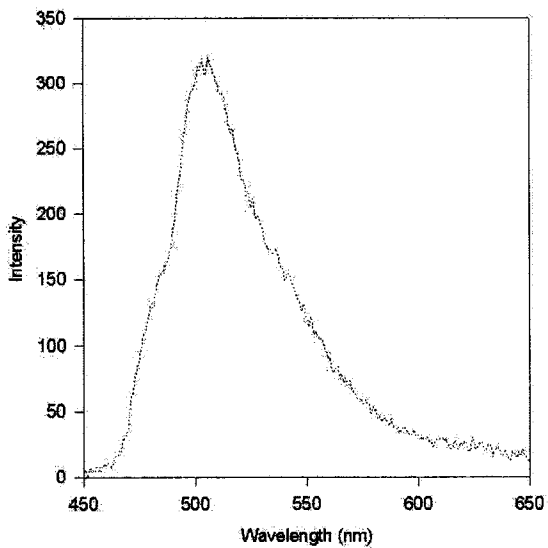
Rubrene  $C_{42}H_{28}$



p-Terphenyl  $1,4-(C_6H_5)_2C_6H_4$

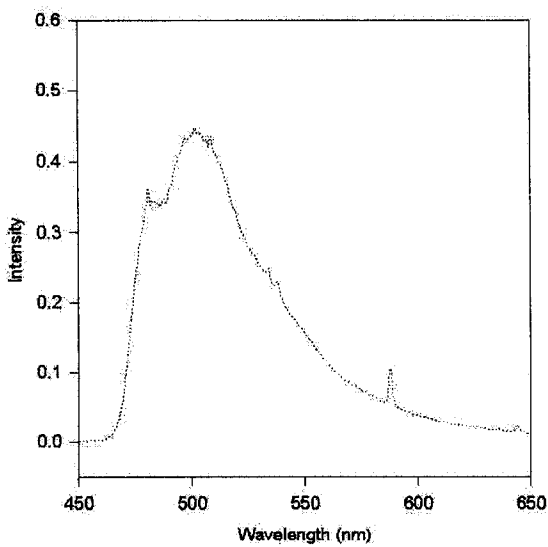
Figure 1-5: Molecular structures of p-terphenyl and rubrene.

**Coronene CL spectrum**



a

**Coronene PL spectrum  
HeCd 442nm laser beam**



b

Figure 1-6: Coronene Cathodoluminescence (CL) (a) and Photoluminescence (PL) (b) spectra.

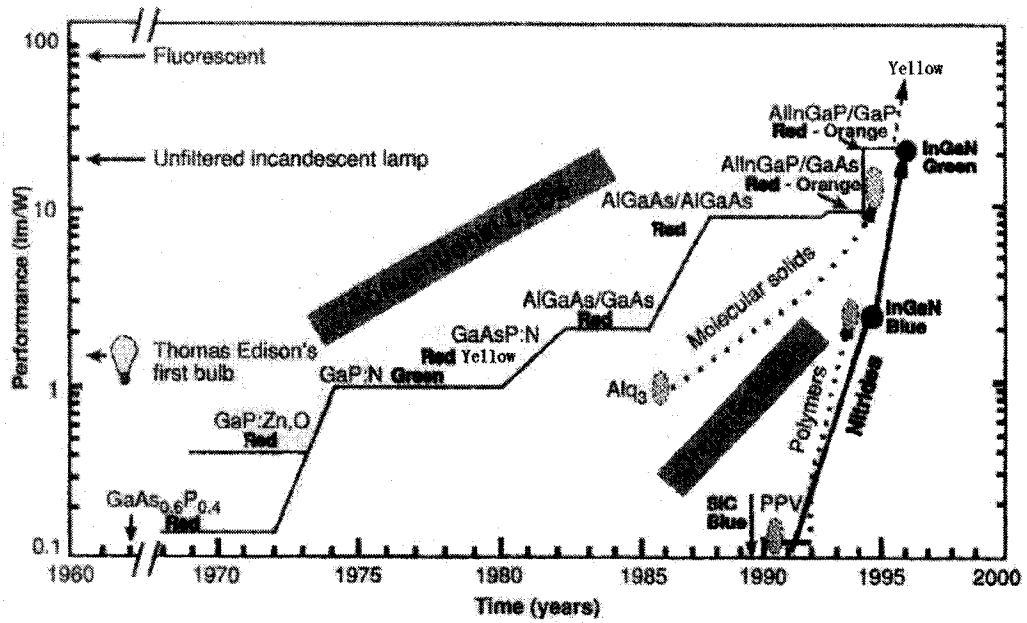


Figure 1-7: The performance of inorganic and organic light-emitting diodes (LEDs), shown here in terms of the "luminous efficiency" in lumens per watt, has been improving steadily over the years [Friend 1999].

$(E_1 - \alpha)/\beta$	$(E_2 - \alpha)/\beta$	$(E_1 - E_2)/\beta$	Ref.
6.64	5.07	1.57	1
16.55	15.47	1.08	2

a

Author	$-\beta$ (eV)	$\Delta E = (E_1 - E_2)$ (Ref.1)	$\Delta E = (E_1 - E_2)$ (Ref.2)
Pauling and Wheland (1933)	1.55	2.43	1.67
Sklar (1937)	1.92	3.01	2.07
Lloyd and Penney (1939)	1.85	2.90	2.00
Baldock (1950)	1.90	2.98	2.05

b

1, Baldock 1949; 2, Moffitt 1947

Table 1-1: Some theoretical calculations about ground state energy and the lowest excited state energy in coronene.  $E_2$ : the energy of the lowest excited state;  $E_1$ : the ground state energy;  $\alpha$ : the coulomb integral;  $\beta$ : the resonance integral.

**Chapter 2.**  
**Sample preparation and radiation damage**  
**measurement by an analytical transmission electron**  
**microscope (TEM)**

***Introduction***

Organic molecules are strongly affected by electron irradiation compared to inorganic materials. The damage process, initiated by electronic excitations, remains one of the important problems in electron microscopy. Several techniques, such as fading of the diffraction pattern and electron energy loss spectroscopy have been used to monitor the damage process. Ultra-thin films (thickness less than electron range – the penetration depth of primary electrons) are required for the measurement with low energy electrons. Vacuum evaporation and solvent evaporation were tried to produce ultra-thin organic films. Film structure and crystal structure were examined in a 200keV TEM. Exponential fading of diffraction pattern and  $\pi$ -resonance peak were observed. Temperature dependence and dose-rate independence of characteristic dose were examined. The damage measurement in the low energy range was tried by a diffraction-pattern fading method, which involved two steps. The irradiation at low energy was initially carried out in a SEM with a retarding system, then the loss of crystallinity was monitored in the TEM. But the sample thickness and heating problems seemed too severe to get any definitive result by diffraction fading in this two-step method.

## ***Sample preparation, film structure and electron diffraction pattern***

### *Vacuum evaporation*

As-received organic materials were used without additional purification (coronene 99%, rubrene 85% and p-terphenyl 99+%). TEM grids coated with thin carbon film, freshly-cleaved KCl or NaCl crystal and SiN membrane were mounted on an aluminum sample holder as substrates. The sample holder was in good thermal contact with a LN<sub>2</sub> tank. Thin organic films were obtained by thermal evaporation in a high-vacuum environment with a typical background pressure between  $0.5-1 \times 10^{-6}$  Torr (Figure 2-1). The material was loaded in a molybdenum thermal boat, which was resistively heated. A MAXTEX TM-100 thickness monitor was mounted at the same level as the sample holder to monitor the deposition rate and thickness. A shutter allowed adjusting the evaporation rate to the desired value before the actual deposition of the organic thin film and can prevent impurities being deposited on the substrates. During the deposition, the deposition rate was kept constant by controlling a "Variac" preceding the step-down transformer.

Figure 2-2 shows TEM images of coronene samples with different thickness (1.4nm, 60nm and 150nm respectively – thickness monitor) prepared on a carbon film at room temperature with a growth rate about 0.1-0.2 Å/s. A thick film (Figure 2-2c) covers all of the

substrate, but it has a granular structure instead of a uniform thickness. It can be confirmed that the film becomes a needle structure when a thin film was prepared (Figure 2-2b). An ultra-thin sample even showed separated islands (Figure 2-2a).

It is very important to grow a coronene sample with a uniform thickness for low-energy electron-irradiation experiments. The electron range is dramatically reduced with decrease of electron incident energy. The damage measurement requires that specimen thickness be less than the electron range. Otherwise, a layer is left un-irradiated after SEM irradiation which makes TEM examination misleading, if based on measurement of the dose required to destroy the crystalline structure. So an ultra-thin film with uniform thickness  $t$  ( $t < R$ , where  $R$  is the electron range) or else a non-uniform thickness (but the thickest area  $t_{\max} < R$ ) is needed for this measurement.

Although the basic physical principles governing organic thin-film growth and crystallization are not well understood, it has been reported that substrate temperature, base pressure and deposition rate [Chang 2003; Park and Lee 1999; Heringdorf 2001] are crucial conditions that can influence the morphology of an organic film. So coronene thin-film growth was studied under different evaporation conditions, such as different substrates, substrate temperatures and deposition rates. Other substrates such as freshly cleaved KCl crystal and SiN membrane were used to grow the sample. All showed similar granular morphologies (Figure 2-3).



At pressures common for evaporation, evaporated material (atoms or molecules) travels from the source to the substrate without collisions, due to the long mean free path compared to the dimensions of the evaporation jar. After an atom or molecule has been condensed on the substrate surface, it may undergo additional processes which involve energy changes such as desorption and migration (diffusion) over the surface. The substrate surface condition, temperature and evaporation rate can have a large influence on the film growth. A high flux rate or a short distance between the thermal boat and the substrate will increase the substrate temperature. An increase in the substrate temperature increases the migration (diffusion) length of the condensed molecules/atoms along the substrate and allows for the formation of a smaller number of nucleation sites in the initial states of growth. So cooling down the substrate and using a low evaporation rate will decrease the mobility of the condensed molecules/atoms and increase the nucleation density.

For many evaporations, an aluminum sample holder was therefore attached to the bottom of a LN<sub>2</sub> tank. Just before the evaporation, the tank was filled with liquid nitrogen. The holder had a good thermal contact with the tank, so the substrate temperature can be as low as 90K. A low evaporation rate means a long evaporation time to reach a certain thickness. To minimize heating of the substrate by radiation from the thermal boat, an aluminum foil was bent around the thermal boat to act as a radiation shield. A hole in the center allowed the flux to travel through to the substrate. Figure 2-4 shows

a coronene film evaporated at a substrate temperature of 90K and at a low rate (0.02 Å/s). It still has a granular structure but the nucleation density and the coverage is increased by a factor of 3.

#### Problem of crystal thickness monitor

##### (a) Estimate of mean free path for coronene:

Due to the fact that thermally evaporated coronene films present a granular morphology instead of a flat continuous surface, their average and local thickness were investigated in a JEOL 2010 TEM by electron energy loss spectrum (EELS) and compared with the thickness deduced from the monitor reading.

If the specimen is of uniform thickness in the area from which the spectrum is recorded, and using simple integration to compare the area  $I_0$  under the zero-loss peak of the electron energy loss spectrum with the total area  $I_t$  under the whole spectrum, the thickness  $t$  is given [Egerton 1996] by

$$\frac{t}{\lambda_i} = \ln\left(\frac{I_t}{I_0}\right) \quad (1)$$

where  $\lambda_i$  is a total mean free path for all inelastic scattering.  $\lambda_i$  must be interpreted as an effective mean free path  $\lambda_i(\theta)$  if a collection aperture is used to restrict the scattering angles recorded by the spectrometer to a maximum angle  $\theta$ .

The collection-angle dependence of mean free path  $\lambda_i(\theta)$  was investigated for a arc-evaporated carbon film with a uniform thickness. Spectra were recorded with different objective apertures inserted and  $t/\lambda_i(\theta)$  was calculated and plotted versus collection semi-angle  $\theta$  (Figure 2-5). In the dipole region (i.e.  $\theta \ll (E/E_0)^{1/2}$ ) the mean free paths can be obtained by using scattering theory to parameterize  $\lambda_i(\theta)$  in terms of the collection semi-angle  $\theta$ , the incident energy  $E_0$  and a mean energy loss  $E_m$  which depends on the chemical composition of the specimen:

$$\lambda_i(\theta) \approx \frac{106F(E_0 / E_m)}{\ln(2\theta E_0 / E_m)} \quad (2)$$

In the above equation,  $\lambda_i(\theta)$  is given in nm,  $\theta$  in mrad,  $E_0$  in keV, and  $E_m$  in eV; F is a relativistic factor  $F=0.618$  for  $E_0=200\text{keV}$ .  $E_m$  can be obtained from the approximate formula [Malis 1988]:

$$E_m \approx 7.6Z^{0.36} \quad (3)$$

where  $Z$  is the atomic number. In the range of small  $\theta$  ( $<15\text{mrad}$ ),  $t/\lambda_i(\theta)$  is roughly a straight line versus  $1/\lambda_i(\theta)$  with a slope  $t=7.8\pm 2.6\text{nm}$ . With the increase of  $\theta$ ,  $t/\lambda_i(\theta)$  saturates at a value 0.067. Then  $\lambda_i = 110\text{nm}$  can be used as an estimate of inelastic mean free path for 200keV electrons in carbon for large  $\theta$ . Because of the lower density of carbon atoms ( $\rho_{\text{coronene}} \approx 1.37\text{g/cm}^3$  and  $\rho_{\text{carbon}} \approx 2.2-3.2\text{g/cm}^3$  [Witke 1999]),  $\lambda_{\text{cor}}=220\text{nm}$  is a good estimate for coronene for large  $\theta$ .

(2) Thickness measurement for films of non-uniform thickness:

As discussed above, equation (1) is valid only if the specimen is of uniform thickness in the area from which the spectrum is recorded. The effect of non-uniform thickness and multiple layers is discussed in the following.

The effect of thinner regions can be visualized by imagining a hole to occur within the analyzed area: electrons passing through the hole contribute to the zero-loss intensity  $I_0$  but not to other orders of scattering. When electrons with current  $I_0$  go through a film with a fraction  $F$  covered, there will be  $(1-F)I_0$  electrons which do not interact with the solid matter at all. They contribute to the zero-loss intensity, which results in a reduced value of  $t/\lambda_i$ . Assuming the specimen has a fraction  $F$  of thick area (thickness  $t_2$ ) and the remaining fraction  $(1-F)$  has thickness  $t_1$ , the zero peak intensity  $I_0$  will be:

$$I_0 = (1-F)e^{-\frac{t_1}{\lambda_i}} + Fe^{-\frac{t_2}{\lambda_i}} \quad (4)$$

if the total intensity  $I_t=1$ . The EELS measured thickness is

$$t_{eels} = \lambda_i \ln(1/I_0) \quad (5)$$

and the actual average thickness is

$$t_{ave} = (1-F)t_1 + Ft_2 \quad (6)$$

Figure 2-6 shows the ratio of thickness by EELS measurement to the average thickness as a function of coverage fraction F for a non-uniform organic film.

Since the scattering probabilities are additive, if several energy-loss processes (each characterized by a different mean free path  $\lambda_i$ ) occur within the energy range over which the spectral intensity is integrated, the effective scattering parameter is

$$\frac{t}{\lambda_i} = \sum_j \frac{t_j}{\lambda_{ij}} \quad (7)$$

If the electron passes through several layers,  $t_j$  represents the thickness of a layer j. The local thickness  $t/\lambda_i$  of a vacuum evaporated coronene film on a carbon substrate was measured in TEM at high magnification. The relative thickness  $t_c/\lambda_c$  of carbon substrate was measured separately using an uncoated carbon film. Then the thickness of coronene is  $t_o/\lambda_o = t/\lambda_i - t_c/\lambda_c$ . The fraction F was measured from a TEM image, and average thickness  $t_{oa} = t_o F$ . Table 2-1 shows TEM-EELS measured average thickness and crystal monitor reading for three different specimens. The ratio of the average thickness measure by EELS experiment to the thickness monitor reading is consistently around 2, within experimental errors. This deviation could represent a "tooling factor", due to the quartz-monitor crystal being located away from the axis of the molecular beam, or/and different sticking coefficient of coronene on the quartz crystal and the carbon substrate.

### *Solvent evaporation*

In a further attempt to make ultra-thin films with uniform thickness, a solvent evaporation method was tried. Different amounts of organic compounds were dissolved in two solvents (xylene and 1,2-dichloroethane). Organic thin films were formed by the slow evaporation of small drops of these solutions, placed on the surface of distilled water. Preliminary checks on the thickness of the solvent-grown crystals were made by observing the reflection of light. Thickness of the films can be controlled by the concentration of solution, number of drops and the temperature of the distilled water. Only those with large area (1-2mm diameter) and flat surface were picked up by bare TEM grids (400 meshes or more) or lacey carbon grids.

Figure 2-7 shows a solvent-evaporated coronene film on a bare TEM copper grid. Only a small amount of film was left near the grid bar or at the corner of the mesh, due to the poor mechanical strength of the film. Also the film was easily broken, even by very low TEM illumination. The typical thickness  $t$  measured by EELS was around 60-80nm. Grids coated with lacey carbon film were better for supporting solvent-evaporated films. There were various sizes of holes inside one single mesh (Figure 2-8) which provides a good support to free-standing ultra-thin films. Figure 2-9 shows a coronene film (around 40nm) on a lacey carbon grid.

### *Electron diffraction pattern and crystal structure*

Both vacuum and solvent-evaporated coronene films show a polycrystalline structure (Figure 2-10). Because of its continuity and lack of a supporting thin carbon film, a free-standing film with similar thickness prepared by solvent evaporation presented a better diffraction pattern (a) than that (b) of a vacuum-evaporated onto carbon substrate.

The interplanar d-spacing corresponding to a transmission diffraction ring pattern was calculated based on the equation:

$$d_{hkl} = \frac{2\lambda l}{D_{hkl}} \quad (8)$$

giving  $2\lambda l = (594.2 \pm 0.9)$  ( $\text{\AA} \cdot \text{pixel}$ ) for 200keV electrons when  $l = 100\text{cm}$ , where  $d_{hkl}$  is the plane spacing in  $\text{\AA}$ ,  $l$  the camera length,  $\lambda$  the wavelength of incident electrons and  $D_{hkl}$  the ring diameter in pixels. Most of the innermost ring was blocked, so the measurement of damage rate by diffraction fading was conducted in one of the points in the second innermost ring. From the diffraction pattern of a free standing sample (Figure 2-10a), the second innermost ring might include two individual rings, but they are very close. The resultant  $d_{hkl}$  value is  $3.7 \pm 0.2 \text{\AA}$ , which is found to be in agreement with the known structures of coronene [Fawcett and Trotter 1965; Stevens 2000].

### ***Fading of electron diffraction pattern***

Electron diffraction gives direct evidence of the rate of damage, but only in a crystalline specimen [Cosslett 1978; Reimer 1984]. Fading of the diffraction pattern reflects the destruction of crystallinity. The critical dose  $D_c$  necessary for complete fading of an electron diffraction pattern has been a common estimate of the decay process [Siegel 1975; Cosslett 1978; Reimer 1984; Howie 1985, 1987; Muhid 1988]. But values of  $D_c$  vary greatly from observer to observer, depending on the visual acuity of the observer, the brightness and contrast of the viewing screen, and the specimen thickness (which affects the spot/background ratio in the diffraction pattern). We therefore adopt a more quantitative procedure.

Our JEOL 2010 TEM, equipped with a CCD camera, was used to conduct electron diffraction experiments at 200keV. In order to maintain low electron doses, the filament was kept undersaturated and a suitable magnification was selected. By operating the microscope in diffraction mode and by adjusting the condenser lens and diffraction lens, the specimen was examined to find a suitable area. In order to avoid pre-irradiation of the specimen before the commencement of the actual recording, the specimen was moved to a new area every time before starting a new measurement. During the irradiation the fluorescent-screen absorbed-current reading was monitored and converted to beam current, based on separate calibrations. The area  $S$  irradiated by electrons was estimated from the illuminated area with a diameter  $d$  on the fluorescent screen and



the magnification  $M$  according to equation  $S=\pi d^2/4M^2$ . Therefore, the beam current density was given by the beam current divided by the area. A series of diffraction patterns were recorded by a CCD camera at increasing irradiation. Before conducting any further analysis, a background was subtracted from each diffraction pattern, which was recorded after a large exposure dose. The intensity of a particular spot was measured by PHOTOSHOP – by putting the sensor on the interesting area, the intensity can be monitored in the “Info Window”, and plotted on a logarithmic vertical scale versus irradiation dose  $D$ . The beam current was checked before and after recording the series of diffraction pattern. The irradiation dose  $D$  was calculated, assuming a linear increase/decrease in incident-current density if any change in beam current was detected between the start and end of the electron exposure. Figure 2-11 shows the series of original recorded diffraction patterns and those after subtracting the background. Figure 2-12 shows that the intensity versus dose curve is a very good straight line if plotted on a logarithmic vertical scale, which indicates an exponential decay of the diffraction pattern with increasing irradiation dose:

$$I_D = I_0 e^{-D/D_{1/e}} \quad (9)$$

where  $I_0$  is the initial intensity and  $I_D$  is the intensity after the dose  $D$ . A new value  $D_{1/e}$  is introduced here to characterize the damage rate which is more consistent between different observers and methods. The characteristic dose  $D_{1/e}$  at which the spot intensity would reach

a fraction  $1/e = 0.37$  of its initial value can be obtained from the downward slope of intensity-dose curve.

### ***$\pi$ -peak monitoring by EELS***

Electron energy-loss spectroscopy (EELS) has been used to monitor structural damage to organic materials [Payne 1993; Egerton 1999]. The peak at 6eV loss is a feature known as the " $\pi$  plasmon" and characteristic of C=C bonding [Ditchfield 1973; Ritsko 1978; Sohmen1992]. By recording the fading of this 6eV peak as a function of electron dose, a characteristic dose  $D_{1/e}$  was calculated and compared to those measured by other methods.

For these measurements, coronene, rubrene and p-terphenyl films of thickness 50-100 nm were thermally evaporated on to TEM grids coated with thin carbon films. Electron energy-loss spectra were recorded in a JEOL-2010 TEM fitted with a Gatan model 666 electron energy-loss spectrometer. Figure 2-13 shows a typical low-loss spectrum recorded at the beginning of an irradiation.

During the irradiation the irradiation dose  $D$  was measured and calculated in the same way as the diffraction-pattern fading experiment. A series of spectra were obtained over a period of a few minutes. Each spectrum was acquired in a period of 4 seconds. The beam current was checked before and after recording the spectrum to correct for any drift in beam current. The background was subtracted from each spectrum before any analysis. The area under the 6eV loss peak, which was separated from the tail of the zero-loss

peak by a program "Afit" (Figure 2-14), was plotted logarithmically against electron dose. As illustrated in Figure 2-15, the resulting plot was approximately linear, corresponding to an exponential decay of the  $\pi$ -peak intensity with a characteristic dose  $D_{1/e}$  measurable from the downward slope. Figure 2-16 shows the measured values of  $D_{1/e}$  by diffraction-pattern fading and 6eV-peak fading.

The characteristic doses for 200keV electrons for coronene, rubrene and p-terphenyl are listed in Table 2-2. According to molecular orbital theory [Pullman1963], the resonance energy per  $\pi$ -electron of a molecule determines the ability of the molecule to withstand radiation damage. Based on the molecular orbital theory [Wheland 1955], the resonance energy per  $\pi$ -electron were calculated. As we see from Table 2-2,  $D_{1/e}$  for coronene is greater than  $D_{1/e}$  for rubrene and p-terphenyl, as expected since the resonance energy per  $\pi$ -electron is greater for coronene than rubrene and p-terphenyl. This correlation was also noted in previous studies of bio-samples [Isaacson1972].

### ***Damage measurement at low energy***

Measurement of the radiation damage cross-section at low incident energy was tried as a two-step measurement. The sample was pre-irradiated at low energy in our PHILIPS 505 SEM with a retarding system. Then the diffraction pattern was examined in JEOL 2010 TEM (200keV) to measure the damage. Figure 2-17 shows specimens irradiated after a dose of  $0.36 \text{ C/cm}^2$  at 700eV, at which the

Cavendish group [Muhid 1988] reported that there is no obvious damage in coronene for 100keV electrons. By examining the diffraction pattern after the irradiation in the TEM, we found that the diffraction pattern did decay. But the beam-heating problem and contamination may make this kind of measurement complicated. The grain size of the sample after pre-irradiation became 1-2 times larger than that before pre-irradiation, suggesting the sample might suffer melting or beam-assisted migration during the irradiation. The thickness in the term of  $t/\lambda_i$  increases from 0.34 to 0.50 for specimen a and 0.40 to 0.65 for specimen b, which also indicates possible hydrocarbon contamination, which can easily result in a thickness larger than electron range.

### ***Temperature dependence of the damage rate***

The idea of reducing the specimen temperature in order to reduce damage caused by the electron beam in the microscope has been the subject of many investigations. It was reported that many organic specimens are less sensitive to radiation damage when kept at low temperature during microscopy [Egerton 1982; Fryer 1992; Wade 1984].

A low temperature holder was used for this measurement. Liquid nitrogen was added to the sample holder to cool down the sample. The temperature of the specimen was controlled and monitored by a Gatan 626-5000 cold stage control unit. Figure 2-18 shows the diffraction-pattern intensity-fading curves for a thin coronene film at

different temperatures. Unlike the curve measured at room temperature, the curve at 90K is not a straight line but shows a latent dose effect [Reimer 1975; Wade 1984]. They found that there is apparently little change in the crystalline structure for some organic materials for about the first half of the critical exposure  $D_c$ . A similar result was obtained in the  $\pi$ -peak fading (Figure 2-19). At small dose the intensity of diffraction patterns or  $\pi$ -peak area is roughly constant or decreases very slowly. At the large dose range the rate of damage becomes close to the room temperature curve. As a result, a larger critical dose  $D_c$  occurs when the sample is kept at low temperature.

The energy transfer in inelastic electron scattering primarily causes ionization and rupture of chemical bonds. Then cross-linking and scission occur [Reimer 1975]. Ionization and rupture of chemical bonds will produce free radicals. The chemical reactions occurring between adjacent free radicals causes the complete destruction. Cooling the sample to a low temperature will severely restrict the degree of molecular motion. At low temperature free radicals will be primarily produced and "frozen" until the concentration becomes sufficiently great that nearest neighbor reactions become highly probable. This may explain the latent dose range in the beginning, in which the damage rate is reduced dramatically, and a following complete damage with a slope close to that at room temperature.

### ***Dose-rate independence***

The effect of dose-rate (beam current density) to the damage process was investigated. The irradiated area in the sample was kept constant by fixing the magnification  $M$  ( $\times 10K$ ) and the beam diameter  $d$  (2.5cm) on the phosphor screen. Then, the beam current density  $J=4IM^2/(\pi d^2)$ , where  $I$  is the beam current, depends only on the beam current  $I$  which can be monitored from the absorbed-current reading obtained from the small phosphor screen. By adjusting the filament current, different beam currents were obtained. Figure 2-20 shows the measured characteristic doses at different beam current densities by DP methods. Similar to the results from diffraction pattern experiment, Figure 2-21 shows the measured characteristic doses at different beam current densities by  $\pi$ -peak fading. In both cases, the damage rate appears to depend only on the accumulated dose and not on the dose rate.

It was reported [Payne 1993] that increasing current density leads to a reduction in  $D_{1/e}$ , but the most obvious process causing a decreased  $D_{1/e}$  is a thermal effect. It is obvious that the temperature is likely to be higher when the specimen is subjected to a greater current density, when other conditions are kept same in damage-rate experiments. While an increase in specimen temperature will have little or no effect on the cross-section for the EELS processes, it will lead to an increase in segmental movement of the organic molecules. The free-radical ends, produced by the bond breaking, would then

have an increased chance of interacting with nearby molecules, which will result in a rapid damage rate.

But for the illumination conditions in our EELS and diffraction pattern experiments, the temperature differences between the different current densities are believed to be insignificant. So the damage rates did not change when the specimen was irradiated at different dose rates. The temperature of a TEM specimen in the region of the electron beam is difficult to estimate. Some discussion of thermal effects will be given in Chapter 3.

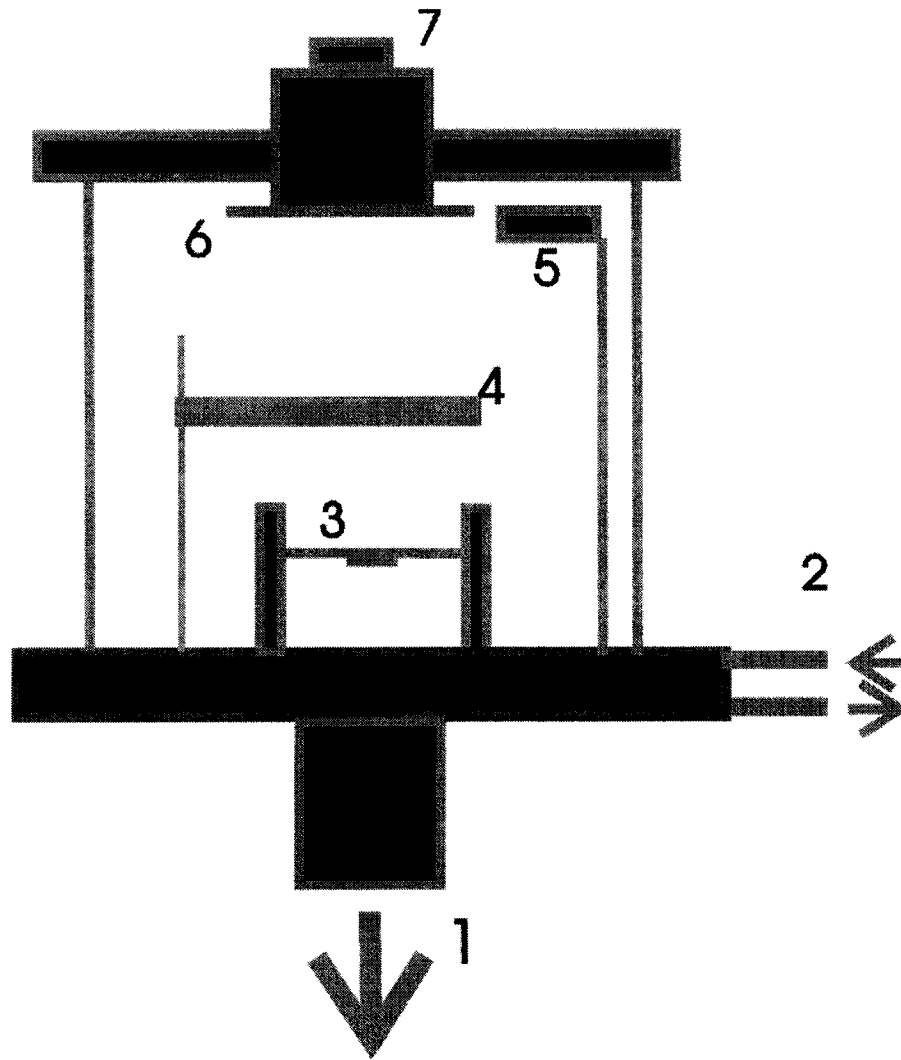
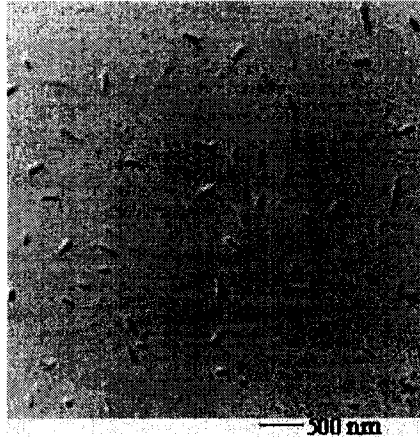
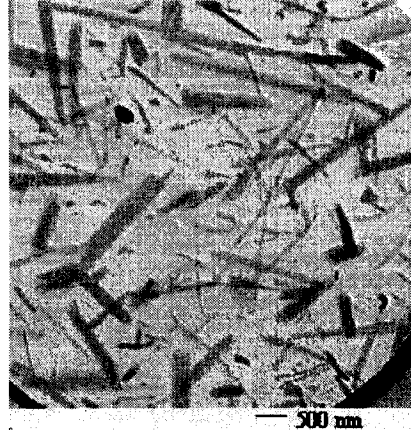


Figure 2-1: Diagram of the vacuum evaporation apparatus. The vacuum of the chamber was maintained by a diffusion pump (1); source materials were loaded in a molybdenum boat (3); a shutter (4) allowed adjusting the deposition rate to the desired value before actual deposition; a crystal thickness monitor (5) was used to monitor the deposition rate and thickness; an aluminum sample holder (6) was in a good thermal contact with a LN<sub>2</sub> tank (7) allowing cooling the substrate down. 1: Diffusion pump; 2: Cooling water; 3: Thermal boat; 4: Shutter; 5: Thickness monitor; 6: Sample holder; 7: Liquid nitrogen tank.

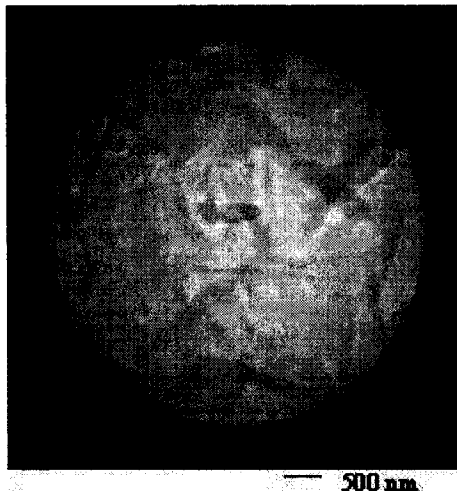




a

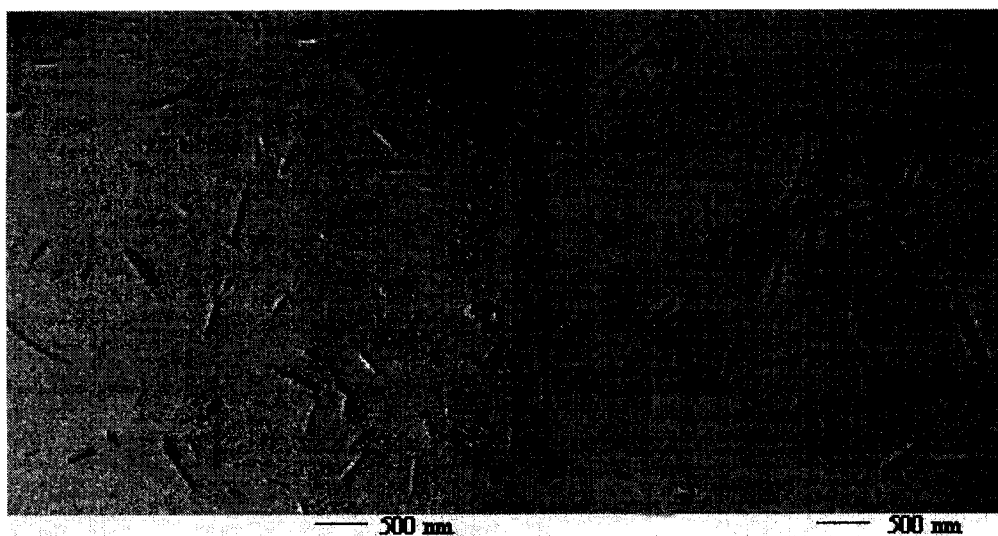


b

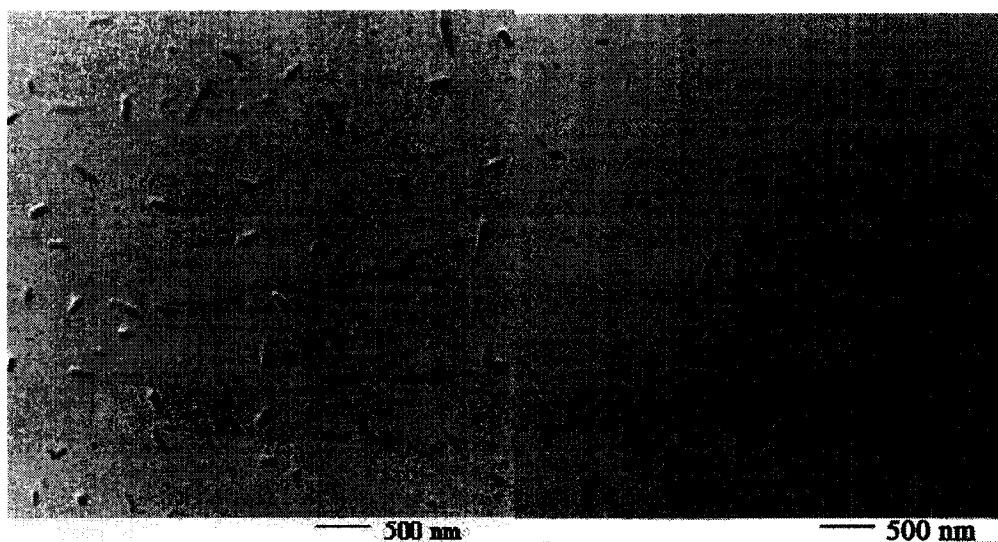


c

Figure 2-2: Morphologies (TEM images) of vacuum-evaporated coronene films (on carbon) with different average thickness: a: 1.4nm; b: 60nm; c: 150nm (from thickness monitor), prepared in room temperature and with a deposition rate of 0.1-0.2 Å/s.



(a)



(b)

(c)

Figure 2-3: 2nm (from thickness monitor) coronene films on different substrates: C-film (a); Cleaved KCl crystal (b); SiN membrane (c). (All were prepared at room temperature and deposition rate of 0.1-0.2 Å/s.)

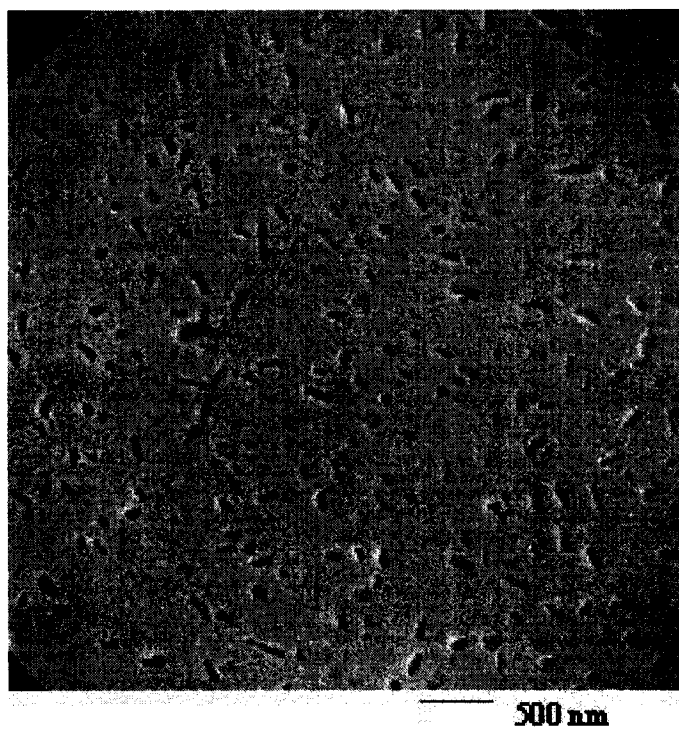


Figure 2-4: A 1.6nm (from thickness monitor) coronene film on carbon film prepared at 90K and deposition rate of 0.02 Å/s.

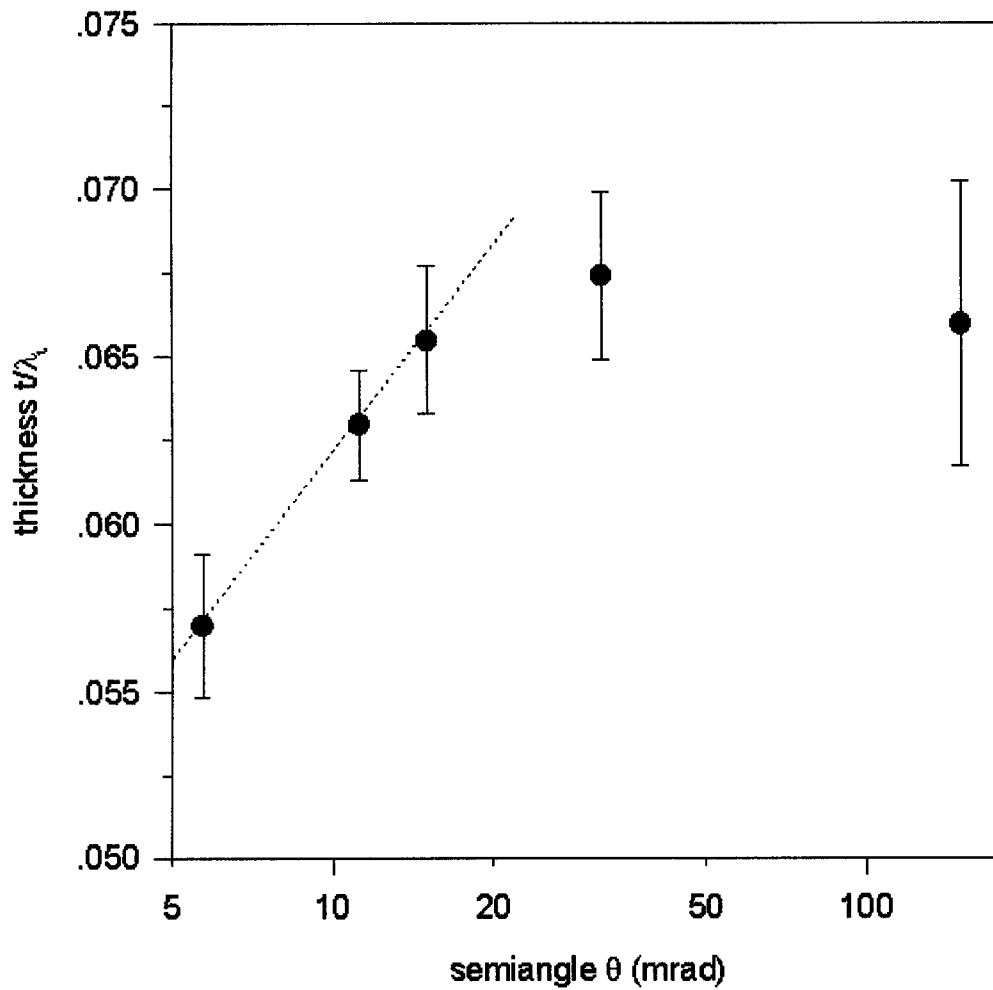


Figure 2-5: Collection angle dependence of film thickness measured by EELS ( $E_0 = 200\text{keV}$ ; carbon film). Thickness is in terms of  $t/\lambda_i$ , where  $\lambda_i$  is the inelastic mean free path.

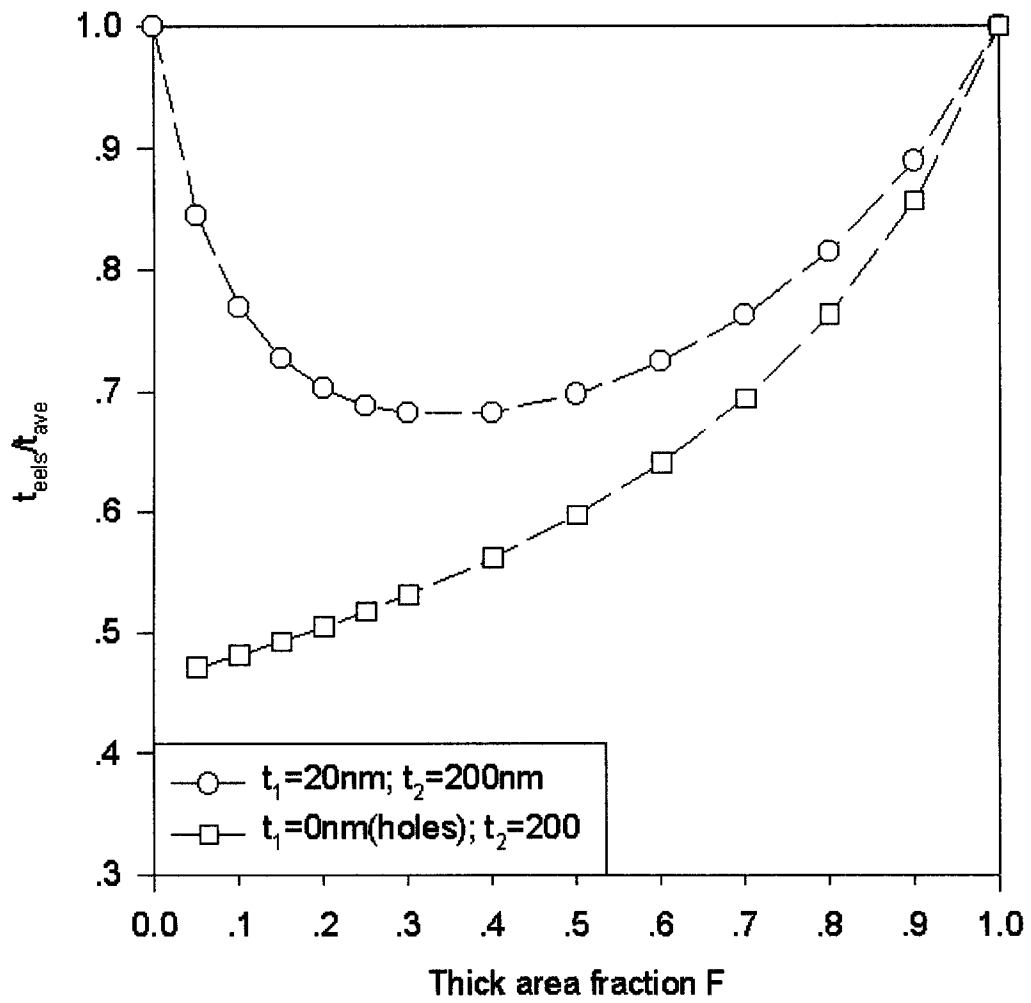


Figure 2-6: Theoretical calculation of coverage fraction dependence of measured thickness by EELS for non-uniform film.  $t_1$ : thin area;  $t_2$ : thick area;  $t_{\text{eels}}$ : thickness measured by EELS;  $t_{\text{ave}}$ : average thickness.

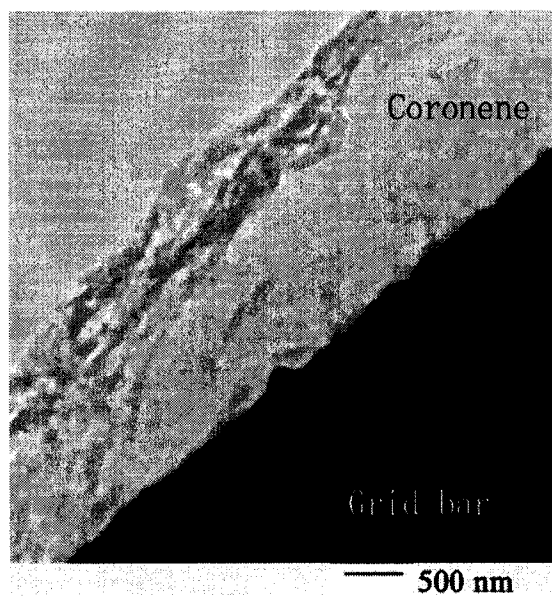


Figure 2-7: A solvent-evaporated coronene film on a bare TEM Cu grid. The water temperature: 5°C; solvent: 1,2-dichloroethane; the specimen thickness: 70nm.

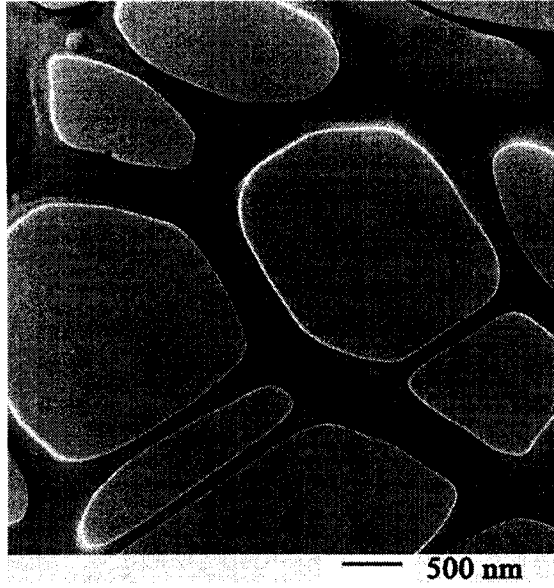


Figure 2-8: A lacey carbon film.

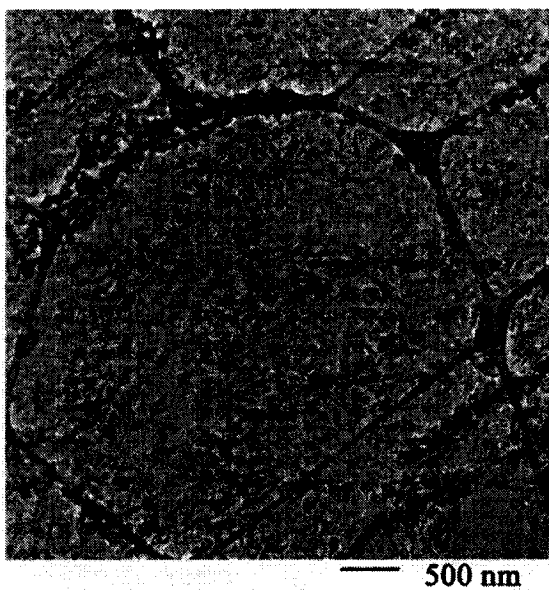
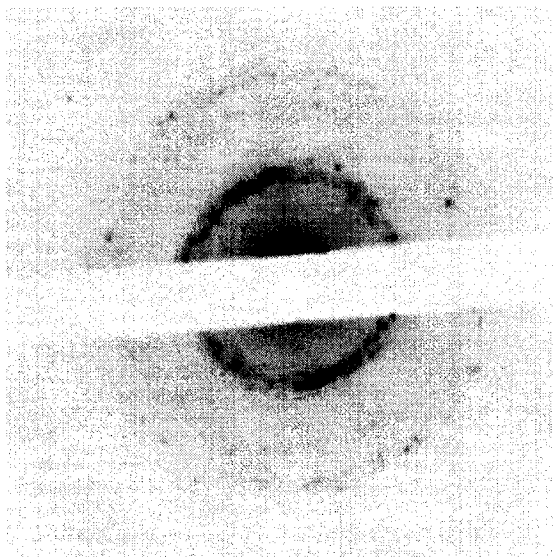
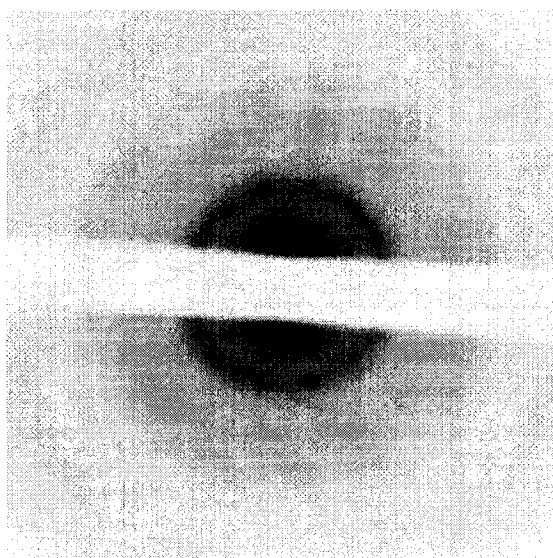


Figure 2-9: A solvent evaporated coronene film on a lacey carbon grid. Specimen thickness: 40nm; water temperature: 5°C; solvent: 1,2-dichloroethane.





(a)



(b)

Figure 2-10: Diffraction patterns of coronene films on regular and lacey carbon grids: (a): Lacey carbon film; (b): regular carbon supporting film.

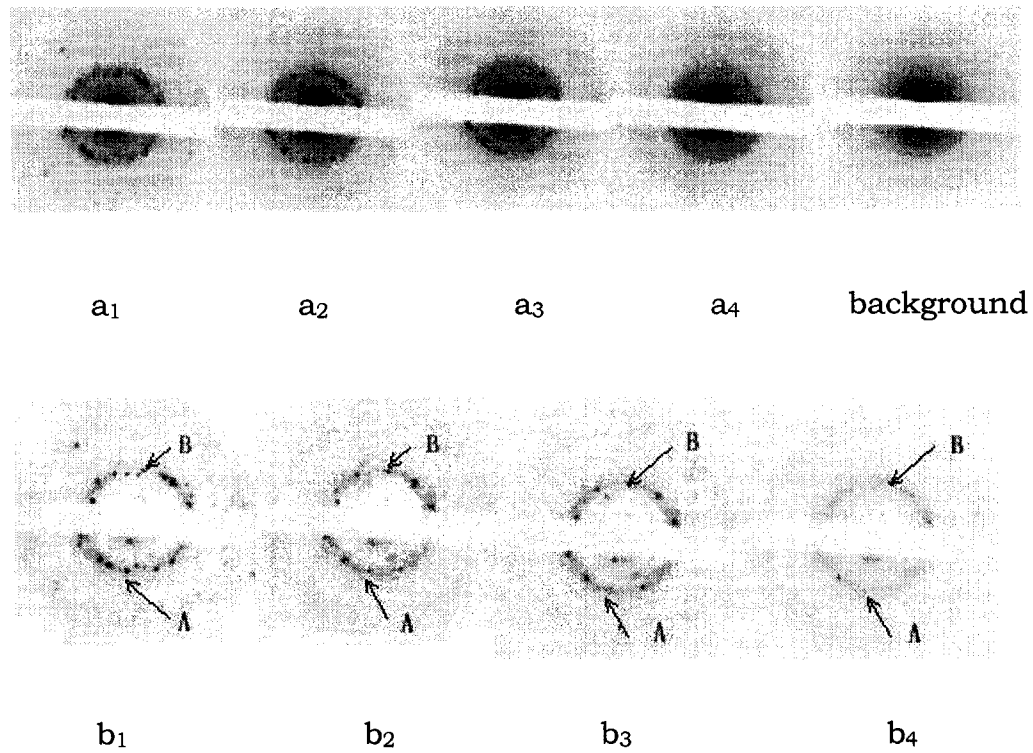


Figure 2-11: Diffraction pattern fading (coronene) with the increase of irradiation dose ( $E_0=200\text{keV}$ ). A series of diffraction patterns  $a_1$ ,  $a_2$ ,  $a_3$ ,  $a_4$  were irradiated after dose 0 ( $a_1$ ),  $0.12\text{C}/\text{cm}^2$  ( $a_2$ ),  $0.24\text{C}/\text{cm}^2$  ( $a_3$ ) and  $0.48\text{C}/\text{cm}^2$  ( $a_4$ ); a background was recorded after a large dose.  $b_1$ ,  $b_2$ ,  $b_3$  and  $b_4$  show the diffraction after subtracting the background.

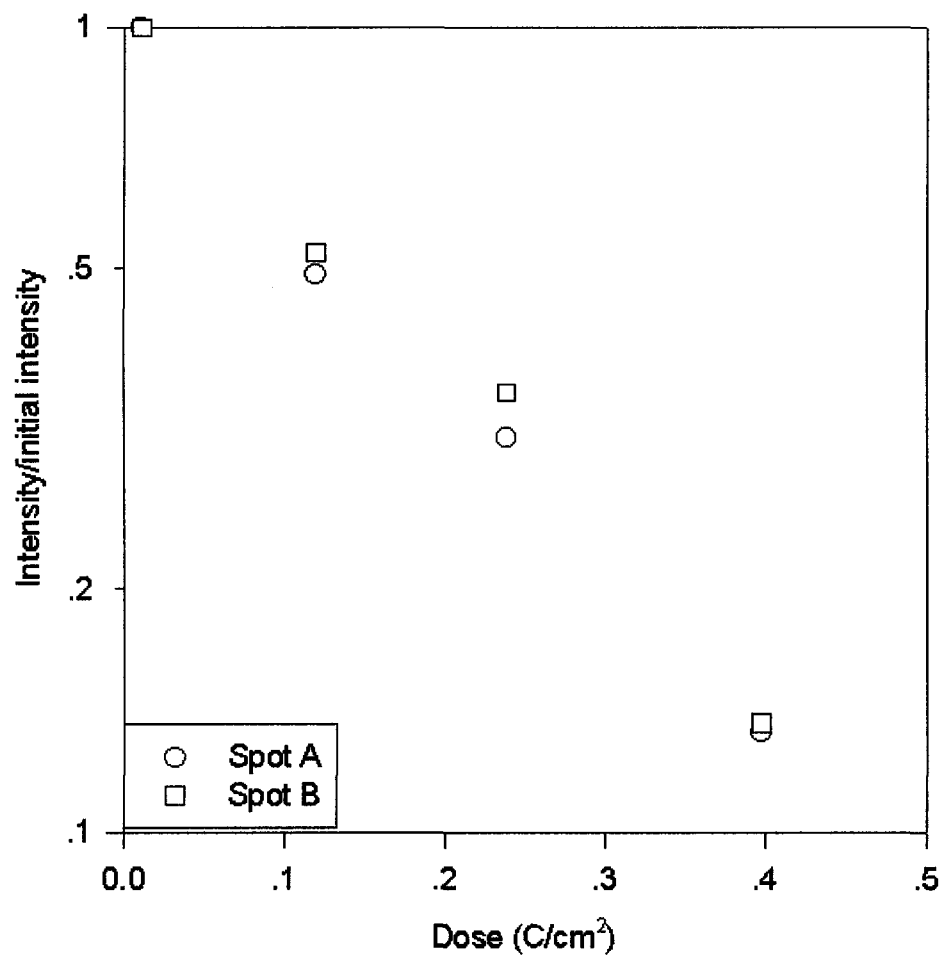


Figure 2-12: Intensity vs. dose curve of diffraction fading (coronene).  $E_0=200\text{keV}$ .

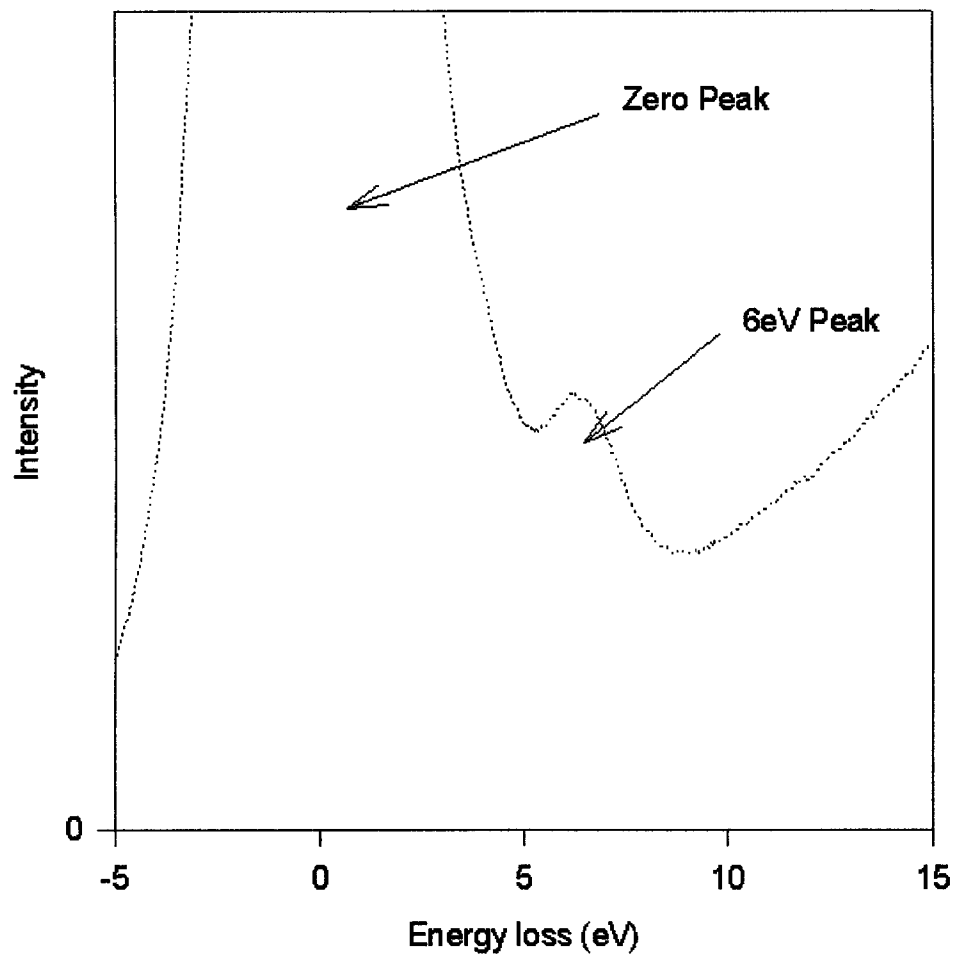


Figure 2-13: Low-energy loss spectrum of coronene.

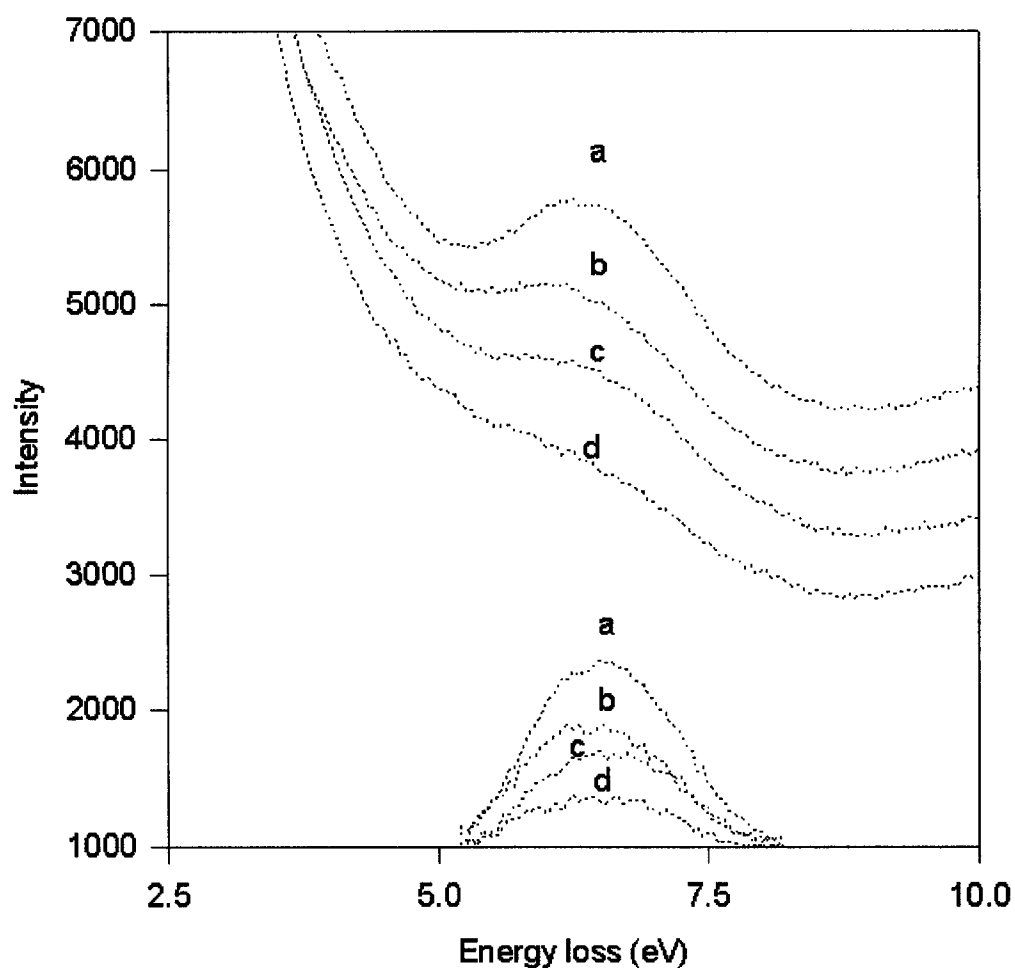


Figure 2-14: 6eV-peak fading (coronene) with the increase of irradiation dose ( $E_0=200\text{keV}$ ). A series of energy-loss spectra a, b, c and d were recorded (upper) after dose 0 (a),  $0.292\text{ C/cm}^2$  (b),  $1.31\text{ C/cm}^2$  (c) and  $1.75\text{ C/cm}^2$  (d); 6eV-peaks (lower) can be separated from the tail of the zero peaks.

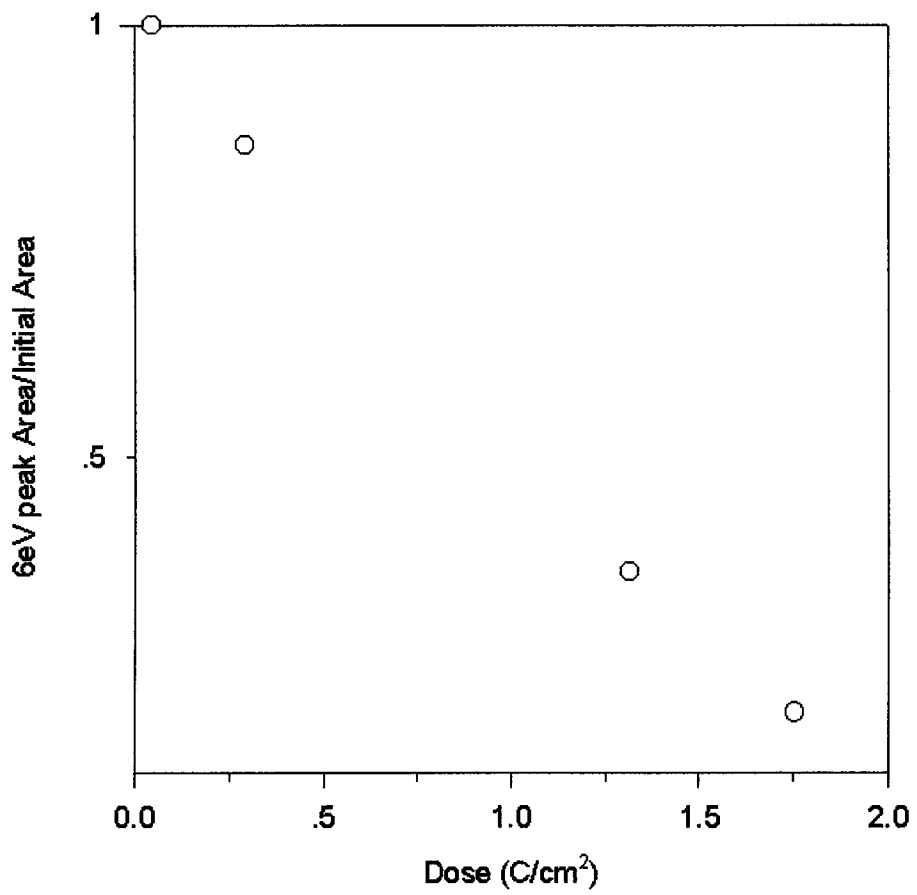


Figure 2-15: 6eV-peak intensity vs. dose (coronene).  $E_0=200\text{keV}$ .

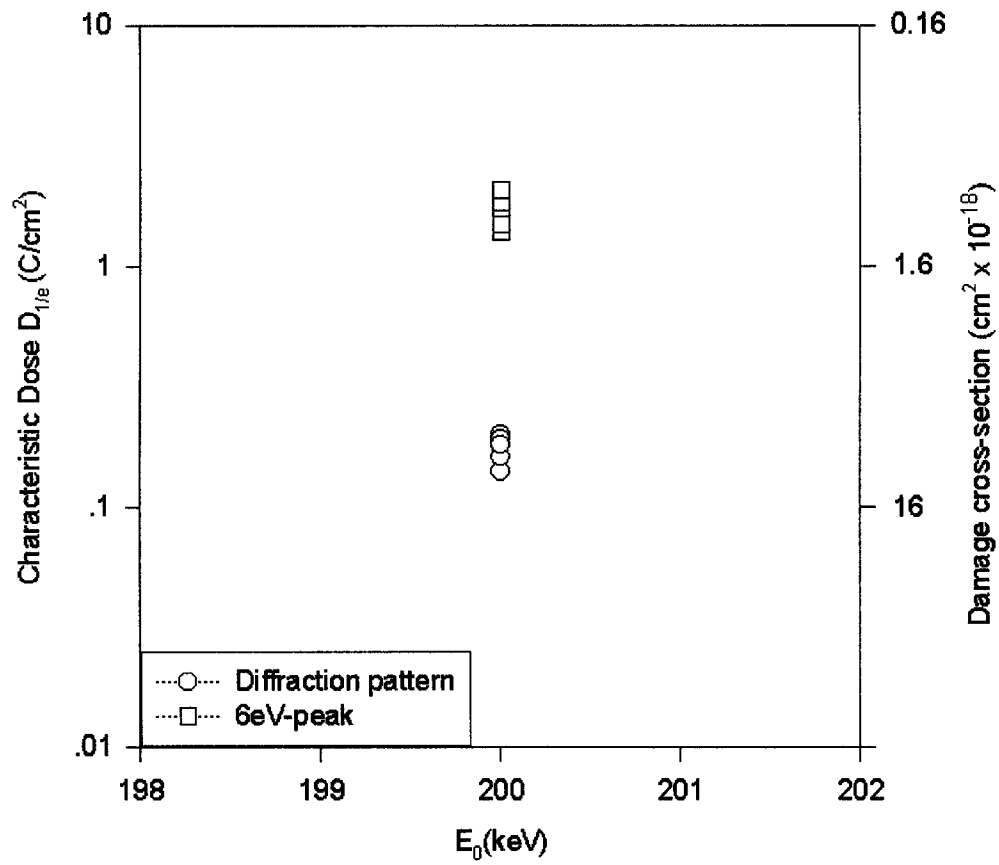
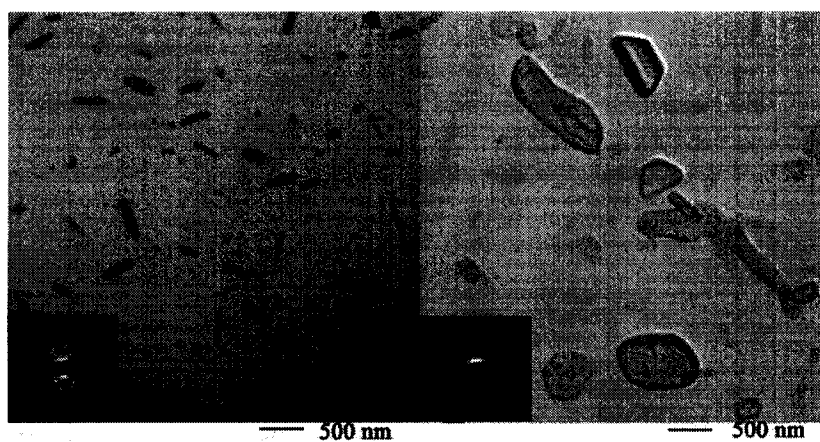
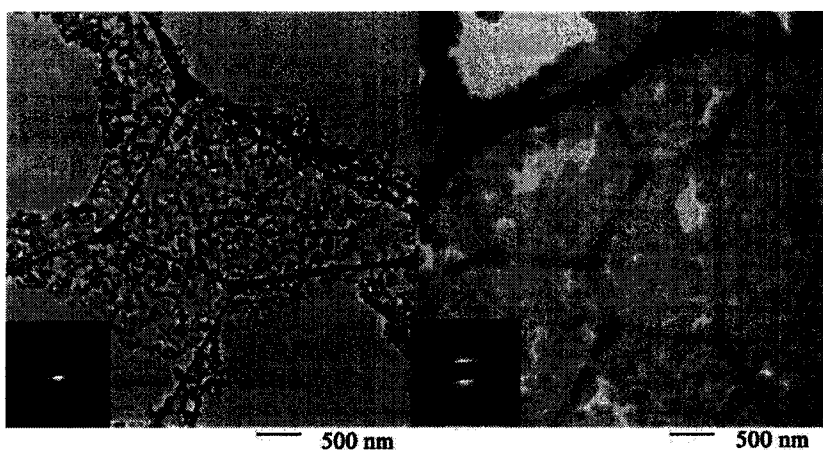


Figure 2-16: Characteristic doses  $D_{1/e}$  and corresponding damage cross-sections measured by diffraction-pattern fading and 6eV-fading (coronene).  $E_0=200\text{keV}$ .



a<sub>1</sub>

a<sub>2</sub>



b<sub>1</sub>

b<sub>2</sub>

Figure 2-17: TEM images of coronene specimens before and after pre-irradiation for a dose of  $0.36 \text{ C/cm}^2$  at  $0.7 \text{ keV}$  in a low-energy SEM. Diffraction patterns are inserted. A vacuum-evaporated coronene specimen on carbon film: before (a<sub>1</sub>) & after (a<sub>2</sub>) irradiation; a solvent-evaporated coronene specimen on lacey carbon film: before (b<sub>1</sub>) & after (b<sub>2</sub>) irradiation.



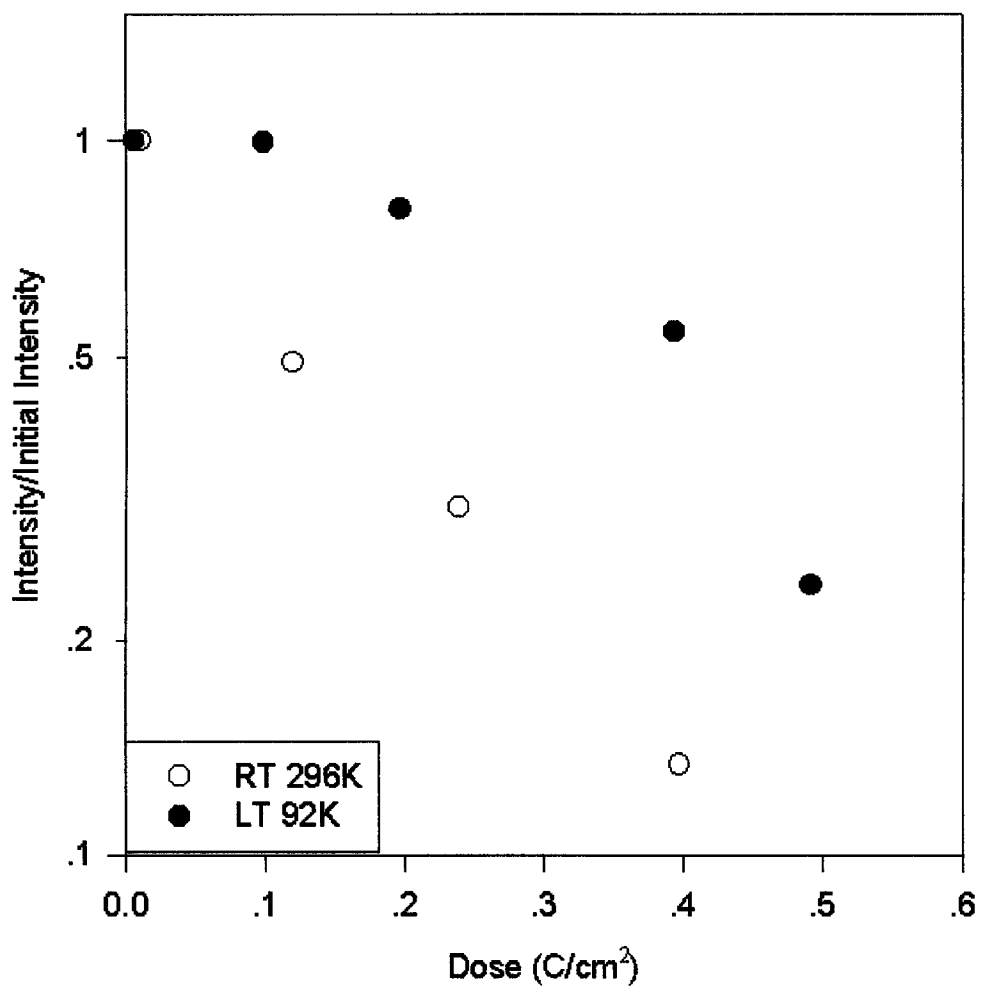


Figure 2-18: Temperature dependence of damage rate for coronene by diffraction-pattern fading.  $E_0=200\text{keV}$ .

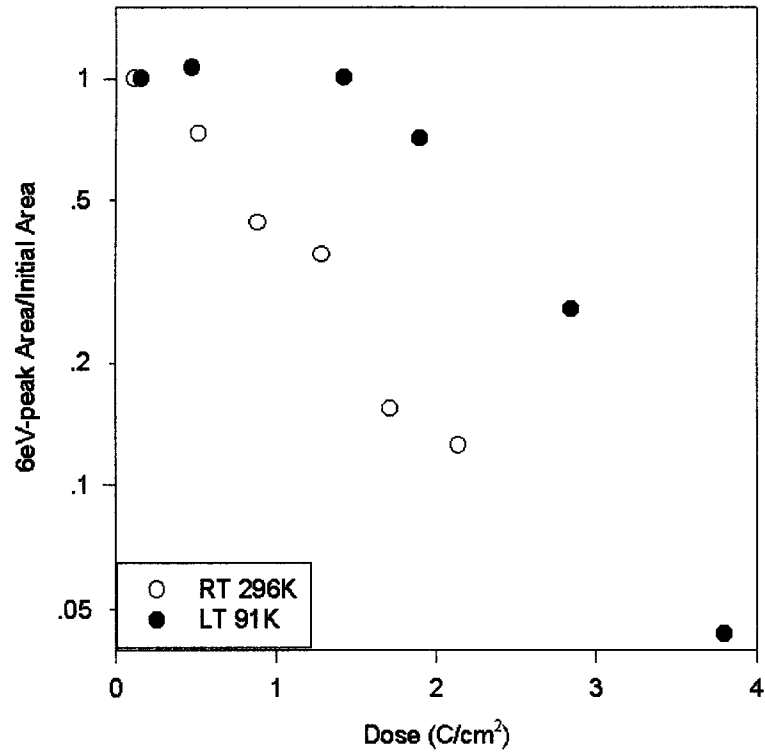


Figure 2-19: Temperature dependence of damage rate for coronene by 6eV-peak fading.  $E_0=200\text{keV}$ .

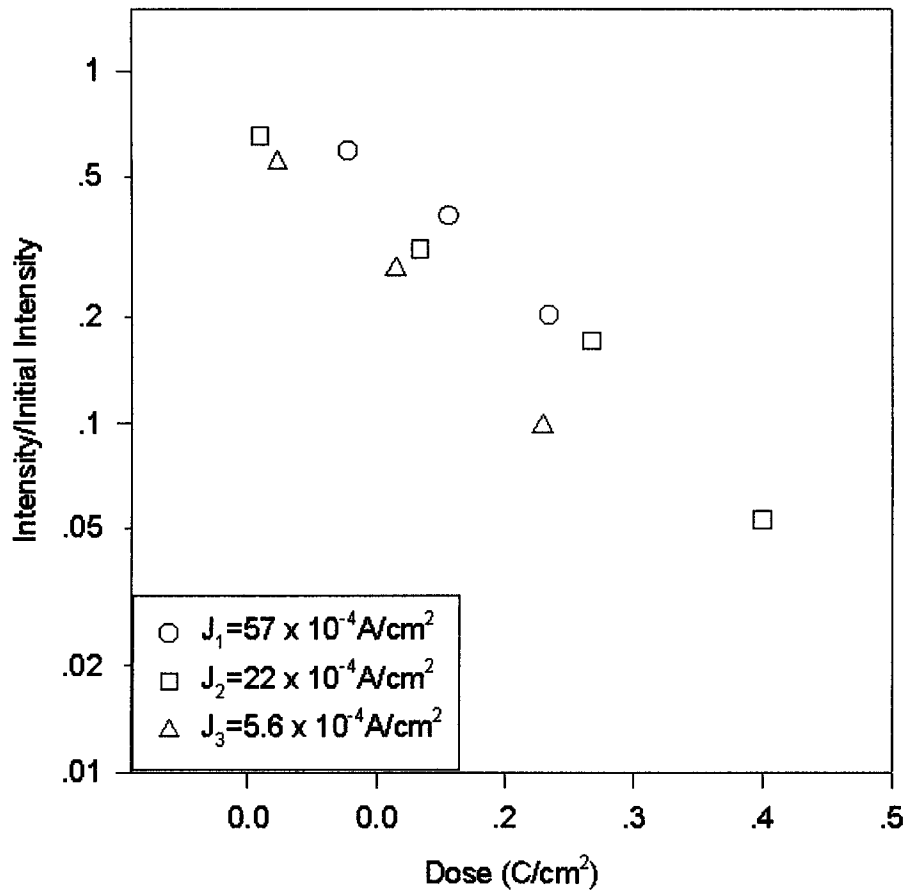


Figure 2-20: Dose rate independence of damage rate for coronene by diffraction-pattern fading,  $E_0=200\text{keV}$ .

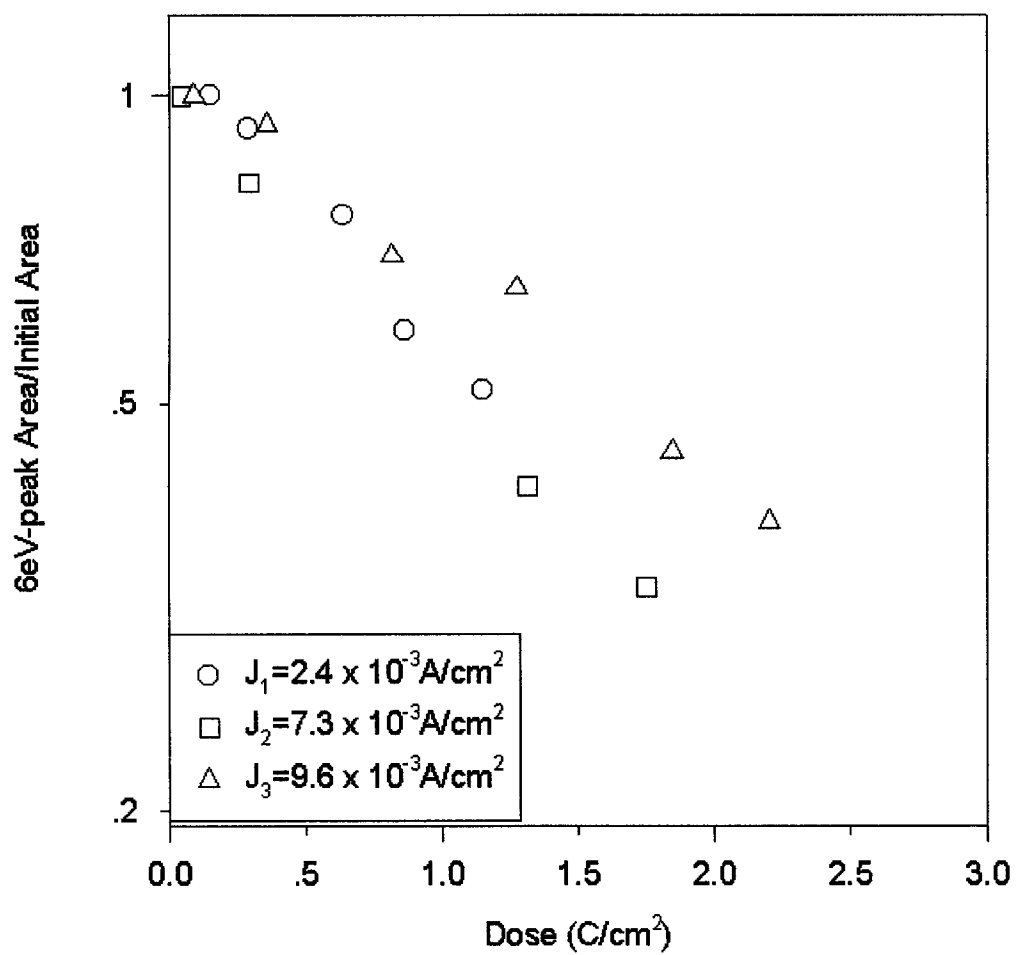


Figure 2-21: Dose rate independence of damage rate for coronene by 6eV-peak fading.  $E_0=200\text{keV}$ .

Sample: (coronene)	Thickness Monitor reading (nm)	Coverage Fraction	Local thickness by EELS ( $t/\lambda_i$ )	average thickness by EELS (nm)	EELS-average/ Monitor-reading
1	2.4	12%	$0.356 \pm 0.090$	$5.4 \pm 2.2$	$2.25 \pm 0.92$
2	3.6	16%	$0.375 \pm 0.062$	$7.4 \pm 1.9$	$2.16 \pm 0.53$
3	8.0	23%	$0.492 \pm 0.056$	$16.7 \pm 2.6$	$2.09 \pm 0.33$

Table 2-1: Thickness monitor reading and EELS thickness measurements. (the supporting carbon film  $t/\lambda_i = 0.13$ ).

	coronene	rubrene	p-terphenyl
$D_{1/e}$ (C/cm <sup>2</sup> )	1.6±0.2	1.0±0.1	1.1±0.2
$\sigma_D$ ( $\times 10^{-19}$ cm <sup>2</sup> )	1.0±0.1	1.6±0.2	1.5±0.3
Resonance Energy per $\pi$ electron* (kcal per mol)	7.5	5.5	5.4

Table 2-2: Characteristic doses for different materials by monitoring the fading of  $\pi$ -peak ( $E_0=200\text{keV}$ ). The characteristic dose  $D_{1/e}$  was measured in our JEOL 2010 TEM; the damage cross-section is  $\sigma_D=q/D_{1/e}$ , where  $q$  is the electronic charge. \* Resonance Energy per  $\pi$  electron was calculated according to Wheland (1955).

## **Chapter 3: Cathodoluminescence (CL) measurement in a scanning electron microscope (SEM)**

### ***Introduction***

A low energy electron microscope (LEEM) is considered a powerful tool for surface studies because of the small interaction depth and small lateral spread of low energy electrons. Much study has been done about electron optics and imaging for LEEM. But the radiation damage for low energy electrons is not fully understood. A threshold effect has been reported for some aromatic materials, by monitoring the decay of a diffraction pattern and noting that there is no obvious damage below a certain incident energy. Due to some unexpected problems in TEM measurement, this threshold effect needs to be confirmed further. Damage-rate measurement by monitoring the cathodoluminescence (CL) signal in a SEM has some advantages over diffraction-pattern and 6eV-peak measurements in a TEM.

A fiber/spectrometer and a PMT tube/electrometer system were added to a PHILIPS 505 SEM to measure the light-emission spectrum and the fading of the total CL emission intensity. The dependence of the damage cross-section on incident (landing) energy was measured. Measurements in the incident energy range from 1keV to 30keV were carried out with the commercial SEM's working accelerating energy. A retarding system made it possible for a

damage experiment to be conducted below 1keV landing energy. Some problems caused by the retarding system are discussed.

***Cathodoluminescence (CL) spectra measured by fiber/spectrometer system***

Cathodoluminescence spectra were measured in a PHILIPS 505 SEM working in the incident energy range of 1-30 keV. A fiber optic attached to a spectrometer was fed through the chamber to collect the emitted light (Figure 3-1). Both CL and PL emission (Figure 1-6) give a similar maximum wavelength around 505nm, which is consistent with a previous report [Mets 1975] except that their spectrum shows some fine structures -- several peaks where ours shows only one main peak. One reason may be that they measured at low temperature whereas our measurement was at room temperature. With the increase of temperature, peaks will merge.

***Total intensity measured by PMT***

The beam current in SEM will decrease dramatically with decreasing acceleration energy (Figure 3-2), which results in a reduced CL emission intensity. Due to the insufficient sensitivity, the fiber/spectrometer system was not suitable for CL measurement in the low-energy range, so a PMT/electrometer system was used (Figure 3-1). A PMT tube connected with an electrometer was attached into the SEM chamber. An aluminum funnel was mounted to the end of PMT tube to enlarge the collection solid angle. The PMT



tube was on the same side of the chamber as the secondary electron detector (SED) to reduce the possibility of the light from the SED coming into the PMT tube. To further minimize the effect of the SED during the experiment, the SED was turned off after finding an area from the secondary image. For each measurement, a background intensity was recorded after a large electron exposure, which was due to dark current of the PMT tube or maybe weak light coming from the filament and reflected by the specimen. This background was then subtracted from the recorded signal.

### ***Dependence of CL yield on incident energy***

The effect of incident energy on CL emission intensity was investigated. By keeping other illumination conditions constant, the initial CL emission intensity was recorded for different incident energies. The beam current was recorded before and after each measurement. Figure 3-3 shows the emission efficiency (total intensity/beam current) for coronene and rubrene specimens as a function of incident energy. It is expected that the emission/per electron might be proportional to the energy deposition in the film, in which case the emission-efficiency curve will follow the same trend as the calculated energy deposition. Electrons will deposit all of their incident energy into the specimen in the low-energy range, due to the fact that electron with such a low energy cannot penetrate the film. In the range of high incident energy, the energy deposited in the specimen decreases with the increasing incident energy because of the stopping power law that the energy loss per unit length is

inversely proportional to the incident energy. So there is maximum energy loss at some medium energy. But it is difficult to calculate the detailed energy deposition in the medium range where the specimen thickness is comparable to the electron range. Coronene efficiency is higher than rubrene, which can be explained from the relationship between the molecular structure and CL luminescence [Mets 1975]. The planar and rigid molecular structure of coronene results in a stronger luminescence than for rubrene.

### ***Decay of the total intensity***

It was observed in our experiments that the total intensity of light emission decreases during continuous electron exposure. Decay of the CL emission has been reported in many organic materials [Mets and Lagasse 1971, Mets 1974]. The decay mechanism, however, is not understood clearly and no quantitative measurement has been reported. Like the damage-rate measurements by diffraction-pattern and 6eV peak fading, decay of CL signal is indicative of irradiation damage by electrons.

Damage rate measurements by monitoring diffraction or 6eV energy loss peak in TEM have several limitations. The diffraction pattern method can only test specimen crystallinity [Cosslett 1978; Reimer 1984]. Furthermore, a TEM works only at high incident energy, 200keV for our TEM for example. To study the radiation damage as a function of incident energy by diffraction or 6eV energy loss peak, pre-irradiation in a low-energy e-beam instrument such as low-

energy SEM needs to be involved before examination in TEM [Howie 1985; Stevens 2000] which may introduce some unexpected problems. The film thickness must be less than the electron range at low incident energy so that the low-energy electron beam can penetrate the film and no layer is left un-irradiated. In this context, damage-rate measurement by CL emission has the following advantages: (1) both crystalline and amorphous specimens can be tested, as long as sample materials luminesce, (2) the damage measurement can be done during (not after) the electron irradiation, and (3) there is no need to consider the thickness/range problem, because the CL emission comes from the same thickness of specimen (below the surface) as that which the electrons penetrate.

### ***Characteristic dose and damage cross-section***

As defined in diffraction and 6eV methods in Chapter 2, a characteristic dose  $D_{1/e}$  is defined as the dose at which the signal decreases to a factor  $1/e$  of its initial value. The CL intensity was recorded at regular time intervals by the PMT/Electrometer system. The beam current was measured by a Faraday cup located in the center of the SEM specimen stub. The dose rate is equal to the beam current divided by the illuminated area, which can be estimated from the SEM screen. The CL intensity can be plotted on a logarithmic scale against exposure dose. Figure 3-4 shows the decay of CL intensity with the increase of exposure dose from a coronene sample at 1keV and the resulting plot is approximately linear. The characteristic dose can be obtained from the downward slope of this

intensity-dose curve. The damage cross-section  $\sigma_D$  is a direct measure of the sensitivity of the material to the damage:  $\sigma_D = q/D_{1/e}$  where  $q$  is the electronic charge.

Due to the scanning status of the electron beam in the SEM, and to the beam current applied during the measurement, some problems such as undersampling and beam heating need to be considered.

#### *Problem of undersampling*

Experimentally, the emission intensity was recorded at regular intervals during irradiation, allowing the intensity as a function of electron dose to be plotted. Electron dose rate is equal to beam current divided by the irradiated area: beam current can be correctly measured by a Faraday Cup, and the area illuminated by electron beam was estimated from SEM display screen. But for low line/frame number  $N$  and small spot size  $d$  in the SEM, undersampling could happen at low magnification (Figure 3-5): the actual area  $A_s$  illuminated by electron beam is less than the area  $A_d$  estimated from the display screen.

If undersampling happens and the characteristic dose is calculated from  $A_d$ , the area will be overestimated and the characteristic dose will be underestimated by a factor of  $n = A_d/A_s = W_d \times L / W_s \times L$ , where  $W_d$  is the width estimated from the screen,  $W_s = d \times N$  is the area scanned by the electron beam ( $d$  the spot size and  $N$  the number of lines the electron beam scanned per frame),  $L$  the length of the scanned area. For a certain spot-size, there is a critical

magnification  $M_c$ . For the magnification lower than  $M_c$ , the undersampling would happen.

The biggest spot size in our SEM is  $0.5\mu\text{m}$ , and with TV mode the beam is scanning 525 lines/frame. So considering no beam drift during the scanning, the width of actual scanned area  $W_s$  in TV mode is  $W_s = 0.5\mu\text{m} \times 525 = 263\mu\text{m} = 0.026\text{ cm}$ . It requires a magnification higher than X450 to amplify  $W_s$  to the SEM screen width of 12cm. For magnification lower than X450, the electron beam will leave un-irradiated gaps between the scan lines, and the area estimated from SEM display screen will be overestimated by a factor of  $n = W_d/W_s$ , and the characteristic dose will be underestimated by the factor of  $n$ . But for magnification comparable to or higher than X450, the area measured from SEM screen will be equal to the actual scanned area, and then the beam density won't be underestimated.

Characteristic doses were measured for several different magnifications. The sample was a 50nm (thickness monitor) coronene film on an Al foil. The incident beam energy was 6keV. Results are shown in the Table 3-1. For the magnification of X625 and X450, the area estimated from SEM screen should be equal to the area that the beam scanned, and the characteristic dose remains almost independent of magnification. The characteristic doses for magnifications lower than X450 become smaller. The ratios of characteristic dose in the magnification of X450 over those in X156 and X312 are  $D_{1/e}(450)/D_{1/e}(156) = 2.6$  and  $D_{1/e}(450)/D_{1/e}(312) = 1.8$ , which moderately agree with the ratios of  $W_d/W_s$ , which are 2.9 and

1.5 respectively. The discrepancy might be due to drift of the beam relative to the sample.

Measurements of characteristic dose for different magnifications show that undersampling happens at low magnification. To avoid this, measurements must be done at a magnification high enough to make sure that the area estimated from SEM screen is equal to the area that beam actually scans, for a certain spot-size.

#### *Problem of beam heating*

Due to the low melting point and poor thermal conductivity of organic materials, the heating effect of the electron beam should be considered during damage measurement, since we do not wish to study damage caused by heating rather than ionization. The typical melting point for organic materials is around a few hundred degrees: 428<sup>o</sup>C for coronene and 331<sup>o</sup>C for rubrene. We hope that the temperature is increased only within a few degrees, in which case the thermal effect does not make much contribution to the damage. Also the heating effect due to different dose rates in TEM measurement needs to be understood, as mentioned in Chapter 2. By considering the heat balance, the temperature increase during the irradiation can be estimated. The heat balance will be considered separately for two different specimen conditions: supported and unsupported.

##### *1. Unsupported sample:*

In the case of samples on TEM grids (Figure 3-6), because there is nothing beneath the sample (except a thin carbon supporting film)

the heat generated in the specimen by the electron beam will conduct over a distance  $R$  from the irradiated area to grid bars whose temperature  $T_0$  is the same as the surroundings. Neglecting energy carried away as kinetic energy of secondary electrons, which is believed to be a good approximation [Kohl 1981], the heat generated per second is  $Q = N\langle E \rangle'$  where  $N$  is the number of electrons arriving per second and  $\langle E \rangle'$  (in J) is the energy loss averaged over all electrons, including those which lose no energy.

If  $\langle E \rangle$  represents the average energy loss in units of eV,  $Q = N\langle E \rangle' = I\langle E \rangle$ , where  $I$  is the beam current (in A). The heat balance is represented [Egerton 1999] by:

$$J \langle E \rangle = [16(T - T_0)\kappa / d^2][0.577 + 2\ln(2R/d)]^{-1} + 2\varepsilon\sigma(T^4 - T_0^4) \quad (1)$$

where  $J$  is the beam current density,  $T$  is the temperature of the irradiated area,  $\kappa$  the thermal conductivity of the specimen,  $t$  the thickness,  $d$  the diameter of irradiated area,  $R$  the distance from irradiated area to grid bars,  $\varepsilon$  the emissivity and  $\sigma$  is the Stefan-Boltzmann constant.  $T_0 = 300\text{K}$  for room temperature and  $\varepsilon = 0.5$  (an estimate, but its value has little influence under typical conditions). Table 3-2 shows  $\kappa$  values for some solid and liquid polycarbonates [Herbert 1989]. They do not vary very much, so we take  $\kappa = 0.19 \text{ Wm}^{-1}\text{K}^{-1}$  for coronene samples. Then the temperature increase  $(T - T_0)$  during the measurement can be estimated by solving equation (1) for different parameters in SEM and TEM experiments.

### *TEM measurement*

In 200kV TEM measurement,  $d$  can be estimated from the phosphor screen calibrated by the magnification ( $2.5\mu\text{m}$  for typical TEM measurement). Other typical parameters are:  $R = 30\mu\text{m}$  (for an irradiated area in the center of a 400-mesh grid square). If inelastic scattering can be viewed in terms of collisions which are independent events, their occurrence should obey Poisson statistics and the average energy loss  $\langle E \rangle$  of electrons after passing through a film:

$$\langle E \rangle = e^{-t/\lambda} \left[ 0 + E_p \frac{t}{\lambda} + (2E_p) \left(\frac{t}{\lambda}\right)^2 \frac{1}{2!} + \dots + (nE_p) \left(\frac{t}{\lambda}\right)^n \frac{1}{n!} + \dots \right] \quad (2)$$

where  $E_p \sim 40\text{eV}$  [Egerton 1999] is the mean energy loss of an inelastically scattered electron,  $\lambda_i$  the mean free path for inelastic scattering and  $t$  the thickness. By writing the exponential term as a Taylor series and simplifying equation (2), we have

$$\langle E \rangle = E_p \frac{t}{\lambda_i} \quad (3)$$

So  $\langle E \rangle$  can be estimated from equation (3). Figure 3-7 shows the calculated temperature increase by equation (1) for an unsupported 40nm-thick coronene film during the damage measurement in TEM ( $E_0=200\text{keV}$ ; beam diameter:  $2.5\mu\text{m}$ ). It can be seen that the temperature increase is less than 1 K in the beam current range between 0.5nA and 1.5nA, in which range the characteristic dose  $D_{1/e}$  of diffraction fading and 6-eV peak was measured. So the heating effect can be safely neglected in the case of TEM



measurement. This insignificant temperature increase also explains the dose-rate independence of damage rate noted earlier.

#### *SEM measurement*

In the low-energy range, it is difficult to estimate the inelastic scattering mean free path  $\lambda_i$  in organic materials. But it is around a few nm for 1keV electrons [Seah and Dench, 1979] and decreases with decrease of the incident energy down to 100eV, which is less than the energy used in these experiments. First the electron beam in SEM is considered to be stationary instead of scanned. Due to the small penetration depth of low-energy electrons, the energy deposited in the sample for low incident energy is estimated in a different way: (1) for low  $E_0$  (electrons cannot penetrate the sample),  $\langle E \rangle = E_0$ ; (2) for higher  $E_0$ , plural scattering and slowing down of the electron is considered.  $\langle E \rangle$  can be obtained from a stopping power law [Reimer 1985]:

$$\left| \frac{dE}{dx} \right| = 7.8 \times 10^{10} \frac{Z}{A} \frac{1}{E} \ln(1.166 \frac{E}{J}) \quad (4)$$

where  $-dE$  is the mean energy loss,  $dx = \rho dt$  is a mass-thickness element,  $Z$  the atomic number,  $A$  the atomic weight,  $E$  the incident energy.  $J$  is the mean ionization potential and can be described by the formula:

$$J = 9.76Z + 58.8Z^{-0.19} \quad (5)$$

For a compound material, average  $Z$  and  $A$  are calculated using the weight fractions ( $w_i$ ) of each element:

$$Z = w_1 Z_1 + w_2 Z_2 + \dots + w_3 Z_3 \quad (6)$$

$$A = w_1 A_1 + w_2 A_2 + \dots + w_3 A_3$$

The decrease of the electron energy  $E(t)$  with increasing thickness  $t$  can be obtained by numerical integration of equation (4):

$$t = \int_{E_t}^{E_0} \left( \frac{1}{-\left(\frac{dE}{dt}\right)} \right) dE \quad (7)$$

where  $E_0$  is the incident energy and  $E_t$  the final energy of electrons after passing through a film with a thickness  $t$ . For a given thickness  $t=40\text{nm}$  and incident energy  $E_0$ , the energy  $E_t$  after electrons exit the film can be calculated from equation (7). Then, the energy deposited in the film is  $\Delta E=E_0-E_t$ . In the case that a low-energy electron is not transmitted through the film (electron range  $R<t$ ), all its energy will deposit in the specimen. Figure 3-8 shows the calculated deposited energy in a 40nm thick coronene specimen for electrons with different incident energies. Electrons will deposit all of their incident energy into the specimen in the low-energy range due to the fact that electron with such a low energy can not penetrate a 40nm thick coronene film. In the range of  $E_0>2\text{keV}$ , the energy deposited in the specimen is decreasing with the increasing incident energy because of the stopping power law that the energy loss per unit length is inversely proportional to the incident energy. So there is maximum energy loss at some medium energy. But it is difficult to calculate the details in the medium range.

Figure 3-9 shows the calculated temperature increase by equation (1) for an unsupported 40nm-thick coronene film for a stationary 0.7keV electron beam. Even in a low beam current as low as 1nA, the temperature can be increased by a few tens of degrees while it reaches 300 degrees for 8nA beam. But this result is obtained without considering any scanning of the beam. The beam is not focused onto an area all the time during the irradiation, so the time dependence of heat dissipation has to be considered.

At the SEM video-rate full-frame display, the scanning condition is 525 lines, 60 frames/sec. Then the time T for scanning a single line is  $3.2 \times 10^{-5}$  sec. At the magnification  $\times 450$  the length L of the illuminated area is 0.026cm. Then with the scanning rate  $v=L/T$  and the spot size  $d=0.5\mu\text{m}$ , the time  $\Delta t$  during which the electron beam scanned a single pixel with a diameter d is

$$\Delta t = \frac{d}{v} = \frac{d}{L} T = 6.2 \times 10^{-8} \text{ sec} \quad (8)$$

It takes a time  $\tau$  for the illuminated area to reach the heat balance. If the scan time between pixels  $\Delta t$  is much smaller than  $\tau$ , heat balance is not reached after  $\Delta t$  and the temperature increase will be less than for a stationary beam. To estimate an upper limit, we assume that during the scanned time  $\Delta t$  no heat dissipates and all deposited energy contributes to heating the specimen within the small volume that the electron beam penetrates, in which case the temperature increase  $\Delta T$  can be calculated from:

$$p\tau = mC_v\Delta T \quad (9)$$

where  $p=I\langle E \rangle$  is the energy deposited per second,  $m$  is the mass of the material within a volume  $v=\pi d^2t/4$  ( $d$ : the beam diameter;  $t$ : the specimen thickness) and  $C_v$  is the heat capacity of specimen. The result obtained is that after  $\Delta t$ , the temperature increase ( $T_s-T_0$ ) does not reach the value when the heat balance is obtained. Figure 3-10 shows the temperature increase for both stationary and scanned beams with 8nA current. After the scan time  $\Delta t$  for a single pixel, the temperature increase is about tens of degrees for a 40nm thick coronene specimen with 700eV electrons of 8nA beam current. If the dissipation time is long compared to the scanning time, the temperature increase could be somewhere between the stationary and the scanned beam, which could be from tens degrees to a few hundred degrees. As discussed in chapter 2, under the same illumination condition the specimen undergoes severe problems of heating and contamination, which make the measurement misleading. In the range between 10 and 30keV, the temperature increase is below 5 degrees, in which case the heating effect is insignificant.

## 2. Supported sample:

For a sample on Al foil or Au foil (Figure 3-11), the heat balance is totally different from that of an unsupported film. The Al foil used as the substrate is around 20 $\mu$ m thick, which is much thicker than the specimen (40nm). Since the electron range is less than 10 $\mu$ m for an electron with the energy less than 30keV, heat is generated in the

substrate but can quickly conduct through the metal substrate foil. The substrate is in thermal contact with the SEM stub whose temperature is  $T_0$ . Then we can consider that the heat is generated in an area  $A$  within a small depth below the upper surface of the foil, where the temperature is  $T$ . To obtain an upper estimate if the temperature rises, we assume that the heat will travel down within a cylinder with a cross-section area of  $A$  to the lower surface whose temperature  $T_0$  is the same as the surroundings (Figure 3-12). In this simplification, we overestimate  $T$ , because in practice the heat will travel in an angular cone (Figure 3-12a) down to the stub instead of being limited to the cylinder (Figure 3-12b).

Again neglecting the energy carried away by secondary electrons, the heat generated per second by the incident electron beam is  $Q = NE'_0$ , where  $N$  is the number of electrons per second,  $E'_0$  (in J) is the incident energy.  $Q$  is therefore equal to  $IE_0$ , where  $I$  is the beam current,  $E_0$  is in eV and the heat balance can be written as:

$$IE_0 = \kappa S(T - T_0)/t_{AL} \quad (10)$$

Here  $\kappa = 237\text{Wm}^{-1}\text{K}^{-1}$  is the thermal conductivity of Al,  $S$  is the area irradiated by the electron beam and  $t_{AL}$  the thickness of Al foil.

Figure 3-13 shows the calculated temperature increase in the low - energy range for an 8nA beam. In the low-energy range, the temperature increase is always below 2 degrees. Substituting  $\tau$  by  $\Delta t$  in equation (9), after the scanned time  $\Delta t = 6.2 \times 10^{-8}$  sec, the

temperature increase has exceeded the temperature at which the heat balance is reached, which means that the beam can be considered as stationary. Figure 3-14 shows the calculated temperature increase versus the incident energy for a stationary 8nA beam illuminating an Al-foil supported coronene film (40nm). In the low energy range 0.1-10keV, the temperature increase is less than 5degrees. But for higher energy 10-30keV, the temperature increase could reach as high as tens of degrees, which would cause some heating problems.

In summary, we can draw the following conclusions according to the beam heating in our experiments:

- (1) For all irradiation conditions in TEM measurements, the temperature increase was less than 1K, so the heating effect can be neglected.
- (2) In SEM measurement or pre-irradiation, the temperature increase might reach a few tens of degrees in some conditions, which will effect the damage measurements. To keep the thermal effect insignificant, an unsupported sample should be used in high-energy range (10-30keV) and a metal film substrate is needed as a heat sink when irradiated in the energy range 0.1-10keV.

## ***Damage cross-section versus incident energy***

### *Retarding system*

To verify the threshold effect reported by previous researchers, the damage cross-section of a coronene specimen was measured as a function of the incident energy by the CL-fading method. In principle, two alternative forms of the low-voltage electron system are possible: either the whole SEM column is optimized to a low energy, or the classical SEM with electrons accelerated to a certain energy is equipped with retarding field optics, decelerating the electrons immediately in front of the specimen and accelerating again the emitted electrons [Mullerova and Frank 1993, Paden and Nixon 1968]. The lowest accelerating voltage  $U_a$  in our SEM is 1kV, but by applying a negative potential  $U_r$  to the stage, characteristic dose can be measured for a landing energy as low as  $(U_a - U_r)$ , when the SEM works with an accelerating energy  $U_a$ . Besides varying the range of landing energy, another advantage of this retarding system is that it can increase the beam current for the same incident/landing energy. Without a retarding potential, the beam current decreases dramatically with decrease of accelerating voltage (Figure 3-2). By adjusting the distance between the filament tip and the Wehnelt and the resistance  $R_w$  in the connection line of the high-tension supply to the cathode, maximum beam current can be obtained at a given accelerating voltage. For example, at an incident energy of 3keV, the beam current can reach as high as  $5 \times 10^{-8} \text{A}$ , but for 1keV the beam current is only  $2 \times 10^{-9} \text{A}$ . An even smaller value would be expected at

an energy of 500eV. With such a low value of beam current, the sample might not give out enough signal for the detector. By applying a -500V potential on the stage, the beam current should stay around  $2 \times 10^{-9} \text{A}$ , because there is no obvious reason that applying a retarding potential would affect the beam current.

*Surface effect and landing energy calibration by reflection*

Reducing the energy of the electrons incident on a solid has a profound effect on the interactions that occur within that material. Electrons in the energy range between about 100eV and a few keV interact much more strongly with the material through which they are traveling than is the case at higher energies. The first consequence of this is that the distance which the electron will penetrate will fall rapidly as the incident energy is reduced. This means that, while scanning microscopy at high energy (20-30keV) can observe the bulk of a specimen, operation at low beam voltages restricts the interaction to the near-surface regions of the material. All of the signal in the low voltage image will come from that portion of the sample which lies close to the entrance surface of the electron beam, even for very thin specimens [Joy 1996]. Figure 3-15 shows secondary electron (SE) images of a 20nm thick carbon film stretched over a copper mesh grid at different incident energies. In Figure 3-15a, the film is almost invisible because the majority of the incident electrons traverse the carbon without producing any interaction. But at 1keV (Figure 3-15b), all of the electron interaction volume is contained within the thickness of the carbon, and the resultant SE emission from the film make it appear solid and opaque.



In case the accelerating voltage meter does not read the voltage accurately, the landing energy needs to be calibrated before any measurement when a retarding potential is applied. An inaccurate reading may cause a negligible discrepancy in the high-energy range but a 30-volt mis-reading can result in a 30-10% discrepancy if operating in the energy range between 100-300eV. Reflection of the incident beam [Mullerova and Frank 1993] was used to calibrate the landing energy of the electron beam. Figure 3-16 shows a diagram of electrons traveling in the SEM column. Electrons emitted from the filament are accelerated to a certain velocity  $V_0$  after passing through the anode. Then the electron beam is deflected by a deflection coil system to scan an area on the sample. Without any retarding potential on the stage, electrons will travel from the final aperture to the sample with their initial velocity  $V_0$ . But with a negative potential on the stage, electrons will be decelerated. When the bias potential is greater than the incident energy, all incident electrons will be reflected backward before they can reach the sample. Then an image of inside of the chamber will be observed. The point where  $U_r$  is equal to  $U_a$  (the landing energy  $U_L=U_a-U_r=0$ ) can be obtained when the reflection just starts. Figure 3-17 shows how the reflection occurs when the retarding potential is increasing close to the accelerating voltage. Images of the inside of the specimen chamber are formed after the reflection. The reflection starts at  $U_r=1.12\text{keV}$ , whereas the voltage meter of the SEM reads  $U_a=0.9\text{keV}$ , which confirms that there is a discrepancy of 220V between the SEM accelerating-voltage meter and the incident energy of the electron beam.

The fact that the vertical component of velocity of the electrons is reduced but not the horizontal component will result in some change of the area illuminated by electron beam, equivalent to a change in SEM magnification. By assuming a uniform electric field  $E = U_r/r$  between the final aperture and the stage, where  $U_r$  is the retarding potential,  $r$  is the distance between the final aperture and the stage, the relation between the change of area and applied negative potential can be estimated. Figure 3-18 is a diagram of electrons traveling from the final aperture to the stage in the SEM column with and without the retarding potential  $U_r$ . After passing the anode, electrons acquire a kinetic energy KE:

$$KE = qU_a \quad (11)$$

where  $q$  is the electronic charge,  $U_a$  is the accelerating voltage between anode and cathode. Electrons, then, have an initial velocity  $V_0$ :

$$\frac{1}{2}mV_0^2 = qU_a \quad (12)$$

where  $m$  is the mass of an electron. Considering the angle  $\alpha$  of electron beam deflected by deflection coil system, the horizontal and vertical initial velocities are

and

$$V_{ox} = V_o \sin \alpha$$

$$V_{oy} = V_o \cos \alpha \quad (13)$$

respectively. Without the retarding system, electrons will travel to the sample on the stage with constant velocity of  $V_0$ . So the horizontal coordinate

$$X = r \cdot \operatorname{tg} \alpha = r \frac{V_{ox}}{V_{oy}} \quad (14)$$

When a retarding potential  $U_r$  is applied, in the vertical direction, electrons will travel with a uniform negative acceleration:

$$a = \frac{U_r q}{mr} \quad (15)$$

Because there is no electric field between the final aperture and the SEM anode, electrons keep their constant velocity  $V_0$  until reaching the final aperture. Then the time  $t$  taken for electrons to travel from the final aperture to stage should be the root  $t_1$  with smaller value of the uniform acceleration equation:

$$V_{oy}t - \frac{1}{2}at^2 = r \quad (16)$$

then:

$$t_1 = \frac{V_{oy} - (V_{oy}^2 - 2ar)^{1/2}}{a} \quad t_2 = \frac{V_{oy} + (V_{oy}^2 - 2ar)^{1/2}}{a} \quad (17)$$

The bigger root  $t_2$  corresponds to the time taken for electrons to pass by where the specimen stage is located (if the stage doesn't exist) and travel to a distance where electrons stop, and be accelerated back to the sample stage, which will never happen in the real situation.

Then the distance electrons travel in the horizontal direction is  $X'$ :

$$\begin{aligned}
 X' &= V_{\alpha} t \\
 &= \frac{V_o \sin \alpha [V_o \cos \alpha - (V_o^2 \cos^2 \alpha - 2 \frac{U_r q}{m})^{1/2}]}{\frac{U_r q}{mr}} \\
 &= \frac{V_o^2 \sin \alpha \cos \alpha [1 - (1 - \frac{U_r}{U_a \cos^2 \alpha})^{1/2}]}{\frac{U_r q}{mr}} \quad (18)
 \end{aligned}$$

The ratio of distances that electron with incident energy  $qU_0$  and retarding potential  $qU_r$  on the stage illuminates on the sample compared to the distance without retarding potential is:

$$\begin{aligned}
 R &= \frac{X'}{X} \\
 &= 2 \frac{U_a}{U_r} \cos^2 \alpha [1 - (1 - \frac{U_r}{U_a \cos^2 \alpha})^{1/2}] \quad (19)
 \end{aligned}$$

For a small angle  $\alpha$ , we can take  $\cos \alpha \approx 1$ , so

$$\begin{aligned}
 R &= \frac{X'}{X} \\
 &\approx 2 \frac{U_a}{U_r} [1 - (1 - \frac{U_r}{U_a})^{1/2}]. \quad (20)
 \end{aligned}$$

The ratio of areas of the rastered beam will be equal to:

$$R^2 = 4 \left( \frac{U_a}{U_r} \right)^2 [1 - (1 - \frac{U_r}{U_a})^{1/2}]^2 \quad (21)$$

Figure 3-19 shows the experimental value of ratio  $R^2$  versus the retarding potential  $U_r$ , and theoretical results calculated by the equation (21) (with an accelerating energy  $U_a=1.12\text{keV}$  and a magnification of X573). The experimental points agree with the theoretical curve very well.

#### *CL damage cross-section versus incident energy*

Finally, we report the dependence of damage cross-section on the incident energy for a coronene film (Figure 3-20), as measured in our SEM. In the energy range from 1keV-30keV, damage rate measurements were done without any retarding potential, while in the energy below 1keV, measurements were conducted with a constant accelerating energy of 1.12keV and a retarding potential on the stage. The damage cross-section does decrease in the low-energy range, but there is no obvious threshold as reported by some groups [Howie 1985, Stevens 2000] for diffraction-pattern fading. Decay of the damage cross-section in the low-energy range might be due to other factors such as less energy deposited in the specimen and low secondary electron yield at lower incident energy. A more detailed discussion will be given in Chapter 4.

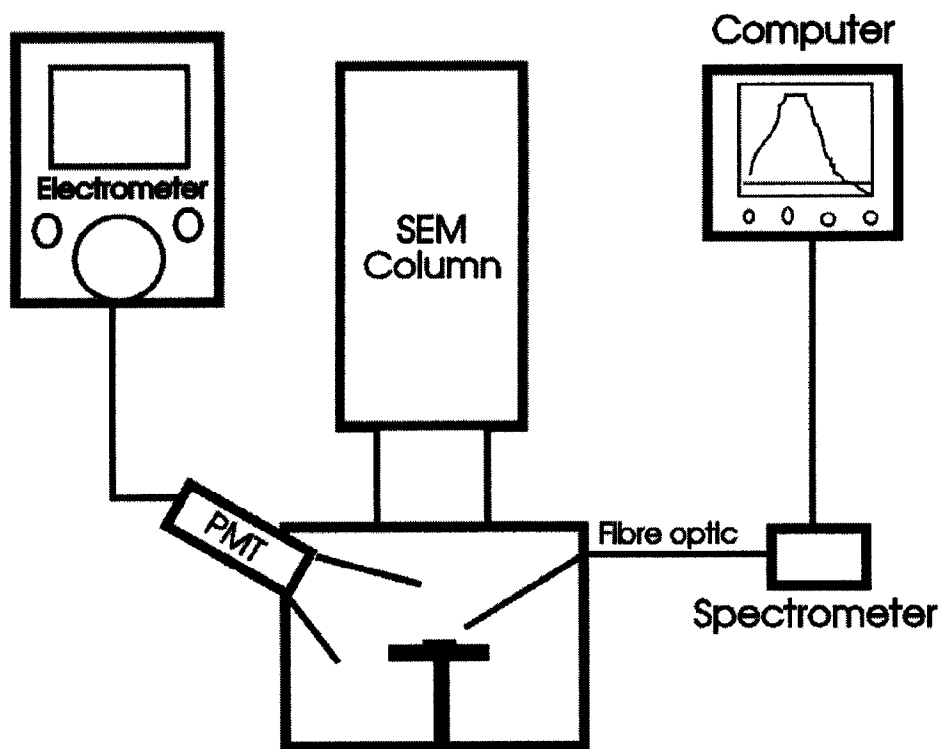


Figure 3-1: Diagram of cathodoluminescence apparatus with a SEM: A fiber optic connected to a spectrometer was fed through the SEM chamber to measure the CL emission spectrum; a PMT/electrometer system was used to measure the total emission intensity.

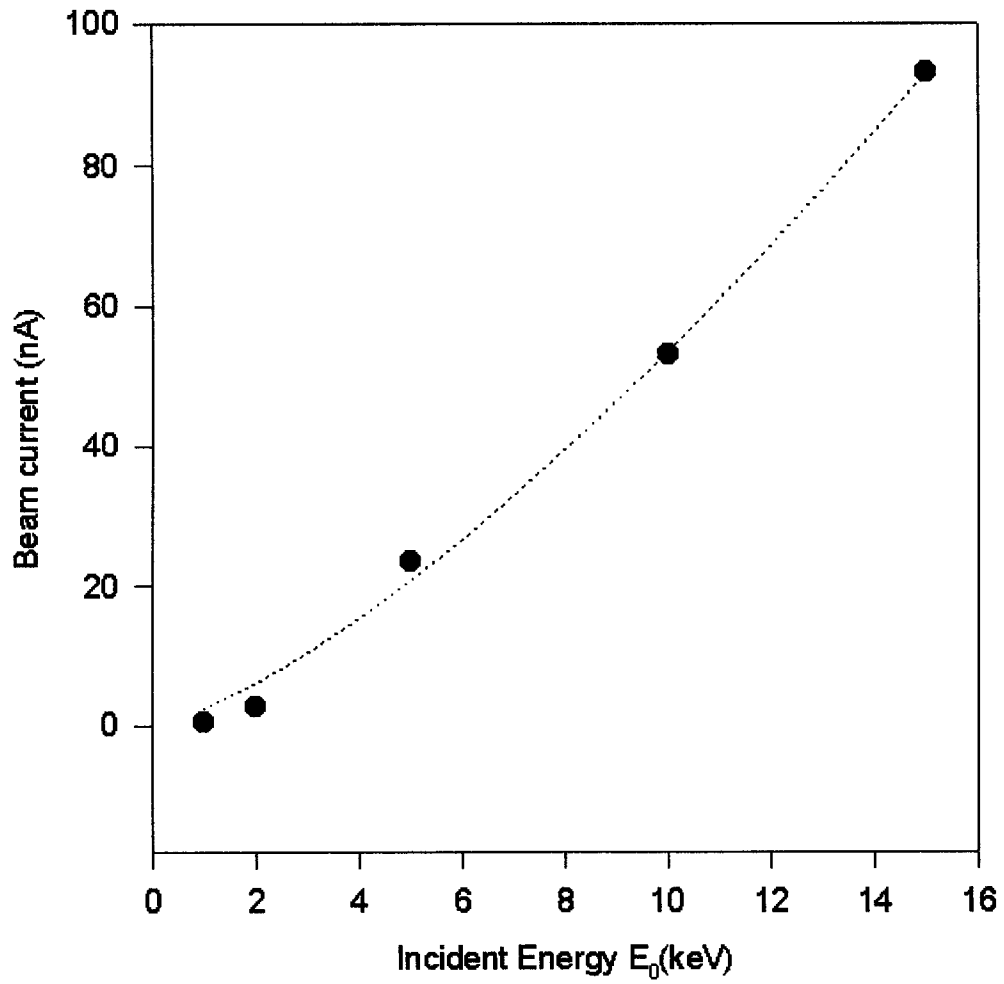


Figure 3-2: Beam current vs. incident energy in our PHILIPS 505 SEM.

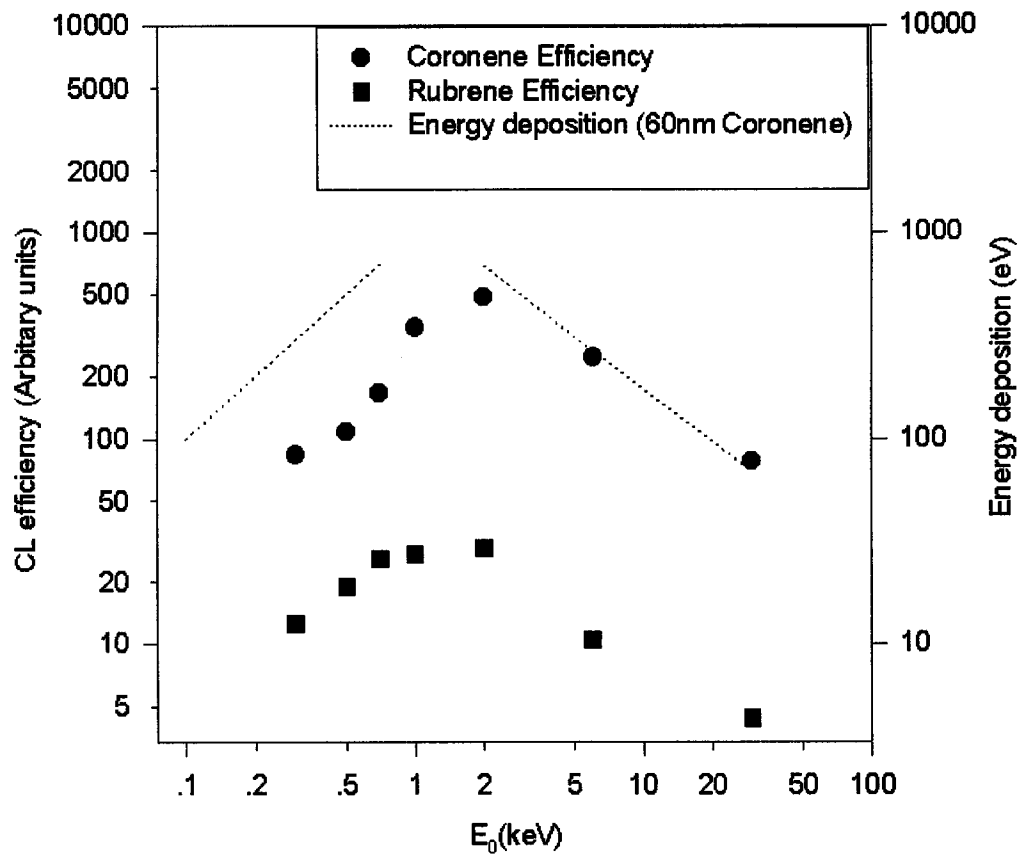


Figure 3-3: Cathodoluminescence efficiency for coronene and rubrene. The efficiency is shown (left) in terms of the intensity/beam current; energy deposition (right) was calculated for the primary beam transmitted through a 60nm thick coronene film.



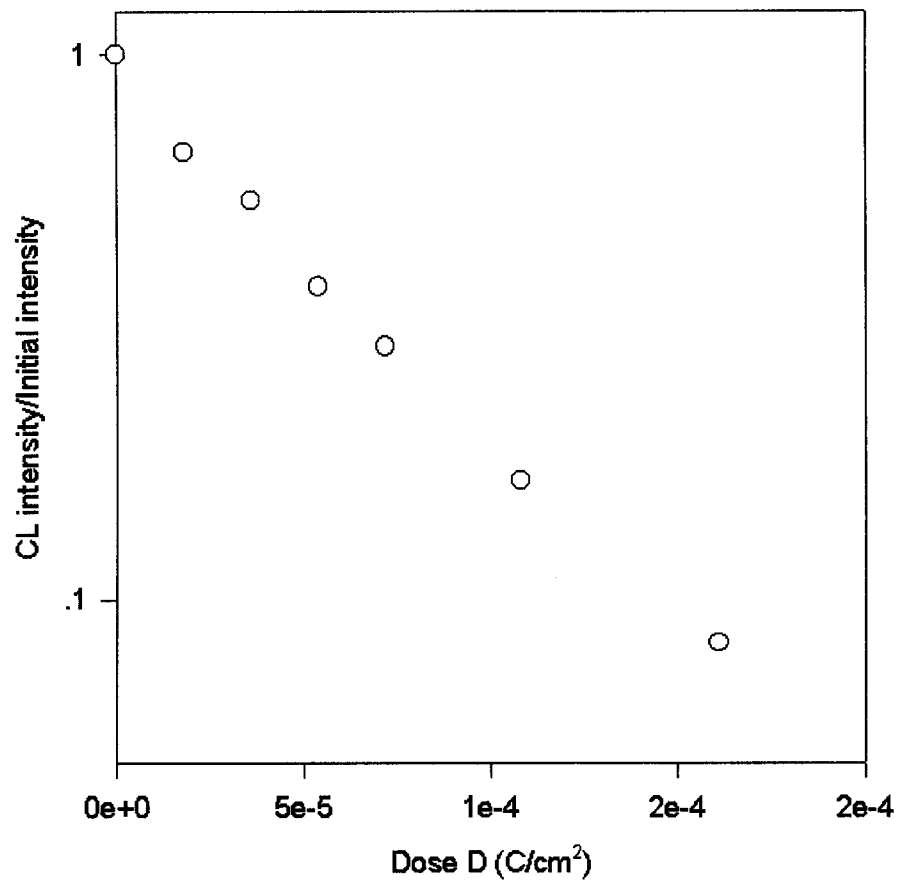


Figure 3-4: Cathodoluminescence intensity vs. dose curve. (coronene,  $E_0=1\text{keV}$ )

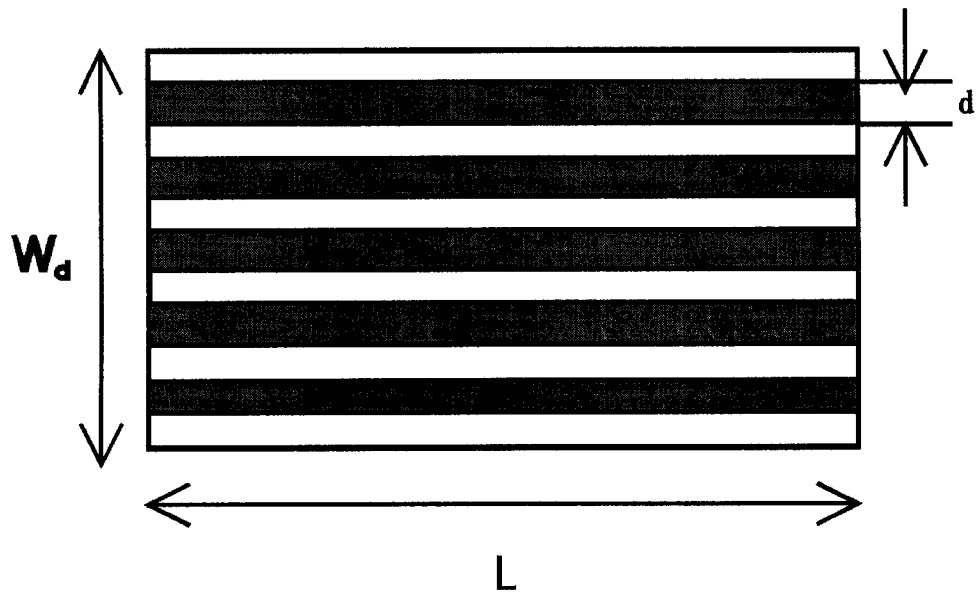


Figure 3-5: Undersampling for low magnification in the SEM. For low line/frame number  $N$  and small spot size  $d$  in the SEM, undersampling could happen at low magnifications: the actual area (gray area)  $A_s = d \times N \times L$  scanned by the electron beam is less than the area (gray + white area)  $A_d = W_d \times L$  estimated from the display screen, where  $L$  is the length of screen and  $W_d$  is the width of screen.

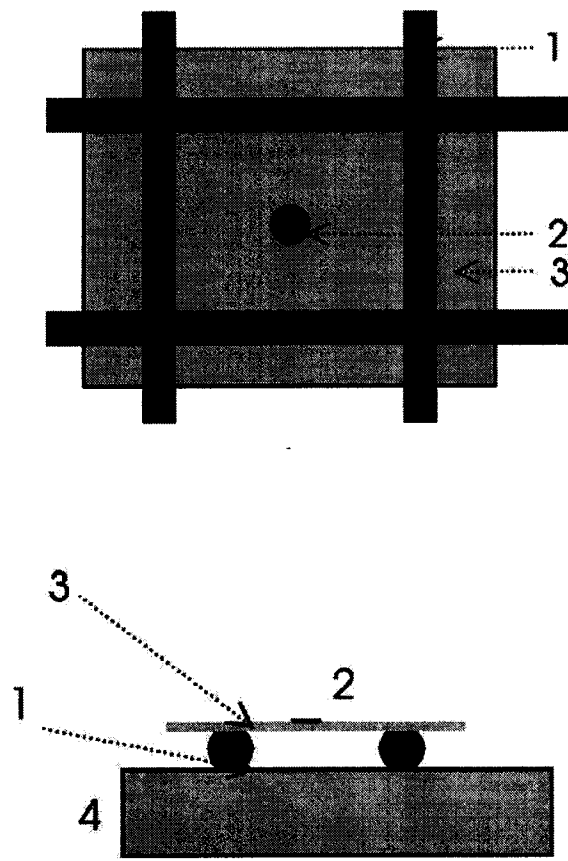


Figure 3-6: An unsupported organic specimen on a TEM grid. The heat generated in the specimen (3) by the electron beam will conduct over a distance  $R$  from the irradiated area (2) to grid bars (1) whose temperature  $T_0$  is the same as the surroundings. 1: Grid bars; 2: Area illuminated by e-beam; 3: Organic specimen; 4: SEM stub.

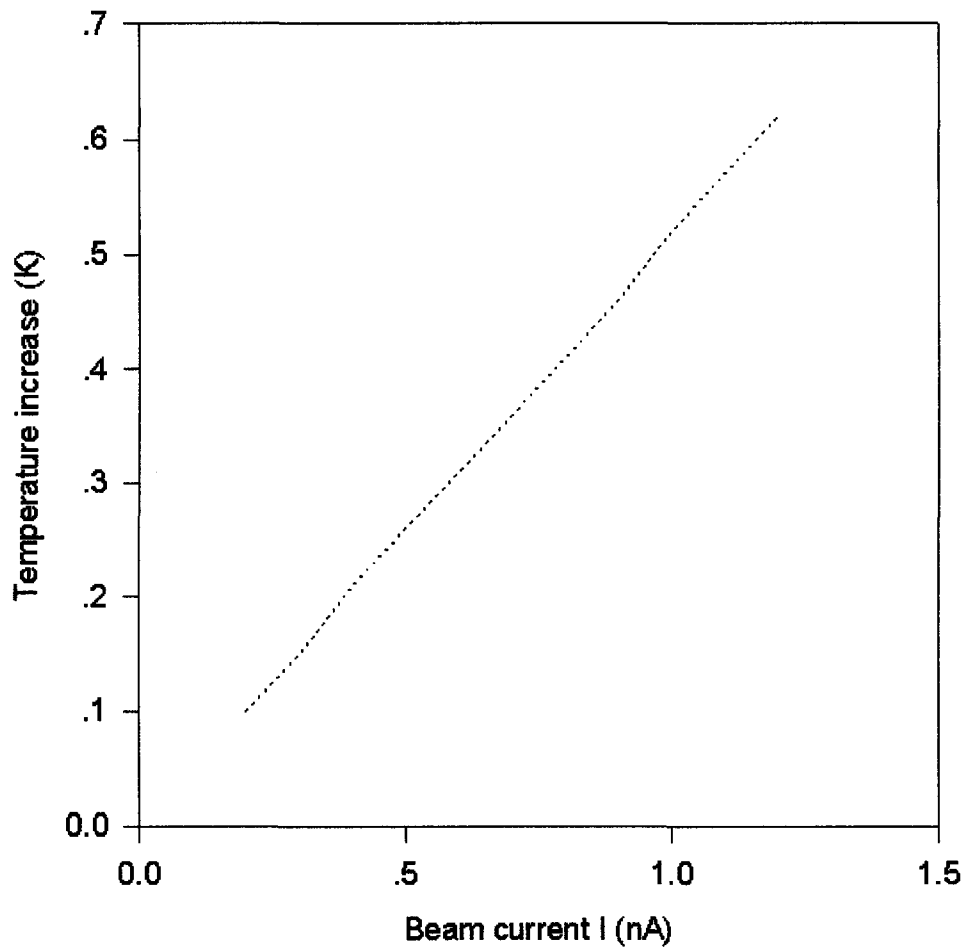


Figure 3-7: Calculated temperature increase for an unsupported 40nm thick coronene film during the damage measurement in TEM ( $E_0=200\text{keV}$ , beam diameter:  $2.5\mu\text{m}$ ).

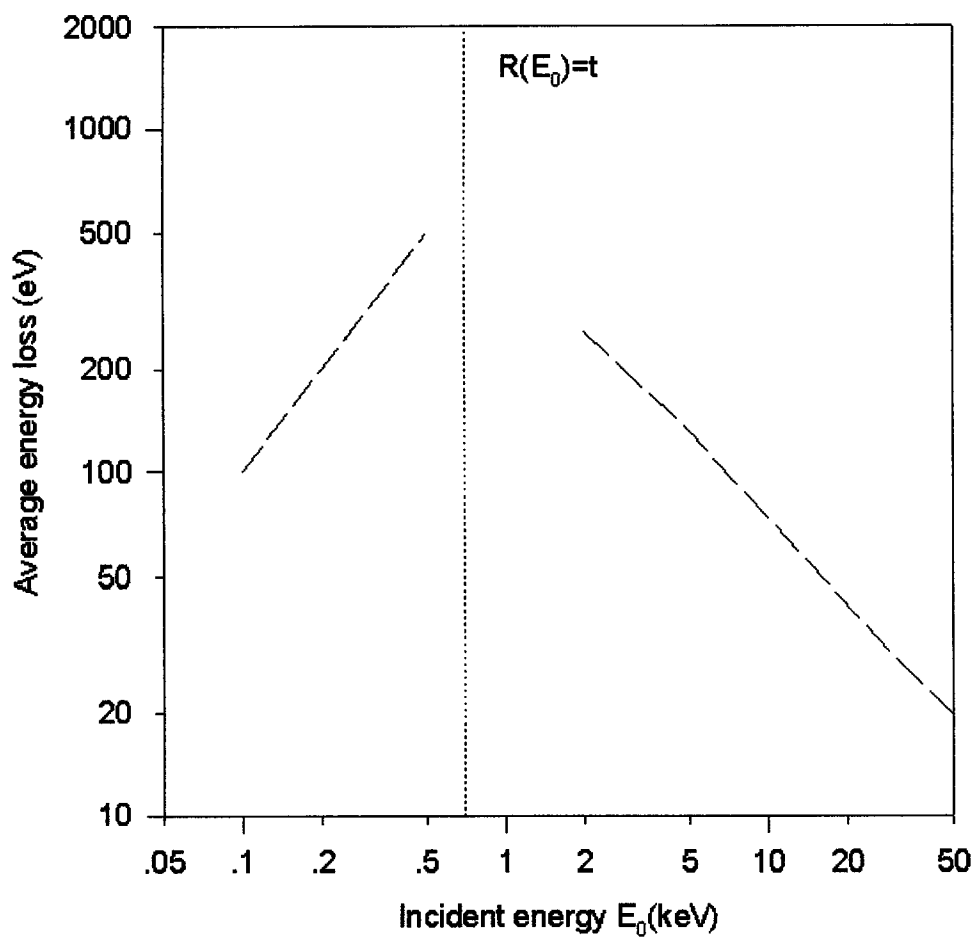


Figure 3-8: Average energy loss in a coronene film (thickness  $t=40\text{nm}$ ), calculated by Bethe Stopping Power Law. The vertical dashed line shows the incident energy where the electron range is approximately equal to the thickness  $t=40\text{nm}$ .

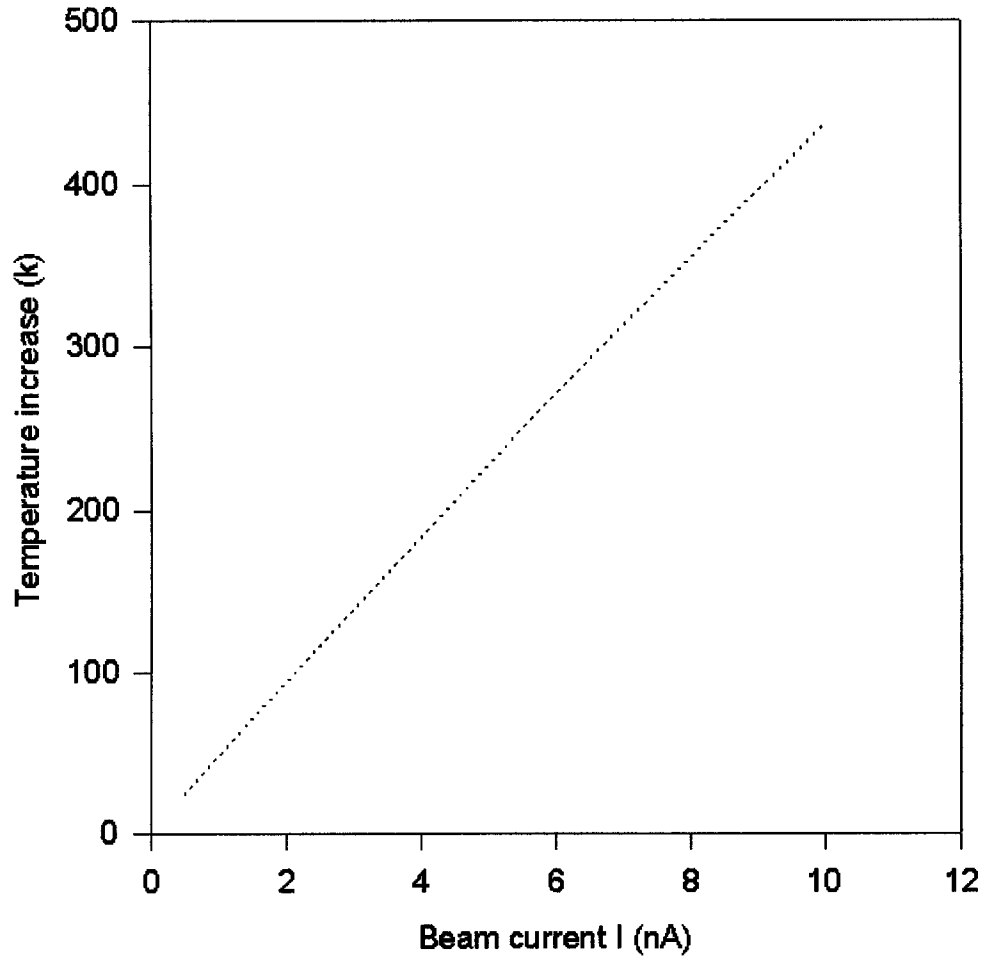


Figure 3-9: Calculated temperature increase for an unsupported 40nm thick coronene film with a stationary beam ( $E_0 = 0.7\text{keV}$ , spot size  $= 0.5\mu\text{m}$ ).

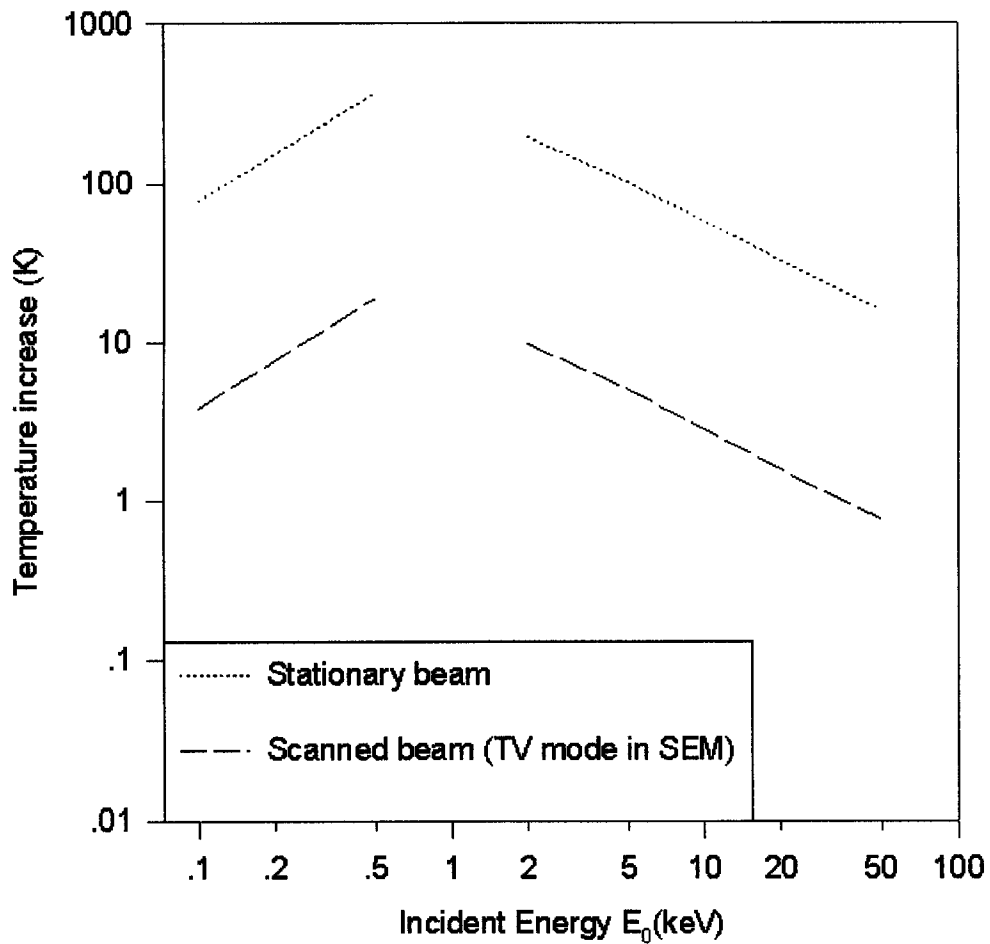


Figure 3-10: Calculated temperature increase for a stationary beam and scanned beam at the SEM video-rate full-frame display ( $I=8\text{nA}$ , spot size =  $0.5\mu\text{m}$ ). The temperature increase for a scanning beam was estimated by assuming the generated heat will be dispersed between two adjacent scans. If the dissipation time is long compared to the scanning time, the temperature increase could be somewhere between the stationary and the scanned beam case.

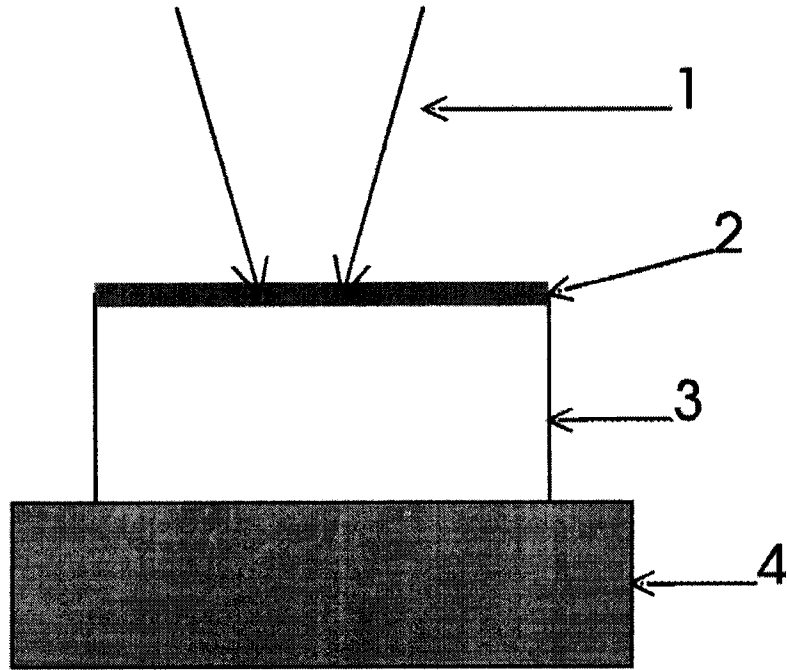
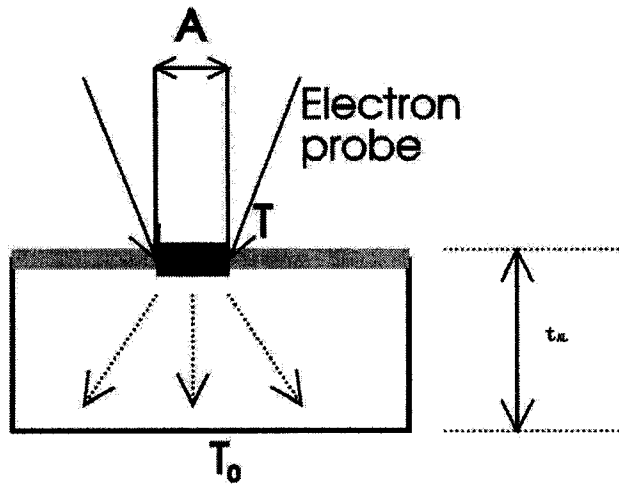
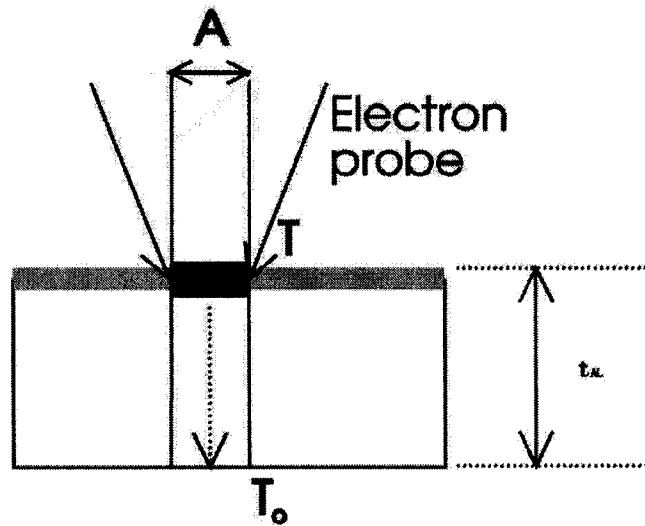


Figure 3-11: A supported organic specimen on an Al foil. The heat generated by the electron beam (1) can efficiently conduct through the metal substrate foil (3). The substrate is in thermal contact with the SEM stub (4) whose temperature is  $T_0$ . 1: Electron probe; 2: Organic specimen; 3: Al foil; 4: SEM stub.





a



b

Figure 3-12: The heat balance in a supported sample on Al foil. To obtain an upper estimate, we assume that the heat will travel down within a cylinder with a cross-section area of  $A$  to the lower surface whose temperature  $T_0$  is the same as the surroundings (b). In this simplification, we overestimate  $T$ , because in practice the heat will travel in an angular cone (a) down to the stub instead of being limited to the cylinder.

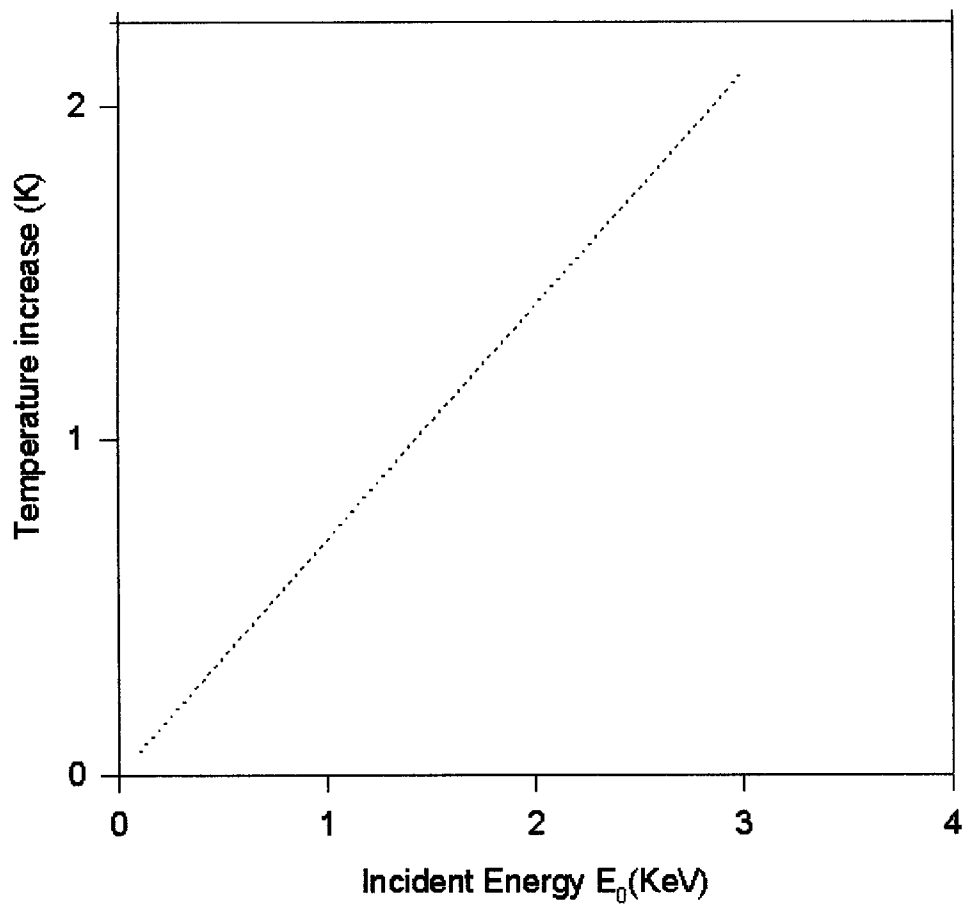


Figure 3-13: Calculated temperature increase for a thin coronene sample (40 nm) on a thick Al foil ( $\sim 20\mu\text{m}$ ) in the low-energy range. ( $I=8\text{nA}$ , spot size =  $0.5\mu\text{m}$ ).

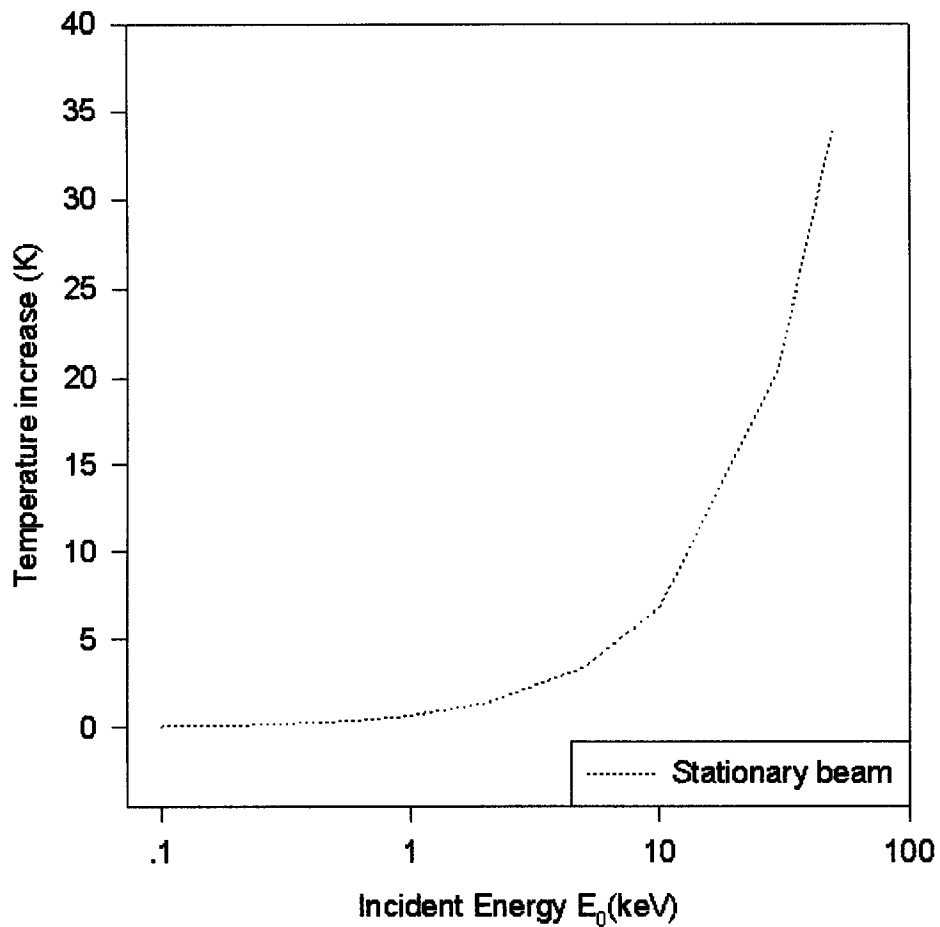
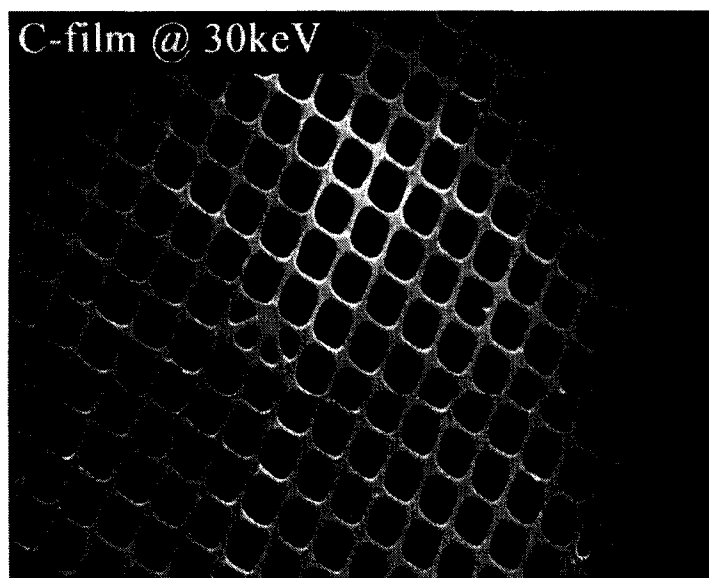
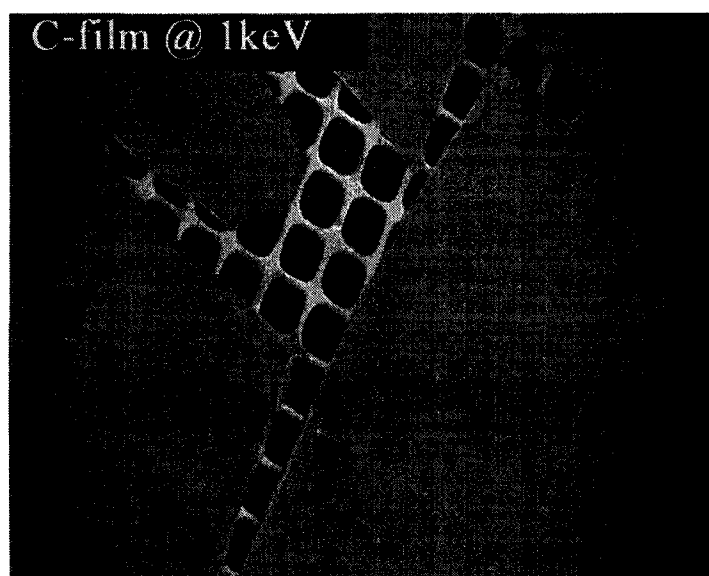


Figure 3-14: Calculated temperature increase for a stationary beam (0.1-30keV) illuminating an Al-foil supported coronene film (40nm). ( $I=8\text{nA}$ , spot size =  $0.5\mu\text{m}$ ).



a



b

Figure 3-15: SEM images of a 20nm thick carbon film on a TEM grid for different incident energies (a:30keV; b: 1keV).

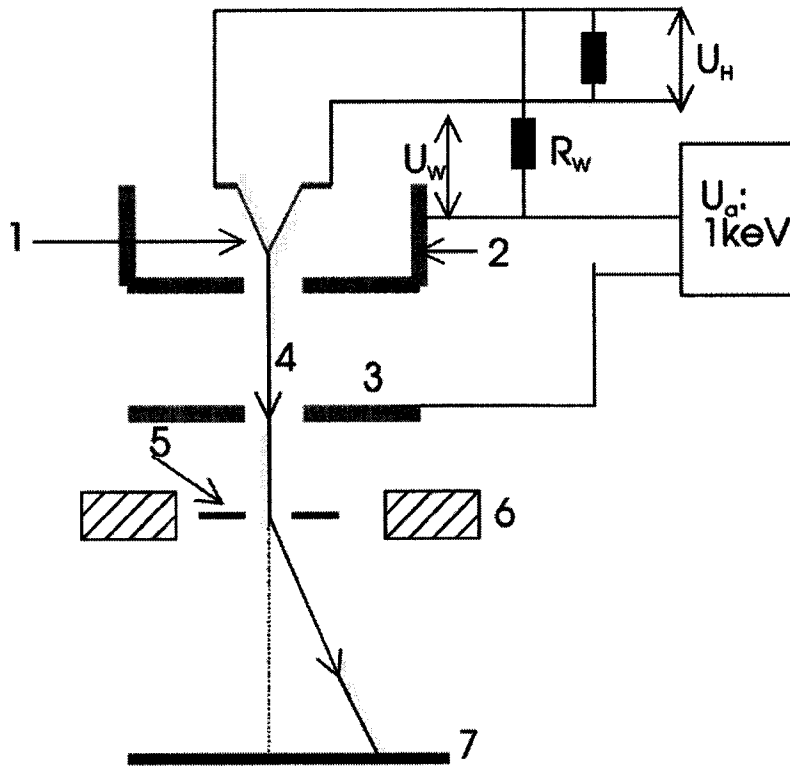
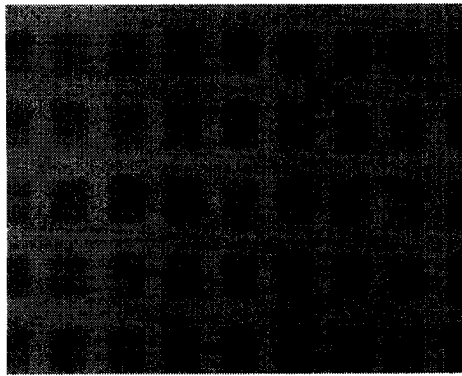
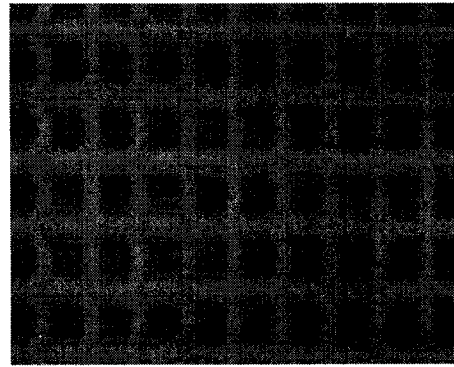


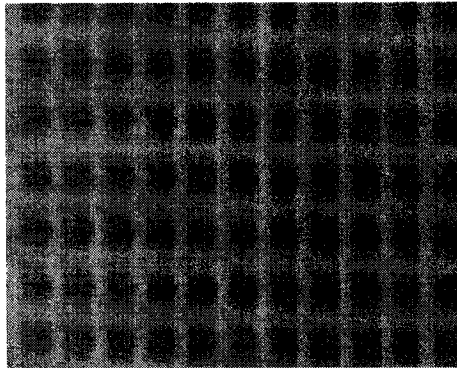
Figure 3-16: Diagram of electrons traveling in the SEM column. Electrons emitted from the filament are accelerated to a certain velocity  $V_0$  after passing through the anode (3). Then the electron beam is deflected by a deflection coil system (6) to scan an area on the sample. Without any retarding potential on the stage (7), electrons will travel from the final aperture (5) to the sample with their initial velocity  $V_0$ . But with a negative potential  $U_r$  on the stage, electrons will be decelerated and a landing energy  $U_L$  can be obtained as low as  $(U_a - U_r)$ , where  $U_a$  is the accelerating energy. 1: Cathode; 2: Wehnelt; 3: Anode; 4: Electron beam; 5: Final aperture; 6: Deflection coil system; 7: Stage.



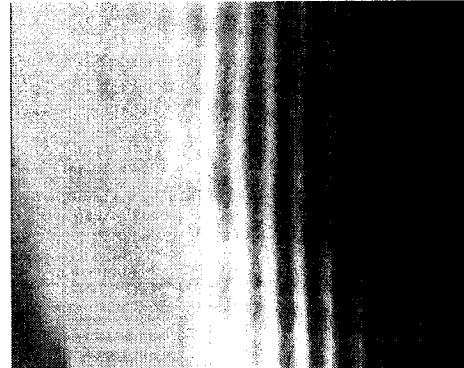
a:  $U_r=0$ ,  $U_L=1.12\text{keV}$



b:  $U_r=0.52\text{keV}$ ,  $U_L=0.6\text{keV}$



c:  $U_r=0.92\text{keV}$ ,  $U_L=0.2\text{keV}$



d:  $U_r=1.12\text{keV}$ ,  $U_L=0$



e: a hole

f: the stage

g: SED grids

Figure 3-17: Electron reflection in a SEM with a retarding system. a,b,c and d show the reflection occurs when the landing energy  $U_L$  is approaching 0 in the SEM (The accelerating energy  $U_a=1.12\text{keV}$ ; the retarding potential  $U_r$  is increasing to  $U_a$ ). e,f and g are some reflected images inside the SEM chamber when  $U_r$  is greater than  $U_a$ .

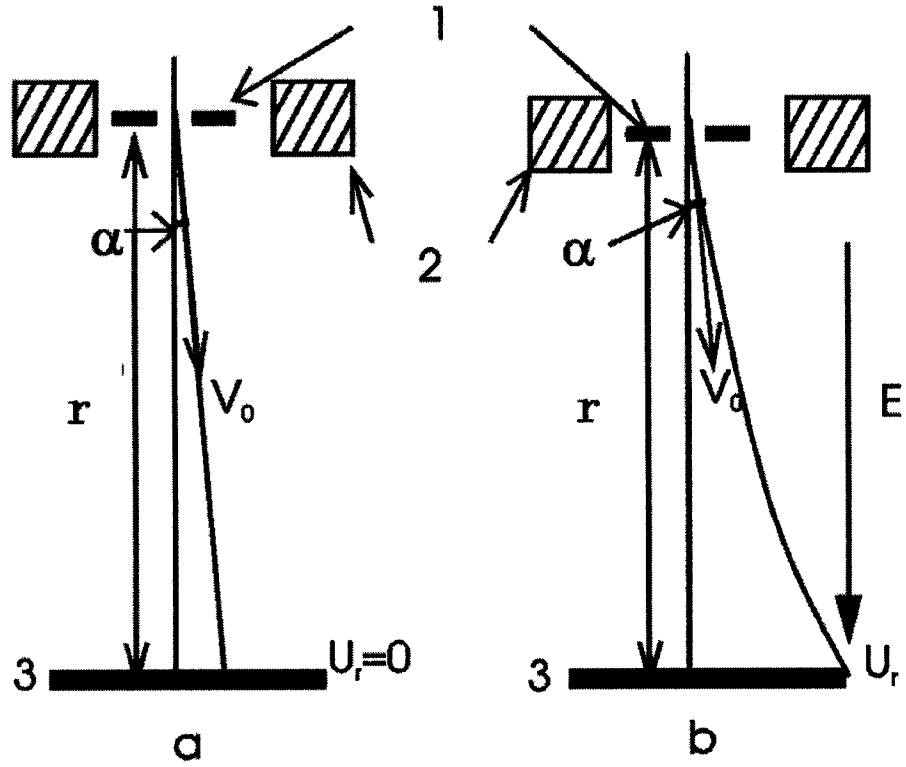


Figure 3-18: Diagram of electrons traveling from the final aperture to the stage in the SEM column without (a) and with (b) the retarding potential  $U_r$ . 1: Final aperture; 2: Deflection coil system; 3: Specimen stage.

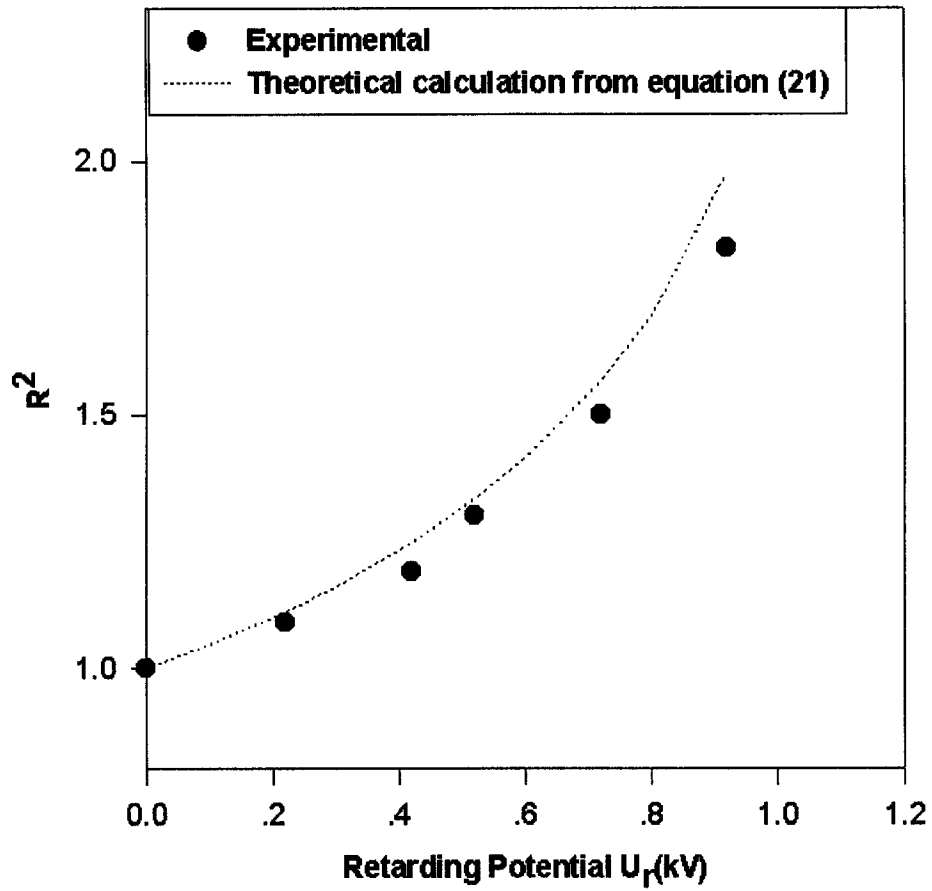


Figure 3-19: Experimental and theoretical  $R^2$ - $U_r$  curve (with an accelerating energy  $U_a=1.12\text{keV}$ ), where  $R^2$  is the ratio of area in low-voltage operation to that in normal operation.



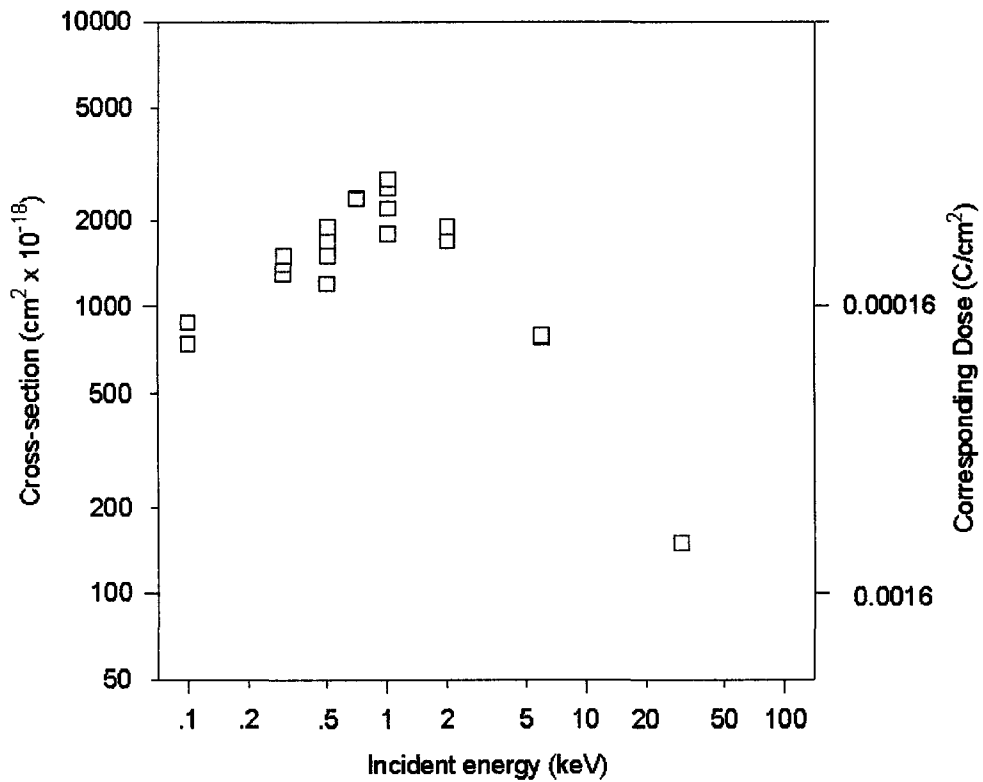


Figure 3-20: The dependence of damage cross-section on the incident energy for a coronene film measured in our SEM by monitoring CL-fading. In the energy range from 1keV-30keV, damage rate measurements were done without any retarding potential, while in the energy below 1keV, measurements were conducted with a constant accelerating energy of 1.12keV and a retarding potential on the stage.

Magnification :	X156	X312	X450	X625
Beam Current: ( $\times 10^{-8}$ A)	2.90	2.80	2.75	2.70
Width, Wd: ( $\times 10^{-2}$ cm)	7.5	3.7	2.6	1.9
Length L: ( $\times 10^{-2}$ cm)	10	5.0	3.5	2.5
Area estimated from Screen $W_d \times L$ : ( $\times 10^{-4}$ cm <sup>2</sup> )	75	19	9.1	4.8
Scanned area $W_s \times L$ : ( $\times 10^{-4}$ cm <sup>2</sup> )	26	13	9.1	4.8
Ratio of Wd/Ws:	2.9	1.5	1	1
Current Density: ( $\times 10^{-6}$ A/cm <sup>2</sup> )	3.87	1.47	3.02	5.62
Chara. Dose: $D_{1/e}$ : ( $\times 10^{-4}$ C/cm <sup>2</sup> )	2.7	3.8	7.0	7.8

Table 3-1: Measurement of characteristic doses for different magnifications. ( $E_0=6$ keV, spot size =  $0.5\mu\text{m}$ )

Materials	$\kappa$ ( $\text{Wm}^{-1}\text{K}^{-1}$ )
Celluloid (solid)	0.21
Ebonite (solid)	0.16
Rubber (solid)	0.13
Benzene (liquid)	0.14
Paraffin oil (liquid)	0.15

Table 3-2:  $\kappa$  values for some solid and liquid organic materials [Herbert 1989].

## Chapter 4 Discussion

### *Energetic electron interaction with solids*

Within a solid, the scattering of fast electrons can be divided into two categories: (1) elastic (including quasi-elastic) scattering, where an electron loses practically no energy ( $< 1\text{eV}$ ) in the collision. (2) inelastic scattering, where the energy loss is usually greater than  $1\text{eV}$ .

In the case of large scattering angles, elastic scattering is caused by the Coulomb field of the nucleus. Quasi-elastic scattering occurs in crystalline materials because the atoms are rarely at their exact lattice sites, due to thermal motion. The elastic scattering of electrons by the Coulomb potential of a nucleus is the most important of the interactions that contribute to the image contrast in the case of TEM imaging. Inelastic scattering is due to interaction of the fast electron and atomic electrons. The inelastic scattering is concentrated within smaller scattering angles and the excitation of energy states results in energy losses. The most important mechanisms are plasmon and interband excitations and inner-shell ionizations. The inelastic scattering process is less localized than elastic scattering and does not contribute much to high-resolution TEM images, but the analytical modes of energy-loss spectroscopy become of greater interest. The inner-shell ionization also results in the subsequent emission of characteristic x-ray quanta or Auger electrons, when the electrons return into the initial states.

### ***Beam effects in the electron microscope***

The electrons in an electron microscope provide useful image, diffraction and spectroscopic information, but some damage to the irradiated area of the specimen is unavoidable. Beam effects can be categorized as follows [Egerton 2003]:

Heating of the specimen is a consequence of the inelastic scattering of electrons, which implies energy transfer. As discussed in Chapter 3, by keeping the sample in a low temperature, using some metal substrate as a heat sink and optimizing the irradiation condition in the microscope, the heating effect can be negligible.

Charging effects occur in materials of low electrical conductivity. A positive charge will attract back the lower-energy secondary electrons resulting in a dark area in the secondary image, while a negative charge may deflect the primary beam, causing image distortion and possibly permanent damage to the specimen due to the high internal electric field.

Mass loss results in a cratering or thinning in the vicinity of the electron beam. Elements of low atomic number are usually lost preferentially. Mass loss usually needs a large dose.

Changes in crystal structure and molecular structure (for organic materials) are the most serious damage caused by ionization. They are the main topic in this research work and the mechanisms and

reduction of the sensitivity to damage will be discussed in detail from previous and current work.

### ***High resolution imaging and damage***

In this section, we will discuss how the radiation damage limits high resolution in electron microscopy. A formula used to calculate the minimal dose for obtaining high resolution in TEM has been reported [Reimer 1975; Glaeser 1975; Howie 1985]. To form an image at resolution  $d$  when the image contrast available is  $C$ , a certain minimum electron dose  $D$  is required. If one assumes that from an area  $d^2$  there are  $\Delta N$  more electrons than  $N$  electrons in an equal area beside the object, the contrast is  $C = \Delta N/N$ . There is a noise amplitude of  $N^{1/2}$ . The signal-to-noise ratio should exceed a factor  $k$ , usually taken from 3 to 5. The signal-to-noise ratio is

$$\Delta N / N^{1/2} = N^{1/2} C > k \quad k=3 \text{ to } 5. \quad (1)$$

The number  $N$  is related to the dose  $D = Jt$  by

$$N = fJtd^2 / q \quad (2)$$

where  $f$  = number of electrons used to produce the image, relative to the total number  $N_0$  of incident electrons on the area  $d^2$ , and  $q$  = electronic charge. Substituting (2) into (1) leads to

$$d > k / [C(fD/q)^{1/2}] = k / [C(fN_0)^{1/2}] \quad (3)$$

Reimer [1975] reported the limitation of radiation damage to the high resolution. Table 4-1 has a logarithmic scale for the dose  $D$  in  $C/cm^2$ , the corresponding scale expressed in the number of electrons per  $\text{\AA}^2$ , and presents some of the most important total damage doses of different substances. In material like chlorinated copper phthalocyanine, which is very resistant to radiation damage, where the critical dose to cause severe damage at 100keV is about  $30C/cm^2$ , a resolution of 0.05nm could theoretically be achieved for a contrast of 10% and a collection efficiency of 0.5. In practice the best resolution is around 0.2nm. In many other organic materials, where the critical dose can be lower by three or four orders of magnitude, the attainable resolution will be much worse.

In SEM, a deflection coil system in front of the last lens scans the electron probe in a raster across the specimen and in synchronism with the electron beam of a separate display instrument such as cathode-ray tube (CRT). The intensity of the CRT is modulated by one of the signals resulted from the electron beam interaction with the specimen such as Secondary Electrons (SE) and Backscattered Electrons (BSE) to form an image. The magnification can be increased simply by decreasing the scan-coil current and keeping the image size on the CRT constant. In the high-energy range, the resolution is limited by the interaction volume of electrons in the specimen, while in the low energy range, the probe size mainly limits the spatial resolution. For those beam-damage-sensitive materials such as organic and biological specimens, beam damage sometimes seriously prevents good imaging. For example, 60keV electrons will

destroy amino acids at a dose of  $10^{-3}\text{C}/\text{cm}^2$  [Reimer 1985]. Scanning with a probe current  $I_p = 10^{-11}\text{A}$  in a frame time  $T = 100\text{s}$  at a magnification  $M = 10,000$  corresponds to a dose of  $10^{-3}\text{C}/\text{cm}^2$ , with  $10 \times 10 \text{ cm}^2$  CRT display screen. This means that amino acids are already strongly damaged by one high-resolution scan.

### ***Damage mechanism***

#### *General theoretical considerations*

The actual damage processes, which follow a given inelastic scattering event, are often quite varied and complicated. Inelastic scattering processes may be broadly classified as molecular (or atomic) excitation, ionization, or collective molecular excitation (plasmon excitation). Plasmons can subsequently decay into states involving molecular ionization. Secondary electrons, which result from a primary ionization, can cause further excitations and ionizations as they track through the specimen.

If a chemical bond is unstable in an excited or ionized state of a molecule, then the bond will be split. The result of such a process is often the formation of highly reactive free radicals. Further chemical processes result in intermolecular cross-linking or in the conversion of single bonds into double bonds.

Another serious factor limiting high resolution is direct atomic displacement [Glaeser 1975; Reimer 1975]. This phenomenon is due



to the knock-on processes in which energy is directly transferred to the nucleus by large angle elastic scattering. Atomic displacement might only be expected to play a significant role in organic materials that are very resistant to damage following ionization.

#### *The influence of chemical structure*

The necessary dose for destroying organic material depends on the chemical structure and varies over four orders of magnitude. [Reimer 1975]. Table 4-2 indicates that amino acids, hydrocarbons, and polymers with carbon chains are very sensitive to irradiation. The bases of nucleic acids show a medium sensitivity. Aromatic compounds (conjugated compounds) are damaged by doses of one to two higher orders of magnitude than aliphatic compounds.

Compounds with benzene rings (like coronene and rubrene) show a pronounced high resistance. It is known from radiation chemistry that a benzene group also protects larger molecules because of its resonating electron configuration. Energy losses do not act locally in destroying a chemical bond because the energy is spread over the whole benzene ring, thus decreasing the probability of a bond rupture. Isaacson [1975] has examined the interactions of 25keV electrons with nucleic acid bases and amino acids. The fading of the 0-15 eV energy loss region was used to monitor the damage process. On the basis of the similar magnitudes of damage cross-sections, Isaacson believed that valence shell excitations lead to the damage of non-conjugated aliphatic compounds and that it needs K-shell events to damage aromatic compounds. The Cavendish group [Howie 1985, 1987; Muhid 1988; Stevens, 2000] measured the damage

cross-section of several organic materials including aliphatic and aromatic compounds as a function of the incident energy. They found an apparent energy threshold around 1keV in the damage process in aromatic compounds. They compared the damage cross-section with K-shell cross-section and concluded that irradiation damage to aromatic compounds needs K-shell ionization.

#### *The influence of electron energy*

Since the rate of damage is proportional to the number of ionization per unit volume, energy deposition in the specimen is one factor affecting the damage rate.

The use of higher accelerating energies, such as 1 MeV or more, has been under consideration for several years as a possible method for reducing radiation damage [Glaeser 1975]. The rationale in this case is based in part on the fact that higher energy electrons interact more weakly with the specimen, and thereby deposit less energy in the sample as they pass through. According to the Bethe Stopping Power Law, the amount of energy loss by the primary electron per unit of specimen thickness, decreases as the inverse of the incident energy. Several high-voltage experiments were reported [Wade 1984; Boudet and Roucau 1985; Pradere 1988; Revol 1990]. Ohno et al. [2002] compared behenic acid crystal diffraction-pattern fading in different incident energies and found a factor of 2.5 between 100keV and 1MV. Our CL measurements also shows the damage rate decreasing with the increasing incident energy in the range of energy from 10 - 30keV.

However some problems of high incident energy make it less advantageous. Elastic scattering, which largely creates the image contrast, will decrease with the increase of incident energy. The sensitivity of photographic emulsion decreases as the accelerating voltage increases. The knock-on damage (ballistic nuclear displacement) becomes prohibitively severe at high energy. To obtain and maintain a high voltage itself is not easy; other effects such as heating, charging and contamination will be significant, especially when a high-energy beam hits a thick sample.

At the other end of the scale, there have been remarkable advances. Even before the scanning electron microscope (SEM) existed as a practical instrument it was realized that operation at a low incident beam energy (usually below 5keV) would be advantageous [Joy 1996]. It was hoped to see image contrast resulting from the changes in the secondary electron coefficient  $\delta$  from different elements, and this effect which would be largest when the SE yield was at its maximum, i.e. at low beam energies (Figure 4-1). The total inelastic scattering cross-section is about three times the elastic for light elements at 100keV, but it is about one-third at around 200eV, suggesting the use of lower energies. Very-low-energy electrons are considered a powerful tool for surface studies because of their small interaction depth and, consequently, small lateral spread [Bongeler 1993]. Instrumentation capable of generating SEM images in low-energy range has been described [Frank and Mullerova 1993, 1999] and work is currently in progress to build and exploit such devices.

Joy et al. [1996] gave an description of radiation damage at low beam energies. As the energy of the incident electron is reduced it transfers increasing amounts of energy per unit depth to the sample in the range of 1-10keV. A low energy electron beam thus actually damages a sample more rapidly than a higher energy beam because the energy deposited per unit volume in the sample is greater. Damage in biological and polymeric materials occurs through the breaking of bonds within the sample, and the energy required for this is only of the order of a few eV, much lower than the energy of any normal incident electron. But they believe that damage might truly be eliminated completely if the Low-Voltage Scanning Electron Microscope (LVSEM) could be operated at a low enough energy, possibly 25eV or less, because there are no high cross-section inelastic scattering events that can result in the transfer of sufficient energy to the sample to break bonds. Observation in transmission mode of purple membrane, which is a specialized region of the plasma membrane of *Halobacterium halobium*, at 100V have shown greatly reduced dose sensitivity [Spence 1994]. Liu [2002, 2003] examined semiconductor devices using an Ultra-Low-Voltage Field-Emission Scanning Electron Microscope (ULV-FE-SEM) with a retarding system operated in the energy as low as a few hundred volts. He noticed a reduced electron-beam sensitivity in low incident energy. Also he expected that the electron-induced radiation damage of delicate materials can be significantly reduced if the landing energy, defined as the energy of the incident electrons at the entrance surface of the sample, of the primary electron beam is reduced to below 50eV.

Several groups have reported a K-shell threshold effect in aromatic materials: that there is no obvious damage at the incident energy below K-shell ionization energy. If so, it will give a promising future for the LVSEM: a low-voltage (below carbon K-shell) SEM could examine such materials without damage. And at higher incident energy there would be negligible effect from low-energy secondary electrons, leading to high spatial resolution if these materials are used as electron-beam resists.

### ***Interpretation of previous and current measurements***

In the Cavendish group's experiments, they pre-irradiated the thin specimen with low-energy electrons, then examined the diffraction pattern in high-energy TEM. This might cause some problems, leading to a false damage cross-section based on the TEM diffraction-pattern fading. Specimen thickness must be less than the low-energy electron range (penetration depth  $R$ ), otherwise there will be an un-irradiated layer left after low-energy-electron pre-irradiation. High-energy electrons in the TEM will definitely penetrate the thin specimen, which will give a misleading result in the damage-rate measurement. From our TEM images, both vacuum-evaporated and solution-evaporated specimens are non-uniform. Especially the vacuum-evaporated samples have granular structure. From Table 2-1, the local thickness of a single needle within a thin specimen (with an average thickness of 5.4nm) is over 70nm. Taking  $R(\text{nm}) = 66[E_0(\text{keV})]^{1.35}$  [Bongeler 1993], the electron range  $R$  will be smaller than 70nm with incident energies less than 1keV.

To compare with previous values, the critical dose  $D_c$  causing a complete fading of the diffraction pattern and 6eV-peak of coronene measured in our TEM is plotted in Figure 4-2 with the Cavendish group's [Howie 1987]. We can see our results are consistent with the Cavendish group's data. The slight deviation is probably due to the different determination of complete fading from different observers, depending on the visual acuity of the observer, the brightness and contrast of the viewing screen, and the specimen thickness which affects the spot/background ratio in the diffraction pattern.

Similarity between the damage cross-section and the cross-section for one K-shell ionization per molecule (dashed curve in Figure 4-3) suggests K-shell ionization (if efficient) could provide the mechanism of intermolecular damage.

The 6eV-peak damage cross-sections measured here are lower than diffraction-pattern damage cross-sections, in accord with previous work [Issacson 1975]. After intramolecular and intermolecular damage (i.e. inside the molecule, short-range disorder and long-range disorder) individual aromatic rings may stay undamaged for a larger dose, which would explain why 6eV-peak cross-section has a lowest value suggesting it is the last stage of damage.

Stevens et. al. [2000] also observed the damage threshold in coronene and Cu-phthalocyanine (CuPc) (Figure 4-4) by using similar methods to the Cavendish group. The samples were exposed for predetermined times in a low energy electron transmission (LEET)

chamber. Then the sample was moved into a transmission electron microscope to check for signs of damage. Aware that damage may be limited to a surface layer in low energy irradiation, they arranged the LEET chamber to display transmission electron diffraction (TED) patterns on a single-stage channel plates at beam energies in the range 5eV to 1.5keV, which made it possible to measure the damage directly in low beam energies in some cases. Analysis of their tested organic samples in TEM showed large continuous polycrystalline films which in most areas were quite thick (20nm), but these films also contained many small areas which were presumably very thin (50Å). They think the observed diffraction patterns at low electron energies probably originate from these thin areas. Figure 4-5 shows their direct measurement of damage cross-section in the low-energy range.

The CL measurement of the damage rate relates to an early stage of radiation damage, based on the fact that the values of CL cross-section are 100 times larger than the diffraction-pattern cross-section. (Figure 4-6). Therefore under such a small dose no obvious intermolecular disorder occurs. Reimer [1965, 1975] previously reported that cathodoluminescence decreases at very low doses because electron irradiation generates recombination centers which are effective in low concentration. The recombination centers are likely produced by the ruptured bonds. If mobile excitons meet such a defect even in a low concentration, radiationless recombination occurs immediately and reduces the lifetime of exciton considerably.

Although the nature of photoexcitations in conjugated polymers and organic molecular crystals is not completely understood, it is believed [Hegmann 2003] that excitons play an important role in light emission. When high-energy electrons pass through a solid medium, the primary excited state is likely to be a plasmon, in which many electrons are excited simultaneously, but the plasmon decays to a superexcited molecular state which can decay to excited singlet exciton states. The luminescence is from these excited singlet states to the ground state. It has been reported [Pope and Swenberg 1999] that the singlet excitons can fission into triplet excitons which do not luminesce. Moreover these excitons may create polarons which polarize the surrounding lattice, resulting in permanent intramolecular or intermolecular damage.

The intramolecular damage could include broken bonds, loss of hydrogen atoms, and changes in shape or orientation of the molecules, any of which might result in the creation of new energy levels with non-radiative transitions.

It was reported [Matsui 1993] that impurities introduce new electronic states into the organic crystal or affect exciton energy transfer. A damaged crystal can be considered as a mixed crystal in which impurities are introduced by irradiation. The irradiation-introduced "impurities" might play the same role as those from an evaporation source, which create radiationless energy levels.



The CL damage cross-section shows no obvious threshold effect; the dependence on incident energy matches the calculated energy-deposition rate, suggesting that all electrons cause damage. In addition, the CL cross-sections (for  $E_0 > 10\text{keV}$ ) approximately match the total-inelastic cross-section per coronene molecule (Figure 4-7), suggesting that valence excitation is a highly efficient mechanism for creating this type of damage. The fact that the CL cross-section (for  $E_0 > 1\text{keV}$ ) are somewhat higher than the total-inelastic cross-section may be due to plural scattering and the fact that some inelastic collisions generate several secondary electrons (or BSEs from substrate), which then damage adjacent molecules.

By investigating the influence of  $200\text{keV}$  electrons on the  $\pi\text{-}\pi^*$  peak in polystyrene using electron energy-loss spectroscopy (EELS) in a scanning transmission electron microscope, Siangchaew et. al. [1998, 2000] found a dependence of peak visibility on probe size. This effect may be attributable to the effects of fast secondary electrons (FSE). Significant numbers of FSE (energy  $> 50\text{eV}$ ) can be generated when materials are exposed to high energy electron beam. FSEs are sufficiently energetic to degrade a  $\pi$  bond. It is not clear whether low energy secondary electrons (SE) contribute to the damage and how much the SEs contribute. The total yield of and the energy distribution of secondary electrons introduced by primary electrons needs to be studied further.

### ***Hydrogen release***

The damage mechanism is not totally understood as yet, but bonding rupture is believed to be a main mechanism. The role of hydrogen in radiation damage to organic specimens has been studied, due to its importance to the structure of many organic materials. For example, hydrogen bonding determines the overall shape (secondary and tertiary structure) of proteins and other macro-molecules; it provides the main intermolecular cohesive force in certain organic crystals (e.g. sucrose); and (of relevance to hydrated specimens) is responsible for the bonding between water molecules [Egerton, unpublished]. Very characteristic breaks in bonds occur for a given class of compounds and it was found that the rupturing bond is not necessarily the weakest in the molecule [Stenn and Bahr 1970; Hall 1966]: the strong C-H bond is very sensitive to radiation, while the C-C bond is more resistant. The explanation might be: breaks occur in the C-C bond, but identical (geminate) recombination because of proximity and rigid environment also occurs; in contrast, because the size of the hydrogen atom permits it to diffuse, repair of a broken C-H bond is unlikely.

A single 100keV electron can transfer over 200eV of kinetic energy direct to the nucleus in a head-on elastic collision. This energy would not only remove a hydrogen atom from its original site, but also ensure a chemical reaction between the 'hot' atom with the surrounding molecules. However the small cross-section for energy transfer in excess of 4eV (sufficient to break a C-H or C-C bond)

suggests that this mechanism is less likely to result in structural damage.

In a solid, the valence electrons are to some extent dynamically coupled (plasmon excitation), so energy deposited by inelastic scattering elsewhere in a molecule may be transmitted to a hydrogen atom and vice versa. A free atom or molecular species might diffuse from its site in a lattice, depending on its size. So it is widely accepted that in the radiolysis of solid organic materials one may consider hydrogen atoms to be the sole diffusing species [Parkinson 1975]. As a result of inelastic collisions with electrons a C-H bond may break, freeing a hydrogen atom or radical which may be "hot" depending on the amount of energy imparted. Before the same bond reforms there is a finite probability of the hydrogen species diffusing away from the site leaving behind a residual radical.

Mass spectrometric measurements [Parkinson 1975] have in fact detected evolution of hydrogen in the early stages of radiation damage. In the Cavendish group's study, they also monitored the C-H concentration in coronene by the transmission peaks of infrared spectroscopy which are due to the aromatic methane absorption band (C-H). After an irradiation sufficient to destroy the electron diffraction pattern the magnitude of the signal from the C-H bonding mode decreased to about 90% of its original value. This means that when the crystal structure is completely destroyed, only 10% C-H bonds have disappeared. While the loss of H may initiate the damage, it is not necessary for all H atoms to be released to cause the damage.

A proportion of 'hot' H atoms diffused from their original sites could ionize the surrounding molecules.

The loss of H atoms during irradiation of organic molecular crystals has been studied by observing the change in the ratio  $n$  of inelastically to elastically scattered electrons in an energy analyzing TEM [Egerton 1976]. Due to Lenz's atomic scattering model, the cross-sections for elastic scattering and inelastic scattering depend only on the atomic number  $Z$  of the scattering atom. A large proportion of hydrogen in the hydrocarbon compound leads to a large predicted value of  $n$ . By monitoring the value of  $n$  as a function of irradiation dose, H loss release can be detected. This provides a technique to measure the effective cross-section of H atom release in organic materials, which will help to understand the role of hydrogen in radiation damage. We attempted to employ this method to study coronene, but for technical reasons (including current stability) the measurements were not successful.

### ***Reduction of damage***

A number of operational techniques are available for minimizing specimen damage during electron microscopy, some of which are of general validity while others vary in efficacy with the type of specimen [Cosslett 1978].

*Minimum exposure.* When examining any radiation-sensitive specimen it is obviously desirable to use the minimum exposure

compatible with recording the required detail. Focusing and astigmatism correction are carried out on a field of little interest and the region to be recorded is then quickly brought under electron illumination and photographed. This is done by shifting the illumination rather than the specimen. The exposure (current density $\times$ time) can not be reduced to an arbitrarily low level. As discussed previously, owing to the statistical fluctuations in the flux of electrons through the specimen, a certain minimum number is needed to ensure that the image of a specimen detail shall be visible against the random background. Also the minimum illumination should be intense enough to get a good image by the recording media.

*Low temperature operation.* As shown in Chapter 2, organic specimens are much less sensitive to radiation damage when kept at low temperature during microscopy. There is considerable variation with type of specimen, but most show an increase in critical dose by a factor of 2-4 (Table 4-3 [Fryer 1992]). The low temperature effect on reduced damage rate on organic specimens has been discussed in Chapter 2.

*Encapsulation.* Coating the specimen on both sides with an evaporated metal or carbon film was reported to reduce radiation damage to organic specimens [Fryer 1983]. By comparing the damage to a bare specimen to an encapsulated specimen (by carbon film), they found that encapsulation methods reduces radiation damage by a factor of 3-12 for different materials (Table 4-4). The evaporated overlayer reduces the out-diffusion of volatile species (e.g.

hydrogen or halogen atoms), and the postulate the retaining these elements within the specimen aids recombination and healing of broken bonds [Egerton 1987].

*Chemical combination.* It has been found that the radiation resistance of an organic molecule is greatly enhanced by halogenation. In copper phthalocyanine, for instant, the critical dose was increased by a factor of about 30 on complete chlorination [Uyeda 1972], suggesting that H-release is an important factor in the damage process.

### ***Future work***

1. A better study of the CL emission mechanism will be helpful to understand the damage mechanism. Is the CL emission determined only by molecular structure in solid specimens? Or does the crystal structure affect the emission as well? By comparing the emission spectra from crystalline and amorphous specimens, we can find the answer. Also the results from solid specimens and solution samples will give some useful information. While it is difficult to test a solution sample in a SEM, the photoluminescence experiment will be easy to conduct.

If the damage comes from individual molecules, it is worth knowing what kind of damage it is: broken bonds, loss of hydrogen atoms, and changes in shape or orientation of the molecules. Broken bonds or loss of hydrogen atoms can be monitored by some techniques as

discussed below. Changes in shape or orientation of the molecules can be examined in other microscopes (Atomic Force Microscope and scanning tunneling microscope). Whether the intermolecular structure affects the damage can be verified by using different specimens: amorphous and crystalline.

2. Since the damage causing the decay of CL emission might be different from that causing crystal-structure disorder, it is worth repeating DP measurement in the low-energy range to verify the threshold effect. But it is required that heating, thickness, contamination problems be avoided if using the two-step method:

a: As discussed an ultra-thin specimen ( $t < R$ ) is required in the damage experiments by diffraction-pattern method. An extensive study on organic thin film growth by vacuum deposition is needed. The effect of impurities in the materials has not been considered during the evaporation. Moreover impurities might affect the decay of the CL emission from the sample [Matsui 1993]. Purifying the source materials before evaporation might improve the morphology of evaporated specimens. It is surprising to get granular structure even though the substrate was cooled down to the  $LN_2$  temperature. The evaporated source flux might heat up the substrate even with a slow deposition rate, so the substrate temperature needs to be measured during the evaporation. Specimens should be transferred into TEM to check the film morphology as soon as possible after the deposition in order to avoid any "heating" at room temperature. To prevent condensation of atmospheric water vapour, a cryotransfer system is

needed to carry the specimen from the evaporation chamber to the TEM.

b: As discussed in Chapter 2, the beam heating might be severe in the low-energy range. A low dose rate will solve the problem, but a long time is needed to reach a given dose. This might not be practical for the SEM and the beam instability might be significant in long-time illumination. Thin-metal substrates can act as a heat sink, but the interaction between the diffraction patterns of the organic specimen and substrate will make it more complicated to detect damage in the TEM.

c: It will be more simple if the diffraction pattern of specimen can be directly examined in low-energy SEM. A camera below the sample in the specimen stage might detect the diffraction pattern, if connected to a display system. But this needs more technical work to make it practical.

3. To understand the role of hydrogen in the damage process, a quantitative study of H-loss in organic materials is necessary. The measurement of inelastic/elastic ratio is a good method when the technical problem is solved in our TEM. Infrared spectroscopy can be used, but many problems need to be considered, such as the sample preparation, amount of materials needed in infrared experiments and electron dose calculation if the irradiation is carried out in electron beam instruments other than the SEM.



4. Although there is no obvious reason that applying a potential on the sample stage will affect the beam current, it is worth measuring the beam current difference experimentally. An electrometer connected between the sample stage and the power supply can measure the beam current when the retarding potential is on.

5. A theoretical calculation about the yield and energy distribution of fast secondary electrons (FSE) introduced by primary electrons will be helpful to understand the decay of the damage cross-section in the low-energy range.

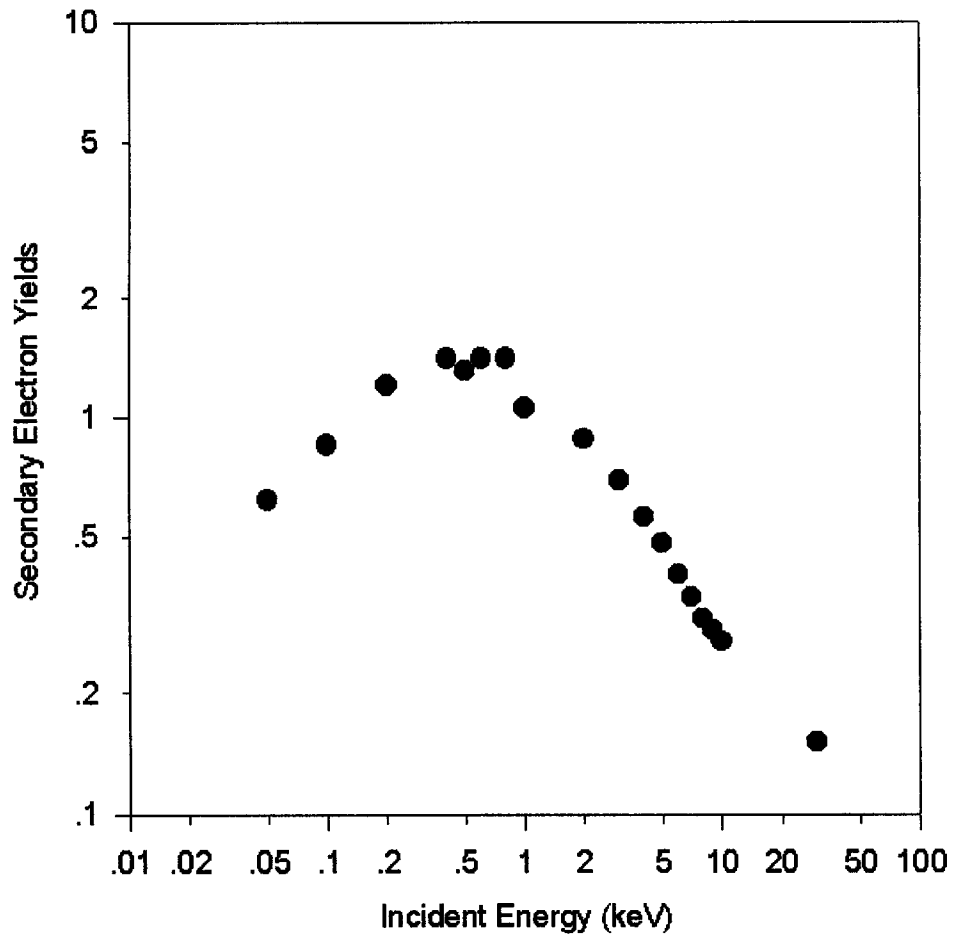


Figure 4-1: Variation with incident energy of secondary electron yield for silver [Joy 1996].

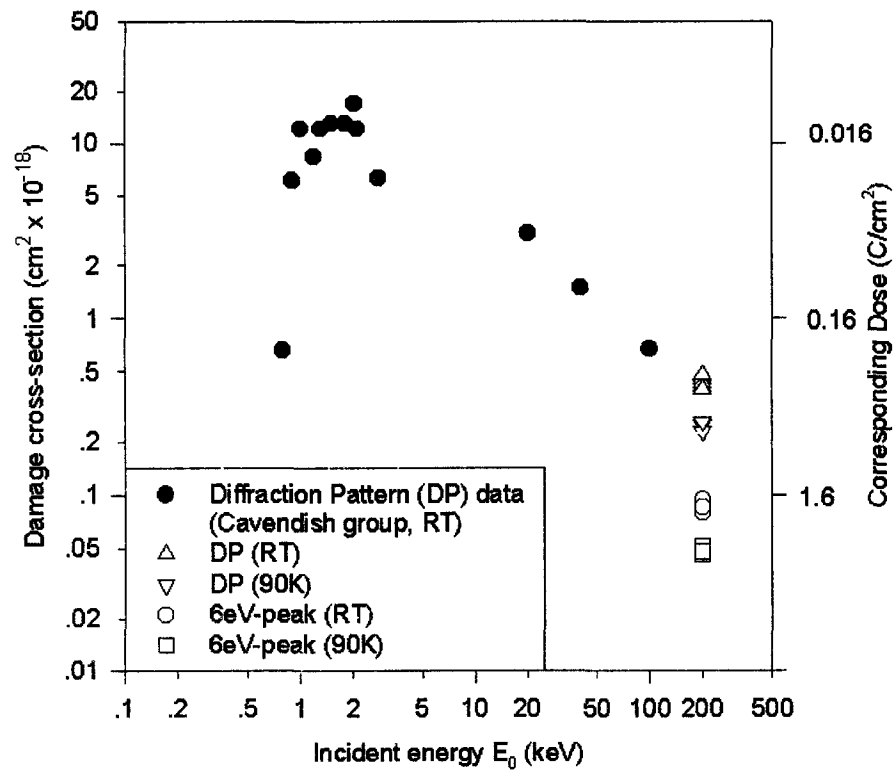


Figure 4-2: Previous damage measurement by the Cavendish group (solid) [Muhid 1988] by monitoring the fading of the diffraction pattern at room temperature and our measurements (hollow data points) at room temperature and 90K.

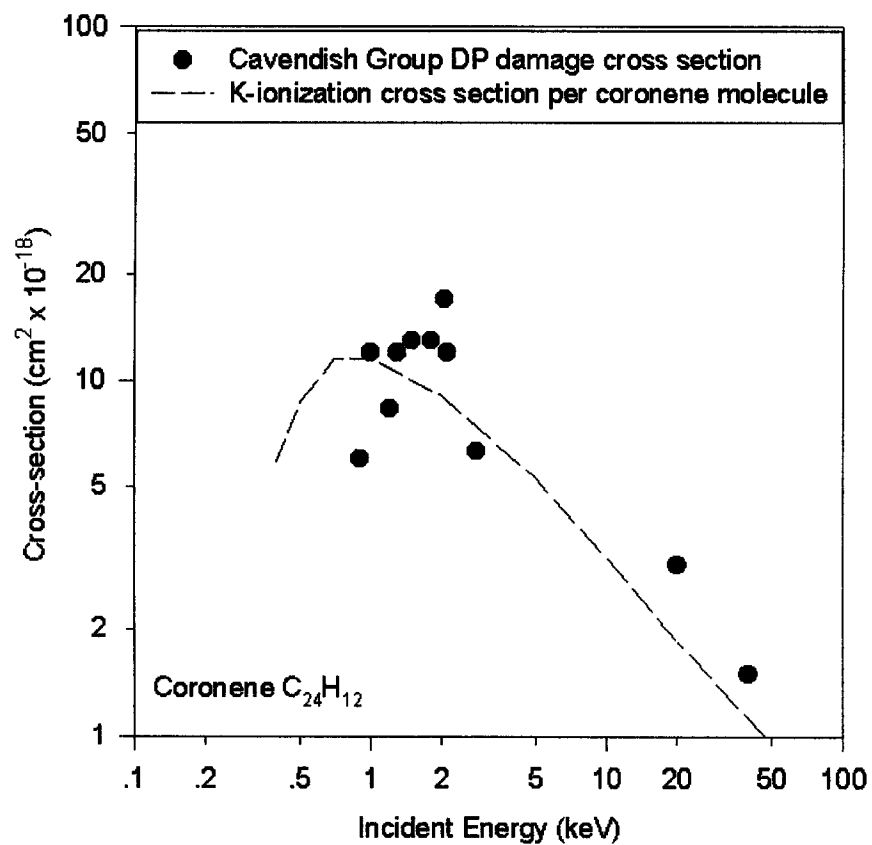


Figure 4-3: Diffraction Pattern damage cross-section and K-shell ionization cross-section [Muhid 1988].

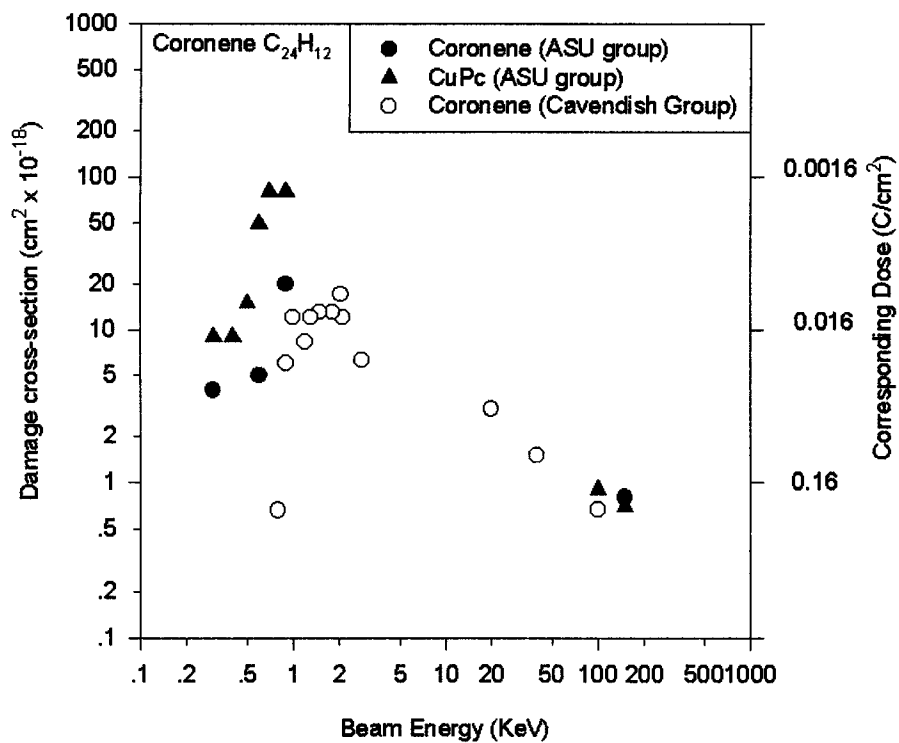


Figure 4-4: Diffraction pattern damage cross-section measured by the Cavendish group [Muhid 1988] and Arizona State University group [Stevens 2000].

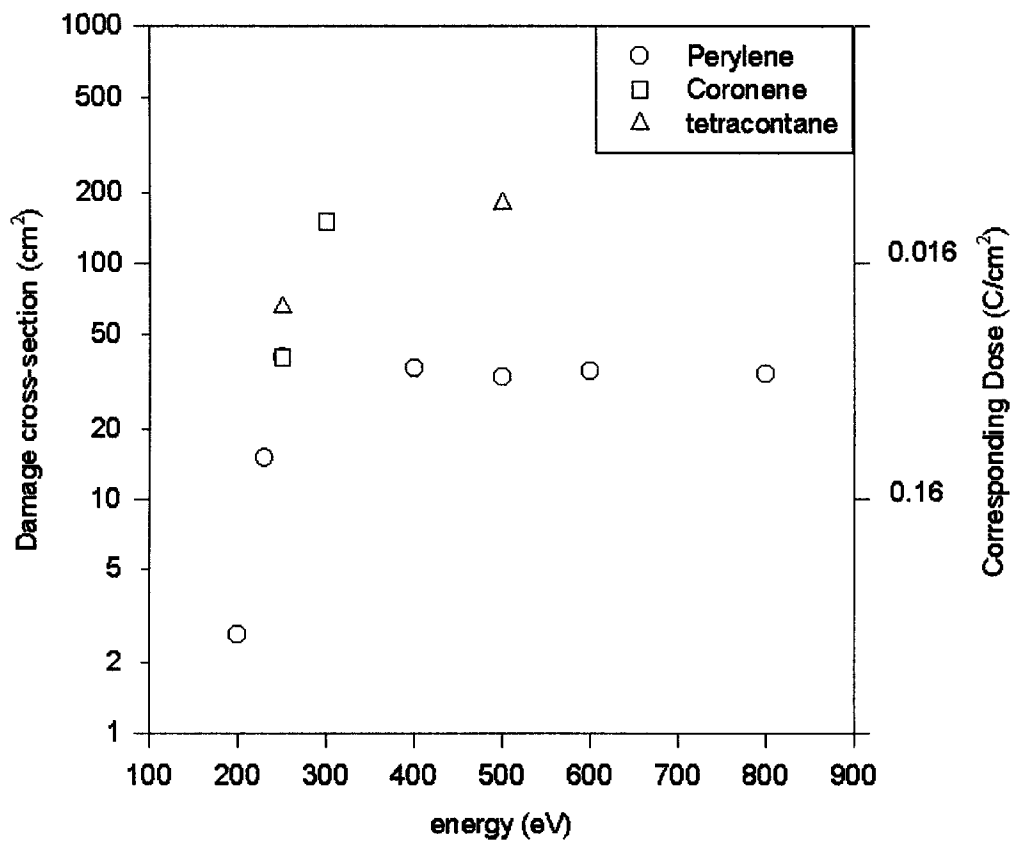


Figure 4-5: Direct measurement of diffraction pattern damage cross-section in low energy irradiation [Stevens 2000].

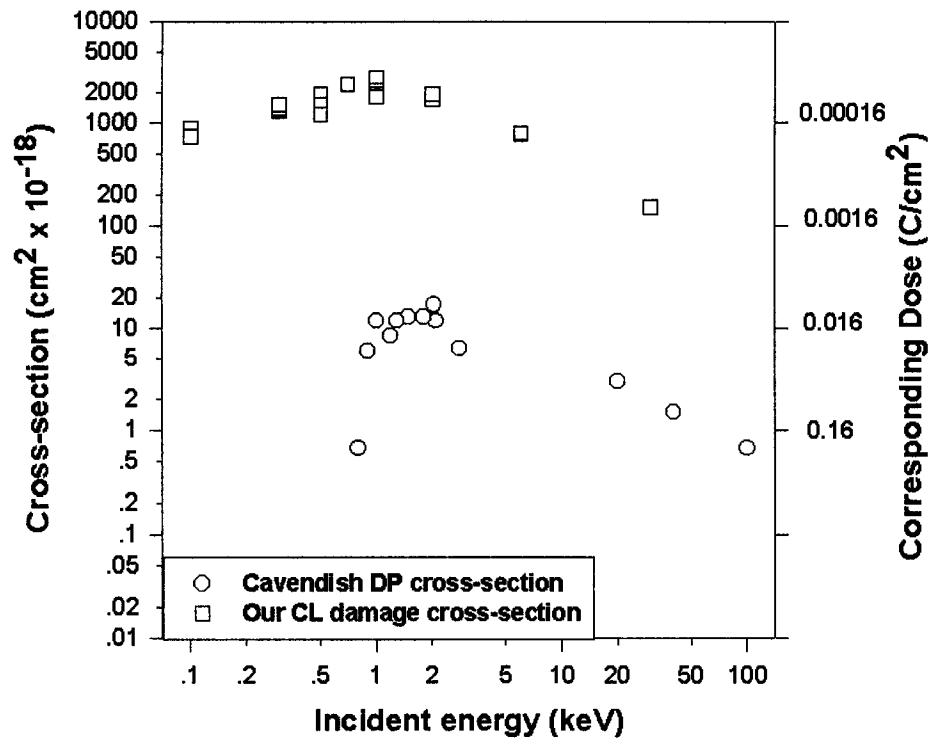


Figure 4-6: Our CL damage cross-section and previous diffraction pattern damage cross-section measured by the Cavendish group [Muhid 1988].

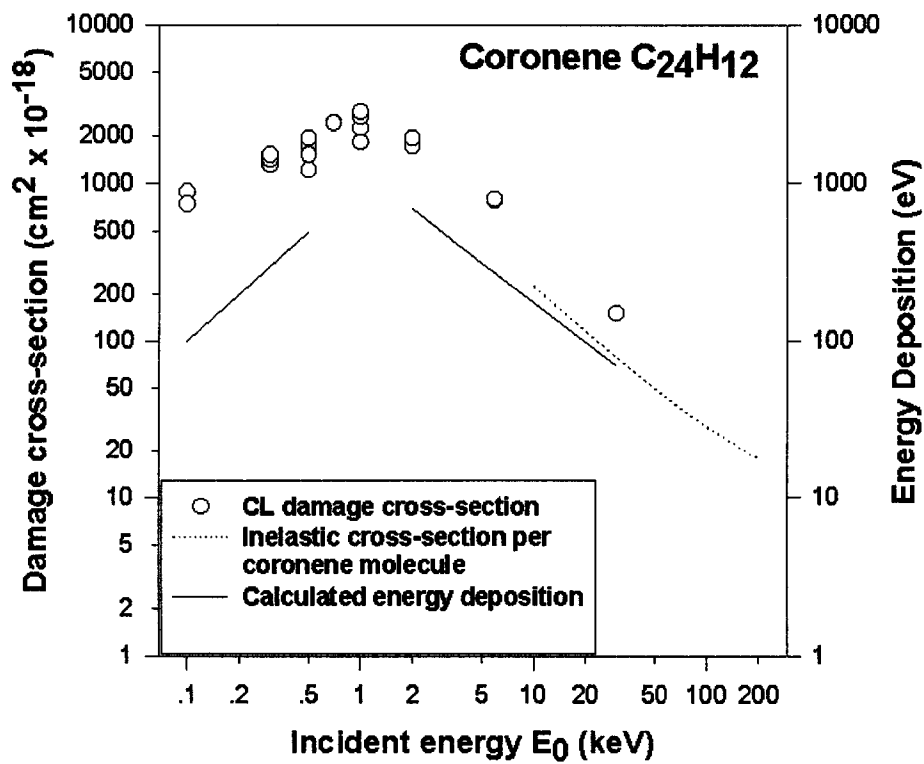


Figure 4-7. The CL damage cross-section, calculated energy deposition rate (for a 60nm coronene) and inelastic cross-section per coronene molecule.



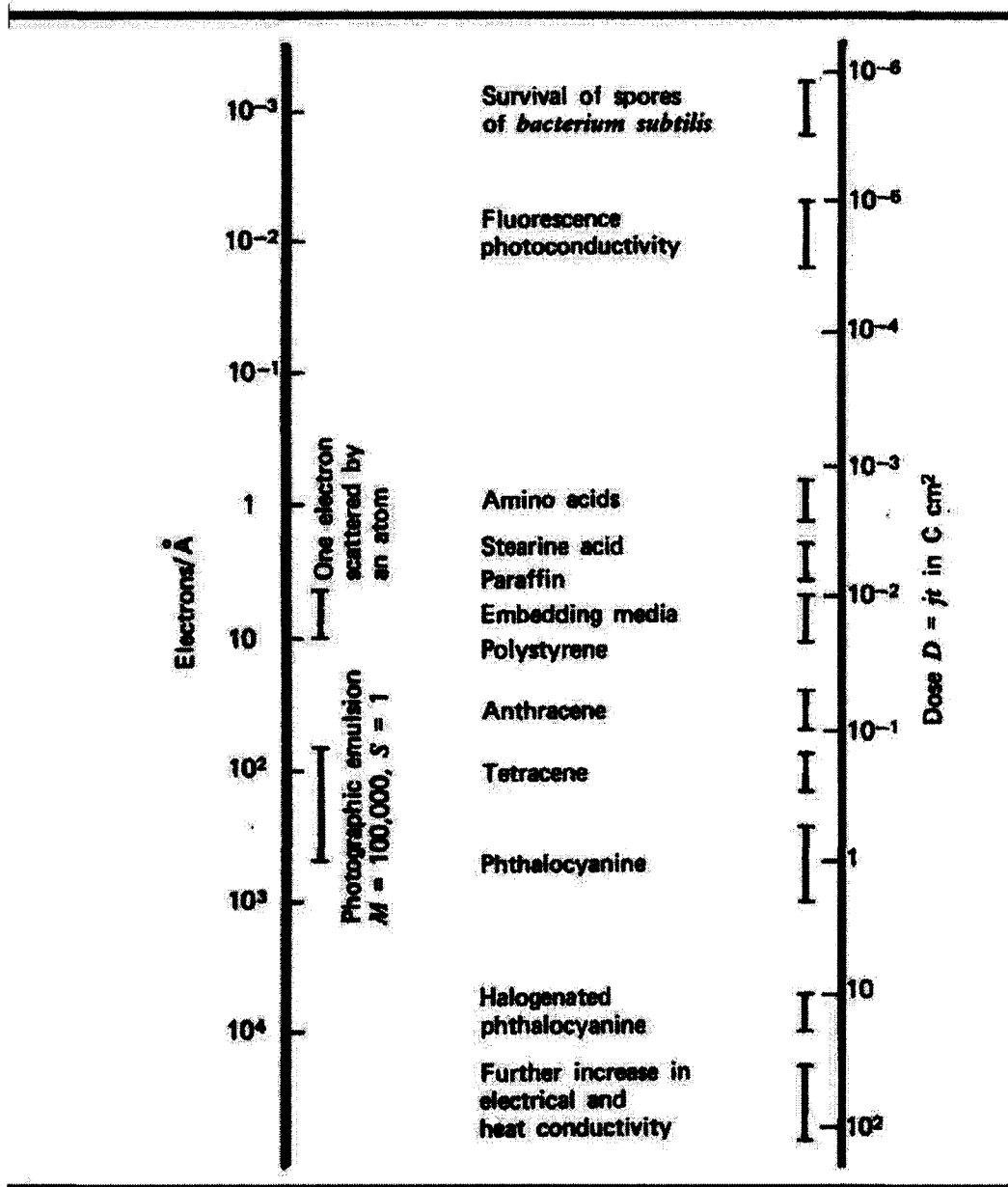


Table 4-1: Dose, D, and corresponding number of electrons /Å² for the damage of different materials and physical properties compared with the dose to get one elastically scattered electron per atom and to blacken a photographic emulsion [Reimer 1975].

Substance	D (C/cm <sup>2</sup> )	E <sub>0</sub> (keV)	Method
<b>Amino acids</b>			
Glycine	1.5×10 <sup>-3</sup>	60	ED
l-Valine	1.5×10 <sup>-3</sup>	80	ED
Leucine	1.5-2×10 <sup>-3</sup>	60	ED
<b>Aliphatic hydrocarbons</b>			
Stearic acid	2-3×10 <sup>-2</sup>	60	ED
Paraffin	3-5×10 <sup>-2</sup>	60	ED
Polymethacrylate	0.8-1×10 <sup>-3</sup>	60	ED
Polyoxymethylene	7-8×10 <sup>-3</sup>	80/100	ED
Polyethylene	0.7-1×10 <sup>-2</sup>	100	ED
Nylon 6	1.2×10 <sup>-2</sup>	100	ED
Polyvinylformal	1×10 <sup>-2</sup>	75	LM
Polyanide	1.5-2×10 <sup>-2</sup>	75	LM
Polyester	2×10 <sup>-2</sup>	75	LM
Fluorinated ethylene propylene	0.5-1×10 <sup>-2</sup>	75	LM
Tetrafluorinated ethylene polymer	1-1.5×10 <sup>-2</sup>	75	LM
Gelatin	1×10 <sup>-2</sup>	75	LM
<b>Bases of nucleic acids</b>			
Adenosine	1×10 <sup>-2</sup>	80	ED
Cytosine	3×10 <sup>-1</sup>	20	EL
Guanine	6×10 <sup>-1</sup>	20	EL
<b>Aromatic compounds and dyes</b>			
Anthracene	6-8×10 <sup>-2</sup>	60	ED
Tetracene (naphthacene)	2×10 <sup>-1</sup>	100	ED
Indigo	1.4×10 <sup>-1</sup>	60	ED
Pentacene + tetracene	3-5×10 <sup>-1</sup>	60	LA
Fushsin	2×10 <sup>-1</sup>	60	LA
Neutral red, indigo	5×10 <sup>-1</sup>	60	LA
Phthalocyanine	1×10 <sup>-1</sup>	60	ED
Cu-phthalocyanine	1-2	60	ED
CuCl16-phthalocyanine	25-35	100	ED

ED: electron diffraction; LM: loss of mass; EL: energy loss; LA: Light absorption

Table 4-2: Observed saturation dose, D, for radiation damage of different organic compounds (E<sub>0</sub>=electron energy) [Reimer 1975].

Compound	Thickness (nm)	Temperature (K)	Extinction dose (C/cm <sup>2</sup> )	Factor T10/T295
Metal-free phthalocyanine	6	295	0.0985	7.4
	6	10	0.727	
Coronene	15	295	0.112	5.5
	15	10	0.62	
Ovalene	10	295	0.075	8.9
	10	10	0.70	

A. Extinction values for crystal films at room temperature and 10K.  $E_0=100\text{keV}$ . From [Fryer 1992].

Compound	Method	Temperature (K)	Dose (C/cm <sup>2</sup> )	Factor T90/T295
Coronene	Electron Diffraction	295	0.37±0.02	1.8
		90	0.65±0.04	
Coronene	Energy Loss	295	1.9±0.2	1.7
		90	3.3±0.2	

B. Critical doses for Coronene by our measurements:  $E_0=200\text{keV}$

Table 4-3: Temperature effect on damage dose.

Sample	With carbon coating (C/cm <sup>2</sup> )	Without carbon coating (C/cm <sup>2</sup> )	Thickness (Å)	Factor and standard deviation
Paraffin C <sub>36</sub> H <sub>74</sub>	0.040 ± 0.005	0.013 ± 0.003	Unknown	3.1±0.4
Perylene	0.11 ± 0.02	0.04 ± 0.01	330	2.6±0.7
Phthalocyanine	0.47 ± 0.08	0.175 ± 0.020	100	7.0±0.5
Chlorinated copper phthalocyanine	19.5 ± 5.0	2.10 ± 0.15	54	9.3±0.8
Catalase	0.050 ± 0.001	0.015 ± 0.002	Unknown	3.1±0.4
Brominated copper phthalocyanine	10.6 ± 0.2	0.92 ± 0.17	35	11.6±2.0

Table 4- 4: Electron doses required for extinction of the diffraction pattern ( $E_0=100\text{keV}$ ) for samples with carbon coating and without carbon coating [Fryer 1983].

**References:**

- Baldock, G.R., "Excited electronic levels in conjugated molecules",  
Proceedings of Physics Society A, 63 No 6 (1950) 585-591.
- Barbara, B. and Gunther, L., "Magnets, molecules and quantum  
mechanics", Physics World, March (1999) 35-39.
- Birks, J.B., in Photophysics of Aromatic Molecules, London, New  
York, Wiley-Interscience, (1970).
- Bongeler, R., Golla, U., Kassens, M., Reimer, L., Schindler, B., Senkel,  
R., Spranck, M., "Electron-Specimen interactions in Low-  
Voltage Scanning electron microscopy", Scanning, 15 (1993) 1-  
18.
- Bowen, E. J. , in Luminescence in Chemistry, London, Princeton,  
N.J., Van Nostrand, (1968).
- Boudet, A., Roucau, C., "Degradation of polyethylene single crystals  
in electron microscopy between 1 and 2.5MV", Journal de  
Physique, 46 (1985) 1571-1579.
- Brewer, G.R., in Electron-Beam Technology in Microelectronic  
Fabrication, New York : Academic Press, (1980).
- Burrows, P.E., "Prospects and applications for organic light-emitting  
devices", Current Opinion in Solid State and Materials Science,  
2 (1997) 236-243.
- Chang, J.W., Kim, H, Kim J.K. and Ju, B.K., "Structure and  
morphology of vacuum-evaporated pentacene as a function of  
the substrate temperature", Journal of the Korean Physical  
Society, 42 (2003) S647-S651.

- Cosslett, V.E., "Radiation damage in the high resolution electron microscopy of biological materials: a review", *Journal of Microscopy*, 113 Pt2 (1978) 113-129.
- Ditchfield, R.W., Grubb, D.T. and Whelan, M.J., "Electron energy loss studies of polymers during radiation damage", *Philosophical Magazine*, 27 (1973) 1267-1280.
- Dodabalapur, A., "Organic light emitting diodes", *Solid State Communications*, Vol. 102, No. 2-3, (1997) 259-267.
- Egerton, R.F., "Measurement of Inelastic/Elastic Scattering Ratio for fast electrons and its use in the study of radiation damage", *Physica Status Solidi, Section A*, 37 (1976) 663-668.
- Egerton, R.F., "Organic mass loss at 100K and 300K", *Journal of Microscopy*, Vol.126, Pt1, April (1982) 95-100.
- Egerton, R.F., Crozier, P.A. and Rice, P. , "Electron energy-loss spectroscopy and chemical change", *Ultramicroscopy*, 23 (1987) 305-312.
- Egerton, R.F., in *Electron Energy-Loss Spectroscopy in the Electron Microscope*, New York, Plenum Press, (1996).
- Egerton, R.F., Rauf, I., "Dose-rate dependence of electron-induced mass loss from organic specimens", *Ultramicroscopy*, 80 (1999) 247-254.
- Egerton, R.F. and Takeuchi, M., "Radiation damage to fullerite (C<sub>60</sub>) in the transmission electron microscope", *Applied Physics Letters*, 75 (1999) 1884-1886.

- Egerton, R. F., "Unwanted effects of an electron beam", Proceedings of the Microscopical Society of Canada, (2003) 4-5.
- Egerton, R.F., "Role of hydrogen in radiation damage to organic specimens", Unpublished.
- Fawcett, J.K. and Trotter, J., "The crystal and molecular structure of coronene", Proceedings of Royal Society of London, Ser A (1965) 289-366.
- Frank, L. and Mullerova, I., "Strategies for low- and very-low-energy SEM", Journal of Electron Microscopy, 48 (3) (1999) 205-219.
- Friedrich, H., in Theoretical Atomic Physics, Berlin, New York, Springer, (1998).
- Friend, R., Burroughes, J. and Shimoda, T., "Polymer diodes", Physics World, June (1999) 35-40.
- Fryer, J.R. and Holland, F., "The reduction of radiation damage in the electron microscope", Ultramicroscopy, 11 (1983) 67-70.
- Fryer, J.R., Mcconnell, C.H., "Effect of temperature on radiation damage to aromatic organic molecules", Ultramicroscopy, 40 (1992) 163-169.
- Glaeser, R.M., "Radiation Damage and Biological Electron Microscopy", in Physical Aspects of Electron Microscopy and Microbeam Analysis (Eds. Siegel B.M. and Beaman D.R.), (1975) Chapter 12.
- Hall, C.E., in Introduction to Electron Microscopy, Malabar, Fla., Krieger, (1983).

- Hawkes, P.W. and Valdre, U., in *Biophysical Electron Microscopy: basic concepts and modern techniques*, London, Academic, (1990).
- Hegmann, F., "Ultrafast carrier dynamics in conjugated polymers and organic molecular crystals", *Physics in Canada*, March/April (2003) 81-92.
- Herbert, L.A., in *A physicist's Desk Reference*, New York, American Institute of Physics, 1989.
- Heringdorf, F., Reuter, M.C. and Tromp, R.M., "Growth dynamics of pentacene thin films", *Nature*, Vol412, 2 August (2001) 517-520.
- Howie, A., Rocca, F.J., "Electron beam ionization damage processes in p-terphenyl", *Philosophical Magazine*, B52 (1985) 751-757.
- Howie, A., Muhid M., Rocca, F.J. and Valdre, U., "Beam damage in organic crystals", *Institute of Physics Conference Series*, No. 90: (1987) Chapter 6.
- Isaacson, M., "Inelastic Scattering and Beam Damage of Biological Molecules", in *Physical Aspects of Electron Microscopy and Microbeam Analysis* (Eds. Siegel B.M. and Beaman D.R.), (1975) Chapter 14.
- Isaacson, M., "Interaction of 25keV electrons with the nucleic acid bases, adenine, thymine, and uracil", *the Journal of Chemical Physics*, 56 (1972) 1813-1818.
- Joy, D.C. and Joy, C.S., "Low Voltage Scanning Electron Microscopy", *Micron*, 27 (1996) 247-263.



- Junji, K., "Organic displays", *Physics World*, March (1999) 27-30.
- Kohl, H., Rose, H., Schnabl, H., "Dose-rate effect at low temperatures in FBEM and STEM due to object-heating", *Optik* 58 (1981) 11-24.
- Lackinger, M., Griessl, S., Heckl, W.M. and Hietschold, M., "Coronene on Ag(111) investigated by LEED and STM in UHV", *Journal of Physical Chemistry, B* 106 (2002) 4482-4485.
- Liu, J., "Low-voltage and ultra-low-voltage scanning electron microscopy of semiconductor surfaces and devices", *International Journal of Modern Physics B*, 16 No.28&29 (2002) 4387-4394.
- Liu, J., "The versatile FEG-SEM: from ultra-high resolution to ultra-high surface sensitivity", *Proceedings Microscopy and Microanalysis*, (2003) 144-145.
- Lloyd, E. H., and Penney, W.G., "Critique of the pair theory of mesomerism", *Transactions Faraday Society*, 35(2) (1939) 835-845.
- Lumb, M.D., in *Luminescence Spectroscopy*, London, New York, Academic Press, (1978).
- Malis, T., Cheng, S.C., and Egerton, R.F. "EELS log-ratio technique for specimen thickness measurement in the TEM", *Journal of Electron Microscope Technique*, 8 (1988) 193-200.
- Matsui, A.H. and Mizuno Ken-ichi, "Crystallization and excitonic luminescence of coronene crystals", *Journal of Physics, D: Applied Physics*, 26 (1993) B242-B244.

- Mets, M. De and Lagasse, A., "An investigation of some organic chemicals as cathodoluminescent dyes using the scanning electron microscope", *Journal of Microscopy*, 94 (1971) 151-156.
- Mets, M.De, Howlett, K.J. and Yoffe, A.D., "Cathodoluminescence spectra of organic compounds", *Journal of Microscopy*, 102 (1974) 125-142.
- Mets, M. De, "Relationship between cathodoluminescence and molecular structure of organic compounds", *Microscopia Acta*, 76 (1975) 405-414.
- Moffitt, W.E. and Coulson, C.A., "The electronic structure and bond lengths of coronene and pyrene", *The Proceedings of the Physical Society*, Vol.60, Part 4, 1 April (1948) 309-315.
- Muhid M., Howie, A., Rocca, F.J. and Valdre, V., "Electron beam damage in organic materials", *Proc. Ivth Asia-Pacific Conference and Workshop on Electron Microscopy*, Bangkok, (1988).
- Mullerova, I. And Frank, L., "Very Low Energy Microscopy in Commercial SEMs", *Scanning*, 15 (1993) 193-201.
- Nguyen, T.P., Jolinat, P., Destruel, P., Clergereaux, R., Farenc, J., "Degradation in organic light-emitting diodes", *Thin Solid Films*, 325 (1998) 175-180.
- Ohno, T., Sengoku, M., Arie, T., "Measurements of electron beam damage for organic crystals in a high voltage electron microscope with image plates", *Micron*, 33 (2002) 403-406.

- Paden, R.S. and Nixon W.C., "Retarding field scanning electron microscopy", *Journal of Physics, E: Scientific Instruments*, 1 (1968) 1073-1080.
- Park, S.H. and Lee, D.C., "A study of the electrical stability characteristics of a PVDF organic thin film fabricated by using the thermal vapor deposition method", *Journal of the Korean Physical Society*, 35 (1999) 431-437.
- Parkinson, G.M., Goringe, M.J, Jones, W., Rees, W., Thomas, J.M. and Williams, J.O., "Electron induced damage in organic molecular crystals: some observations and theoretical considerations", *Proceedings of EMAG 75 held at the University of Bristol*, 8-11 Sep. (1975) 315-318.
- Pauling, L. and Wheland, G.W., "The nature of the chemical bond. V. the quantum-mechanical calculation of the resonance energy of benzene and naphthalene and the hydrocarbon free radicals", *Journal of Chemical Physics*, 1 (1933) 362-374.
- Payne, R.S. and Beamson, G., "Parallel electron energy-loss spectroscopy and X-ray photoelectron spectroscopy of poly(ether ether ketone)", *Polymer*, 34 (1993) 1637-1644.
- Pope, M. and Swenberg, C., in *Electronic Processes in Organic Crystals and Polymers*, New York, Oxford, Oxford University Press, (1999).
- Pradere, P., Revol, J.F., Nguyen, L., Manley, R., "Lattice imaging of poly-4-methyl-pentene-1 single crystal; use and misuse of Fourier averaging techniques", *Ultramicroscopy*, 25 (1988) 69-80.

- Pullman, B. and Pullman, A., in *Quantum Biochemistry*, New York, Interscience Publishers, (1963).
- Reimer, L., "Irradiation Changes in Organic and Inorganic Objects", *Laboratory Investigation*, 14 No.6 (1965) 1082-1096.
- Reimer, L., "Review of the radiation damage problem of organic specimens in electron microscopy", in "Physical aspects of electron microscopy and microbeam analysis", Wiley, New York (1975).
- Reimer, L., "Methods of detection of radiation damage in electron microscopy", *Ultramicroscopy*, 14 (1984) 291-304.
- Reimer, L., *Scanning Electron Microscopy : physics of image formation and microanalysis*, Berlin, New York, Springer-Verlag, (1985).
- Revol, J.F., "Electron crystallography of radiation-sensitive polymer crystals". In: Fryer, J.R., Dorset, D.L. (Eds.), *Electron crystallography of organic molecules*. Kluwer Academic, Dordrecht, (1990) 169-187.
- Ritsko, J.J. and Bigelow, R.W., "Core excitons and the dielectric response of polystyrene and poly(2-vinylpyridine) from 1 to 400eV", *Journal of Chemical Physics*, 69 (1978) 4162-4170.
- Seah, M.P., and Dench, W.A., "Quantitative electron spectroscopy of surfaces: A standard data base for electron inelastic mean free paths in solids", *Surface and Interface Analysis*, 1 (1979) 2-11.

- Sheats, J.R., Antoniadis, H., Hueschen, M., Leonard, W., Miller, Moon, R., Roitman, D., Stocking, A., "Organic electroluminescent devices", *Science*, Vol. 273, 16 August (1996) 884-888.
- Shi, J. and Tang, C.W., "Doped organic electroluminescent devices with improved stability", *Applied Physics Letters*, 70 (13) (1997) 1665-1667.
- Siangchaew, K. and Libera, M., "Effects of fast secondary electrons on spatially-resolved low-loss EELS of polystyrene", *Microscopy and Microanalysis*, 4 (Suppl 2: Proceedings) (1998) 804-805.
- Siangchaew, K. and Libera, M., "The influence of fast secondary electrons on the aromatic structure of polystyrene", *Philosophical Magazine A*, 80 No.4 (2000) 1001-1016.
- Siegel, B.M. and Beaman, D.R., in *Physical Aspects of Electron Microscopy and Microbeam Analysis*, New York, Wiley, (1975).
- Sklar, A. L., "Theory of color of organic compounds", *Journal of Chemical Physics*, 5 (1937) 669-681.
- Sohmen E., Fink J., and Kratschmer W., "Electron energy-loss spectroscopy studies on C<sub>60</sub> and C<sub>70</sub> fullerite", *Zeitschrift Fuer Physik, B: Condensed Matter*, 86 (1992) 87-92.
- Spence, J., Qian, W., Zhang, X., "Contrast and radiation damage in point-projection electron imaging of purple membrane at 100V", *Ultramicroscopy*, 55 (1994) 19-23.

- Stenn, K. and Bahr, G.F., "Specimen damage caused by the beam of the transmission electron microscope, a correlative reconsideration", *Journal of Ultrastructure Research*, 31 (1970) 526-550.
- Stevens, M.R., Chen, Q., Weierstall, U. and Spence, J., "Transmission electron diffraction at 200eV and damage thresholds below the carbon K edge", *Microscopy and Microanalysis*, 6 (2000) 368-379.
- Uyeda, N., Kobayashi, T., Suito, E., Harada, Y., Watanabe, M., "Molecular image resolution in electron microscopy", *Journal of Applied Physics*, 43(12) (1972) 5181-5189.
- Wade, R.H., "The temperature dependence of radiation damage in organic and biological materials", *Ultramicroscopy*, 14 (1984) 265-270.
- Weast, R., *CRC handbook of Chemistry and Physics*, Boca Raton, FL, CRC Press, (1988).
- Wheland G. W., in *Resonance in Organic Chemistry*, New York, Wiley (1955).
- Witke, T., Schuelke, T., Berthold, J., Meyer, C.F., Schultrich, B., "Deposition of hard amorphous carbon coatings by laser and arc methods", *Surface and Coatings Technology* 116-119 (1999) 609-613
- Yang, B., Li, Y., Xie, M., "Photoelectricity capability of imager detector with coated blends of polymer and perylene or coronene", *Chinese Physics Letters*, 20 (1) (2003) 161-163.

Zhou, G.Y., Wang, C., Lei, H., Wang, D., Shao, Z.S. and Jiang, M.H.,  
"Two-photon absorption and optical power limiting based on  
new organic dyes", Chinese Physics Letters, 18 (2001) 1120-  
1122